TURBULENT KINETIC ENERGY DISSIPATION RATE AND EDDY DIFFUSIVITY STUDY IN THE TROPICAL MESOSPHERE USING JICAMARCA RADAR DATA

A Thesis

Presented to

the Graduate School of

Clemson University

In Partial Fulfillment

of the Requirement for the Degree

Master of Science

Physics and Astronomy

---

by

Liyu Guo

May 2006

Advisor: Dr. Gerald A. Lehmacher

ABSTRACT

The MST radar at Jicamarca Radar Observatory (JRO) is a powerful radar that can detect atmospheric turbulence on the Bragg scale of 3 m in the daytime mesosphere (60-85 km). Since 2002, the radar has been operated for a few days each year in the mode of collecting 1 minute Doppler spectra in 4 beam directions and 150 m resolution. The spectral widths have been used to compute the kinetic energy dissipation rate ε due to atmospheric turbulence. A small contamination due to beam broadening (effective beam width 0.7°) has been removed.

For most days, median ε values of 1-10 mW/kg, which are consistent with the non-polar summer days results from rocket data (Lübken, 1997), and median eddy diffusivity K values of 3.2-100 m^2/s are observed. They increase with height to about 75-77 km, then decrease above, consistent with some of the results of the MU radar in Japan and the VHF radar in Gadanki, India. The variability during each day is large, for ε, it can be from 1-50 mW/kg, for K, it can be from 1-100 m^2/s. Turbulent dissipation rates for individual layers and the day-to-day variability are also discussed in relationship to the observed wind shear and estimated Richardson numbers.

The correlation between four beams of σ_{turb}^2 and the wind shear is mostly positive, but the correlation coefficients are quite small.

The correlation between SNR (signal to noise ratio) and ε is mostly positive. The correlation coefficients for each day change with height in a similar pattern as SNR; the larger the SNR at a certain altitude, the larger the correlation coefficient. The maxima of the correlation coefficients in a turbulent layer are 0.7-0.75. Days with weak SNR can have similar large correlation coefficients as days with strong SNR. This may indicate that the strength of radar echoes is determined not only by turbulence.

TABLE OF CONTENTS

Page

Table of Contents (Continued)

Page

LIST OF TABLES

Table Page

LIST OF FIGURES

Figure Page

List of Figures (Continued)

Figure Page

List of Figures (Continued)

Figure Page

List of Figures (Continued)

Figure Page

List of Figures (Continued)

Figure Page

CHAPTER 1

BACKGROUND AND INTRODUCTION

Various techniques have been used to study mesosphere dynamics including rocket (Lübken et al., 1987) and radar (Woodman and Guillen, 1974) observations. Among them radar observation has the advantage of the capability of more continuous measurements.

Knowledge of the turbulent kinetic energy dissipation rate ε in mesosphere is important in understanding the turbulent activities in that region.

The theory of deriving ε and the vertical eddy diffusivity K from Mesosphere-Stratosphere-Troposphere (MST) radar measurements has been developed (Sato and Woodman, 1982; Hocking, 1983, 1985, 1986, 1997) and there have only been two seasonal studies (Fukao et al., 1994; Rao et al., 2001) at middle and low latitudes in the Northern hemisphere using the spectral width method (to be discussed later in 1.3.3). Daily variation and layer-to-layer variation studies of the turbulent parameters have yet to be done. In this thesis, using the most sensitive MST radar data, we have studied the daily and layer-to-layer variation of the turbulent parameters in the equatorial mesosphere.

Fukao et al. (1994) used three years of observations (resolution 600 m) from the VHF MU (Middle and Upper atmosphere) radar in Shigaraki, Japan (35˚N, 136˚E) and CIRA-1986 monthly temperatures. They show that the monthly median of K increases with height in the mesosphere suggesting the predominant vertical wavelength of gravity waves increases with height. The magnitude of K is around 1-10 m^2/s in the mesosphere. The maxima of K and of the mean vertical shears were observed in summer.

Similar studies were conducted in the tropics, Gadanki, India (13.5˚N, 79.2˚E), using four years of mesospheric VHF radar data (resolution 1200 m) and lidar temperatures. The monthly median of K increases with height up to 75km and then decreases (Rao et al., 2001). The magnitude of K is about 2-5 m^2/s, somewhat smaller than the magnitude of K observed by the MU radar. The maximum values were observed during June-July and minima during November-December in the mesosphere. They also observed enhanced gravity wave activity in summer and little activity in winter. The seasonal variability of K is thought to be due to the breaking of gravity waves.

The Jicamarca radar (11.95˚S, 76.87˚W) in Peru is the most sensitive VHF radar in the world. Compared to the MU radar and the Indian MST radar, Jicamarca is more powerful and has higher vertical resolution (150 m). Seasonal studies of ε and K in the mesosphere have not been conducted there. Moreover, the knowledge of K at various geographical locations and seasons can benefit our understanding of the global circulation. Daily high resolution data can improve our knowledge of the generation of these echoes and the mesospheric dynamics they represent. The measurement of the distribution of these turbulent parameters can also provide a test for gravity wave parameterization in middle atmosphere global circulation models (e.g., Garcia and Solomon, 1985).

Table 1.1 Summary of the Jicamarca observation data used

YEAR	MONTH	DATE	CORRESPONDING DAY NUMBER
2002	JULY	18-20	199-201
2003	MARCH	5	64
	MAY	22-23, 27-29	142-143, 147-149

In this paper, data collected in 2002 and 2003 (Table 1.1) with the Jicamarca radar are used to study daily variations of ε and K. Variations in different layers have also been studied.

Section 1.1 describes the MST radar techniques. Section 1.2 gives a brief history of the improvement of the resolution of MST radars. The estimation of turbulent parameters is introduced in section 1.3. The methodology, radar setup and radar data analysis are presented in chapter 2. Chapter 3 discusses the results. Chapter 4 gives the conclusions of this study. Additional results are included in the appendix.

1.1 MST coherent radar techniques

The first VHF radar for the mesosphere can be dated back to the 41 MHz radar in Illinois (Bowles, 1958) and echoes were observed between 75-90 km altitudes. Later, echoes interpreted as turbulence were detected at 75 km at Jicamarca, Peru (Flock and Balsley, 1967). Woodman and Guillen (1974) developed the MST (Mesosphere, Stratosphere and Troposphere) technique and observed echoes from the mesosphere, stratosphere and troposphere. From then on, VHF radars started to be used for lower and middle atmosphere, hence the name MST radar.

MST radars make use of scattering and reflection from variations of humidity, temperature and electron density (Röttger, 1984). They can observe the three dimensional wind vectors, atmospheric reflectivity and stability, and morphology of turbulence and waves. Usually MST radars operate at frequencies around 50 MHz; their peak powers are between 1 kW and 1 MW. Range resolutions down to about 100 m and time resolutions down to some ten seconds are possible. Antennas range from 1000 m^2 to some 10000 m^2.

The Jicamarca radar operates at 50 MHz ($\lambda = 2\lambda_0 = 6$ m), and the transmitter system consists of four 1.5 MW peak power transmitters. The average power is 100 kW and the antenna area of Jicamarca is 84000 m^2 ($48\ \lambda_0 \times 48\ \lambda_0$) consisting of 18432 half-wave (λ_0=3 m) dipoles divided up into 64 modules which can be phased individually (Rastogi and Woodman, 1974). The modules are grouped into four squares with four independent feeds.

An MST radar system usually consists of the following components (Röttger, 1984): the oscillator generates a signal with a frequency equal to the center radar operation frequency. The controller then imposes a modulation to this signal. The transmitter amplifies the signal and transmits the signal to the sky. After the signal is being reflected and scattered back from the sky, the antenna collects the signal and sends it to the receiver. The received signal consists of the radar echo and noise. After linear amplification in the receiver, the received signal is coherently detected. After certain filtering we obtain a complex signal $c(t)=x(t)+iy(t)$, where $x(t)$ is called the in-phase component and $y(t)$ is called the quadrature component. The Fourier transform of $c(t)$ yields the power spectrum $P(\omega)$ which is the convolution of the spectrum of the refractivity fluctuations in the radar volume with the spectrum of the transmitted wave form multiplied by the bandpass characteristics of the receiver.

The radar transmitter transmits a series of pulses. When a pulse hits a target (scatterer) at range r_a (Fig 1.1), the radar receives the return echo after the time $t'_1=2t_1=2r_a/c$ (c is the speed of light).

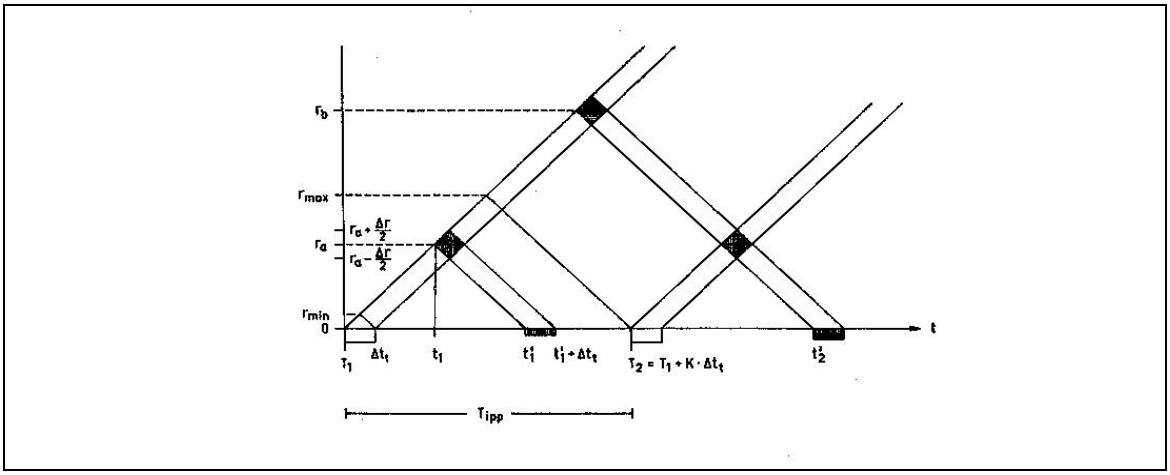

Figure 1.1 Range-time diagram for MST radar [Röttger, 1984]

Since each pulse has a duration (baud length) of Δt_t. the trailing edge will reach r_a at time $t_1 + \Delta t_t$ and the receiver at time $t_1' + \Delta t_t$. If we assume the target is a hard target, the received pulse will have the same shape as the transmitted pulse. The range gate from which the radar echoes are received is $\Delta r = c/2 \cdot \Delta t_t$. From Figure 1.1, it is easy to see that echoes from $r_a - \Delta r/2$ and r_a reach the receiver at the time t'_1, while the echoes from r_a and $r_a + \Delta r/2$ reach the receiver at the same time $t_1' + \Delta t_t$. Most of the echo power is received from the range r_a, and minimum power is received from $r_a \pm \Delta r/2$. So ideally, the range weighting function of one range gate is a triangle with the center at r_a. However, the receiver pulse response time (matched with Δt_t) distorts the received pulse into a smooth shape and delays it by about the receiver response time.

The radar transmits series of short pulses with pauses between the series. Usually a pause is set to be a multiple of Δt_t and is called the interpulse period T_{IPP}. $f_{PRF} = 1/T_{IPP}$ is the pulse repetition frequency. Range aliasing happens when the antenna receives pulses from different altitudes. For example, from Figure 1.1, range aliasing occurs when antenna receives the echoes from range r_b and r_a at the same time, t_2'. For Jicamarca, T_{IPP} is 1.33 ms and Δt_t is 1 μs so that the smallest range gate is 150 m. 64 baud alternate coded pulses are used to suppress range aliasing and to achieve the best possible resolution.

Assume the scatterer at range r is moving and the radial component of the velocity is $dr/dt = v$. Because of the Doppler effect, the phase change of the returned signal $d\Phi/dt$ (angular Doppler frequency) is $\omega_D = 2\pi f_D = d\Phi/dt = 4\pi v/\lambda$, where λ is the radar wavelength. Because of the existence of f_{PRF}, the maximum Doppler frequency to be resolved by pulse-to-pulse analysis is $f_{Dmax} = f_{PRF}/2$. The corresponding $v_{max} = \lambda \bullet f_{Dmax}/2 = \lambda f_{PRF}/4 = \lambda/4T_{IPP}$. For Jicamarca radar, λ is 6 m and T_{IPP} is 1.33 ms, v_{max} is ~ 1000 m/s. This indicates heavy oversampling is undertaken. Since the expected Doppler velocities are only a few meters per second, by coherently integration over $2N$

interpulse periods (for our data, $N=30$, see section 2.3.1), we can significantly improve the signal to noise ratio of the very weak mesospheric echoes.

The total received echo power P is the sum of the mean received power due to scattering P_s and the power due to reflection P_r: so P can be expressed as $P_s+P_r=P_tA\,\Delta rC^2/r^2$, where P_t is the transmitted power, A is the effective antenna area, Δr the range gate, r the range and C^2 is the effective reflectivity (Röttger, 1984). C^2 is dependent on the properties of the media, radar parameters, calibration constant and mean generalized refractive index gradient.

Inhomogenities in the refractive index of the atmosphere result in the backscatter of radar power. If the inhomogenities distribute in the radar volume instead of a steep change, the process is often called Bragg scattering. Bragg scattering is responsible for most of the clear air echoes. The fundamental physical principles for Bragg backscatter are the same as those causing refraction of X rays from crystals. When there is turbulence, there are inhomogenities in the air which lead to coherent scattering of waves. Only at one half wavelength of the radar, scattered waves interfere constructively and produce the strongest signal. That is why we consider the echoes of Jicamarca radar caused by Bragg scattering of electron density irregularities at scales of 3 m.

1.2 Resolution improvements of Jicamarca radar

The resolution of MST radar observations has been improved and has helped us to learn more about the structure of the echo layers. The first observation of mesospheric radar returns at Jicamarca Radar Observatory (JRO) was reported by Flock and Balsley (1967). First MST radar studies at Jicamarca (Woodman and Guillen, 1974; Rastogi and Woodman, 1974) had 5 km height resolution and could handle only a few range gates at a time. Fukao et al. (1979) made continuous measurements between 62.5 and 90 km with a 2 km resolution. The height resolution of Jicamarca radar observations was further improved to 1.5 km for early radar interferometry experiments

(Royrvik, 1983; Kudeki, 1988; Stitt and Kudeki, 1991) and to 500 m and 400 m for wind and momentum flux measurements during 1987 and 1993/94 (Fritts et al., 1992; 1997) respectively. From 1998-2000, data were taken with 300 m resolution (Riggin et al, 2002; Lehmacher and Kudeki, 2003).

We use nominal 150 m resolution data made possible by applying 64 baud coded pulses. In this study, we analyze between 60-85 km, since there is not enough electron density in the below 60 km region and too strong interference from equatorial electrojet plasma instabilities in the lower E-region (90-110 km).

1.3 Turbulent parameters and turbulent theories

Turbulent kinetic energy (TKE) is an important variable measuring turbulence intensity. The increasing or decreasing of TKE with time and height is also important in understanding turbulence activities. There are several processes responsible for the creation and destruction of TKE defined by an energy budget equation:

$$\frac{\partial \bar{e}}{\partial t} = -\bar{u}\frac{\partial \bar{e}}{\partial x} + \frac{g}{\bar{\theta}} < \theta' w' > - \frac{\partial \bar{u}}{\partial z} < u' w' > - \frac{\partial < w' e >}{\partial z} - \frac{1}{\bar{\rho}}\frac{\partial < w' p' >}{\partial z} - \varepsilon \qquad (1.1)$$

where $\bar{e}$ is TKE. The term on the left hand side is the TKE tendency term. The first term on the right hand side is the advection term. The second term is the buoyancy term, the effect of potential temperature vertical flux $< \theta' w' >$ on the tendency of TKE: TKE of a static stable layer decreases. The third term is the wind shear term where w' is eddy vertical motion: the interaction of the turbulent momentum flux with the mean vertical wind shear generates turbulence. The fourth term is just a vertical transport term. It doesn't create or destroy TKE. The fifth term is a term of TKE

redistribution because of pressure perturbation, for example gravity waves. The last term is the dissipation rate term, ε, determining how much TKE has been dissipated viscously into heat.

Another value, eddy diffusivity or eddy diffusion coefficient K is also a measure of turbulence intensity. It is the exchange coefficient for the diffusion of a conservative property by eddies in a turbulent flow. The eddy diffusion coefficient for momentum K_m (related to the third term on the r.h.s. of equation 1.1) is defined by

$$K_m = \frac{-<u'w'>}{\partial\overline{u}/\partial z}, \tag{1.2}$$

and the eddy diffusion coefficient for temperature K_T (related to the second term on the r.h.s. of equation 1.1) is defined by:

$$K_T = \frac{-<\theta'w'>}{\partial\overline{\theta}/\partial z}, \tag{1.3}$$

vertical heat flux divided by the vertical gradient of the mean potential temperature.

If we consider thermal equilibrium with energy generation due to the Reynolds stress and turbulent dissipation (Fukao et al, 1994), i.e., we only consider the buoyancy term (second term) and the wind shear term (third term) in equation 1.1:

$$\varepsilon = -\frac{\partial\overline{u}}{\partial z}<u'w'> + \frac{g}{\overline{\theta}}<\theta'w'> = (1-\frac{1}{R_f})\frac{g}{\overline{\theta}}<\theta'w'>, \tag{1.4}$$

where R_f is the flux Richardson number, defined as:

$$R_f \equiv \frac{\frac{g}{\overline{\theta}} < \theta' w' >}{\frac{\partial \overline{u}}{\partial z} < u' w' >} = \frac{Ri}{\mathrm{Pr}^{tur}} = Ri \frac{K_T}{K_m} \tag{1.5}$$

$$Ri \equiv \frac{F_{bouyancy}}{F_{inertial}} = \frac{\omega_B^2}{(\frac{du_h}{dz})^2} \tag{1.6}$$

is the flux Richardson number, the ratio of buoyancy force and inertial force. *Ri* is the gradient Richardson number. Pr^{tur} is the turbulent Prandtl number defined as the ratio of K_m (eq. 1.2) and K_T (eq. 1.3). Usually we take $K_m = K_T$, so that $Pr^{tur} = 1$ and $R_f = Ri$. From now on *K* will be used as eddy diffusion coefficient. ω_B is the Brunt-Vaisala frequency of the atmosphere:

$$\omega_B{}^2 \equiv \frac{g}{\overline{\theta}} \frac{\partial \overline{\theta}}{\partial z} = \frac{g}{\overline{T}} (\frac{\partial \overline{T}}{\partial z} + \frac{g}{C_p}) \tag{1.7}$$

The higher the Brunt-Vaisala frequency, the more statically stable the air flow. For unstable flow, where $\omega_B{}^2 < 0$, this equation cannot be used.

Insert equations 1.7, 1.4, 1.5 and 1.6 into 1.3 to obtain

$$K = \frac{\beta \varepsilon}{\omega_B^2}, \tag{1.8}$$

where

$$\beta = \frac{R_f}{1 - R_f}. \tag{1.9}$$

Based on some experimental results of turbulence (Woods, 1969) in the troposphere and in the ocean, we believe turbulence is created if *Ri=0.25*, so $R_f = 0.25$ and $\beta \approx 0.3$ in equation 1.8:

$$K = 0.3 \frac{\varepsilon}{\omega_B^2} \tag{1.10}$$

If we assume the average Brunt-Vaisala frequency is about 0.02/s, wind shear of 40m/s/km is large enough to generate a Richardson number that is less than 0.25.

Since turbulence is the mechanism causing the Bragg scale electron density irregularities responsible for the radar echoes, radar data can be used to extract information about some important turbulence intensity related values, for example, turbulent kinetic energy dissipation rate ε and in turn eddy diffusivity K (eq. 1.10).

There are mainly two ways to use radars to obtain the turbulent energy dissipation rates (Hocking, 1985) assuming that the specular reflection effect is small and all the scatter is due to turbulence. 1) Convert the absolute strength of backscattered power to ε. 2) The spectral width of the signal is used to estimate ε.

Both methods have their own advantages and disadvantages. The first method requires calibration of the radar and depends on mean gradient of fluctuation and electron density; the second method requires the calculation of beam broadening and shear broadening effect.

We have no calibration and absolute power from JRO yet, so we use the second method to estimate ε in this paper. In section 1.3.3 there will be a brief discussion of this method.

Much of the discussion of the method is based on Kolmogoroff theory of inertial range isotropic turbulence (Batchelor, 1953), so it is necessary to include a short discussion of Kolmogoroff theory and subranges for turbulence spectra (section 1.3.2) after an introduction of the statistics of turbulence.

1.3.1 Statistics of turbulence: structure function

The statistics of turbulence can be described by a conservative and passive tracer ξ and its structure function D_ξ (Lübken, 1993 (b)):

$$D_\xi(\vec{r}_1,\vec{r}_2,t) = < (\xi(\vec{r}_1,t) - \xi(\vec{r}_2,t))^2 > \tag{1.11}$$

Passive tracers are variables do not depend on the position in the turbulent patch, for example, potential temperature, in our case the refractive index fluctuation can be considered as passive tracer. If we assume the structure function is stationary (not dependent on t), locally homogeneous (only dependent on the difference of the location) and isotropic (not depend on the direction), we have:

$$D_\xi(\vec{r}_1,\vec{r}_2,t) = D_\xi(|\vec{r}_1 - \vec{r}_2|) = D_\xi(r) \tag{1.12}$$

Here we only concentrate on the special case (Lübken, 1993 (2)) where

$$D_\xi(r) = C^2 r^\mu \tag{1.13}$$

and $0<\mu<2$. C is a constant. In this case the 3D power spectrum $\Phi_\xi(k)$ is the Fourier transform of the

structure function:

$$\Phi_{\xi}(k) = \frac{\Gamma(\mu+2)}{4\pi^2}\sin(\frac{\pi\mu}{2})C^2 k^{-(\mu+3)} \tag{1.14}$$

The integral of $\Phi_{\xi}(\vec{k})$ over a spherical shell with radius k is the total energy density $E_{\xi}(k)$, which is the density of the kinetic energy per unit mass:

$$E_{\xi}(k) = \int_{4\pi} \Phi_{\xi}(k) d\Omega(k) = 4\pi k^2 \Phi_{\xi}(k) \tag{1.15}$$

1.3.2 Subranges for turbulence spectrum and Kolmogoroff theory

Before calculate $D_{\xi}(r)$ and then in turn $E_{\xi}(k)$ to determine ε. We need to first familiar with the subranges for turbulence spectrum and Kolmogoroff theory.

At very small scales, much of the turbulent energy is dissipated due to viscous effects. This range is called viscous subrange.

At very large scale, buoyancy effect is important and turbulence has a larger horizontal dimension than vertical dimension. This range is called buoyancy subrange.

The range between viscous subrange and buoyancy subrange is inertial subrange. In the inertial subrange, energy is not inserted from external sources nor is it dissipated to heat. Energy transferred from large to small scales with rate ε.

Kolmogoroff assumed that in the inertial subrange, the Reynolds number is very large (>1000) and $D_{\xi}(r)$ only depend on ε and r. Using equation 1.13 to do the dimensional analysis with ε and r, we obtain the 2/3rd law of Kolmogoroff and Obouknov:

$$D_{\xi}(r) = C(\varepsilon r)^{2/3} \tag{1.16}$$

So $\mu=2/3$. According to the Fourier transform relationship between the structure function and spectrum (eq. 1.14), then use equation 1.15, we thus find

$$E_{\xi}(k) = A\varepsilon^{2/3}k^{-5/3} \tag{1.17}$$

where $A = \frac{\Gamma(\frac{5}{3})\sin\frac{\pi}{3}}{2\pi} C$, and C is a dimensionless constant (Tatarski, 1961).

From the Taylor expansion of the structure function in the viscous subrange and assuming that it only depends on ε and v (viscosity), we perform dimensional analysis of the structure function and obtain:

$$E_{\xi}(k) \propto k^{-7} \tag{1.18}$$

Similarly by assuming that the energy spectrum only depend on ω_B in the buoyancy subrange we obtain

$$E(k) \propto \omega_B^2 k^{-3} \tag{1.19}$$

Equating equation 1.17 and 1.18, we derive the wave number k_0 that is the transition wave number between viscous subrange and inertial subrange. The inner scale l_0 which is the transition between viscous subrange and inertial subrange is $2\pi/k_0$:

$$l_0 = f\eta \tag{1.20}$$

where f is a dimensionless constant and η is the Kolmogoroff microscale:

$$\eta = \frac{\nu^3}{\varepsilon} \tag{1.21}$$

Similarly equating equation 1.18 and 1.19, we can derive the outer scale L_B that defines the transition between inertial subrange and buoyancy subrange (Hocking, 1985):

$$L_B \approx \frac{2\pi}{0.62}\varepsilon^{1/2}\omega_B^{-3/2} \tag{1.22}$$

Figure 1.2 shows an example of the subranges calculated by some typical ε and ω_B values (Hocking, 1985). ω_B values were based on the Brunt –Vaisala period profile shown on the left side of the graph. ε was assumed 100 mW/kg at 90 km decreasing exponentially to 10 mW/kg at 80 km. Between 80 and 60 km, ε was taken as 10 mW/kg.

The red box in fig 1.2 indicates Jicamarca vertical observable scales (3-150 m) and the altitude range of the data. The Bragg wavelength of 3 m for Jicamarca above 70 km should be in the viscous subrange of the turbulence spectrum. This is also based on reasonably small values of ε confirmed by rocket measurements in the mesosphere. Royrvik and Smith's (1984) ε is about 50 mW/kg at around 82 km. Lübken had mostly under 10-20 mW/kg except in polar summer (Lübken et al., 1993 (a); Lübken, 1997).

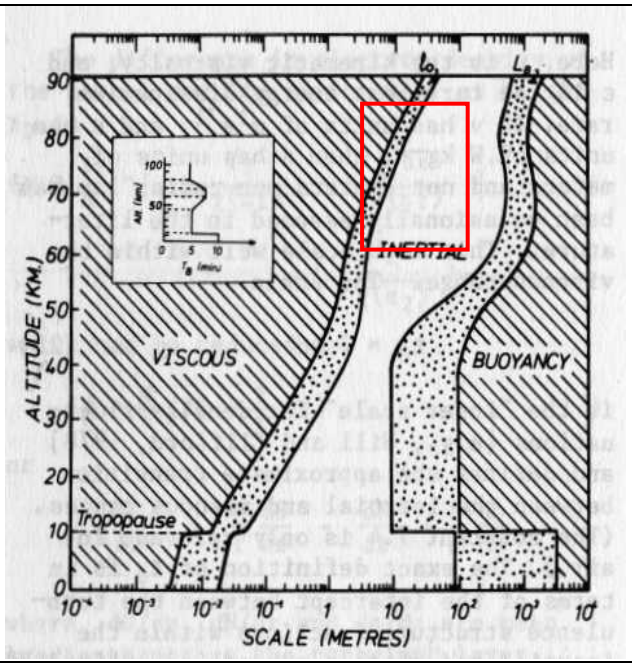

Figure 1.2 Typical scales for turbulence in the atmosphere [Hocking, 1985]

1.3.3 Spectral width method to estimate ε and K

The energy dissipation rate ε of turbulence affects radar signal and the root mean square (rms) fluctuating velocity of scatterers (Hocking, 1985). Spectral width is a measure of the rms fluctuating velocities averaged from the smallest scales up to the thickness of the observed volume (e.g. 150 m), which is mostly in the inertial subrange. This is why ε can be estimated using the spectral width method.

Other nonturbulent processes can also affect the spectral widths. So the observed spectral width has to be corrected. These processes include beam broadening and shear broadening. Beam broadening is the effect of mean motions tangential to the beam direction across the finite beam width of the radar. Shear broadening is the effect of vertical shears in the horizontal winds.

Specular reflection can also affect the spectral widths. Usually we assume specular reflection is not caused by turbulence and if we use off-vertical beams, specular reflection effect is negligible

The spectral width method thus can be summarized as:

Filter out any specular reflection effect, which usually involves the rejection of large spikes in the spectra that are not in a Gaussian form.

Remove the effect of beam broadening and shear broadening:

$$\sigma_{turb}^2 = \sigma_e^2 - \sigma_t^2 \tag{1.23}$$

where σ_{turb} is the half power half width of the spectrum purely due to turbulence, σ_e is the experimental half power half width of the spectrum and σ_t is the half power half width of the spectrum due to broadening effect:

$$\sigma_t^2 = \sigma^2_{beambroadening} + \sigma^2_{shearbroadening} \tag{1.24}$$

The mean square fluctuating velocity is related to σ_{turb} by

$$< v'^2 >= \frac{\sigma_{turb}^2}{2\ln 2} \approx 0.72\sigma_{turb}^2 \tag{1.25}$$

According to the definition of total energy density $E_\xi(k)$, the total kinetic energy of turbulence should be the integral of $E(k)$ in the inertial subrange. According to Kolmogoroff theory $E(k)$ in the inertial subrange is equation 1.17 and the integral should be from k_B to k_0:

$$\frac{1}{2} < \vec{v}'^2 > \approx \int_{k_B}^{k_0} E(k) dk \tag{1.26}$$

where k_0 is the lowest wavenumber for the viscous subrange (highest wavenumber for inertial subrange) and $k_B = \omega_B / (<v'^2>)^{1/2}$ is the highest wavenumber for the buoyancy subrange (lowest wavenumber for inertial subrange).

If we assume the three velocity component contribute equally, equation 1.26 becomes

$$\frac{3}{2} < v'^2 > \approx \int_{k_B}^{k_0} E(k) dk \tag{1.27}$$

ε is related to $<v'^2>$ by

$$\varepsilon \approx c < v'^2 > \omega_B \tag{1.28}$$

By combining equations 1.25, 1.27 and 1.28, we can obtain c as a constant of about 0.4 (Weinstock, 1981), which leads to:

$$\varepsilon \approx 0.3 \omega_B \sigma_{turb}^2 \tag{1.29}$$

The uncertainty of ε estimated using this method comes from the strict assumption of isotropic turbulence and Kolmogoroff theory which requires high Reynolds numbers (Re > 1000) that may not be the case in the mesosphere. So ε is just an estimate but should be accurate to within a factor of 2 or 3 (Hocking, 1985).

For low-resolution radar measurements at JRO this method has been applied by Royrvik and Smith (1984) in comparing radar and rocket data, and a reasonable agreement has been found. The MU radar data (Fukao et al., 1994) and Gadanki radar data (Rao et al., 2001) have also been used to estimate ε using this method. The spectral width method has never been applied with the high resolution Jicamarca radar data. We expect that spectral width of high-resolution backscatter signals will help to distinguish between different regions of mixing within wider turbulence layers.

Based on the relationship with $\boldsymbol{\varepsilon}$ and K and insert equation 1.29 into 1.10, we get:

$$K \approx 0.1 \frac{\sigma_{turb}^2}{\omega_B} \tag{1.30}$$

Equation 1.29 and 1.30 will be used in this paper to estimate the turbulent parameters.

CHAPTER 2

RADAR SET UP AND DATA ANALYSIS

2.1 Radar set up

The data used in this paper are Jicamarca radar measurements during 2002-2003 (table 1.1) The parameters are given in table 2.1.

Table 1.1 Summary of the Jicamarca observation parameters

YEAR	Day number	Range (km)	Number of height levels	Time in minutes (LT)	Beams
2002	199	9.6-84.75	502	308-1044	EWSN
	200			403-1055	
	201			339-1068	
2003	64	9.6-84.75	502	400-1058	
	142			656-1059	
	143			433-1080	
	147	60-94.463	920	364-1067	
	148			373-727	
	148	9.6-94.312	2260	729-1061	
	149			366-1048	

In the daytime there are solar radiation induced electron density irregularities modulated by neutral dynamics and turbulence (by convection or shear). After sunset, recombination will remove ionization in the mesosphere, thus nighttime echoes are negligible except for meteorites above 85 km. We will only look at the data between 7 am to 5 pm (420 min-1020 min).

As mentioned in section 1.1, T_{IPP} was 1.33 ms and a baud length Δt_t was 1 μs. So the height resolution was 150 m. For 5/27-29/2003, there were oversamplings by a factor of four at 37.5 m

range intervals. The actual height resolution was closer to 250 m than 150 m because of imperfections in transmitting and receiving systems (Sheth et al, 2005).

By properly phasing each of the 64 modules of the radar, the direction of the radar can be adjusted. Its degrees from zenith are limited by the beamwidth of each module. Different quarters of the antenna can point to different directions simultaneously. The effective beamwidth is 0.7°.

Data in 2002 and 2003 used four independent antenna beams pointed 2.5˚off-zenith in geomagnetic north, south, east and west directions. The beams were excited with 64 baud complementary coded pulse pairs.

2.2 Methodology

The methodology of this study on analyzing ε and K is described in Fig. 2.1. Each step will be further discussed in detail in the following sections.

First we have the Jicamarca spectral data. Using the least square fitting to Gaussian method, we obtain Gaussian shaped spectra. By calculating the second moments of the spectra, we find the spectral widths. The beambroadening effect will be removed from the spectral widths giving us spectral widths due to turbulence alone.

Our temperature data sources are Mass-Spectrometer-Incoherent-Scatter (MSIS), a model (Hedin, 1987) and Sounding of the Atmosphere using Broadband Emission Radiometry (SABER), an instrument on the NASA TIMED satellite. We will get the corresponding Brunt-Vaisala frequency and estimate ε and K using the equations discussed in chapter 1.

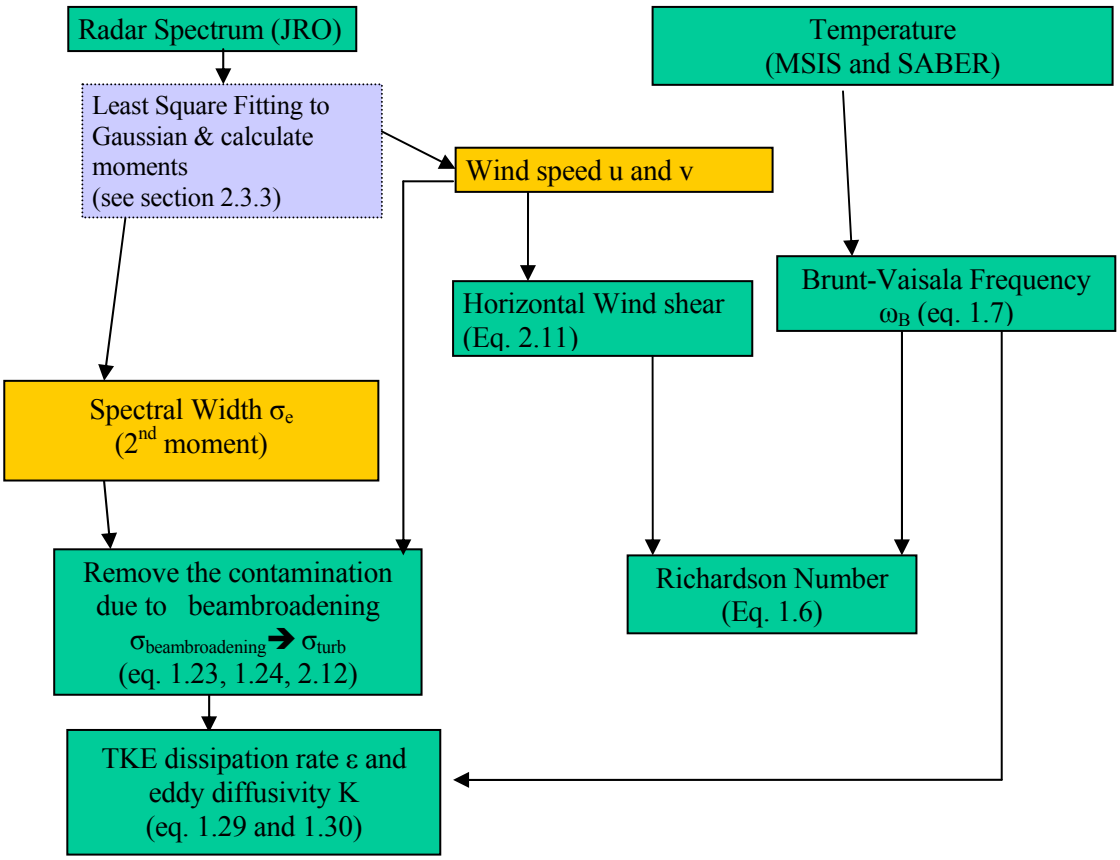

Figure 2.1 Methodology

2.3 Radar data analysis

The data we have are all processed spectra data with about 1 minute time resolution, we do not need to do the processing from raw data to spectra data. Just for the completeness of knowledge, the discussion of obtaining spectra data from raw data is included in section 2.3.1.

2.3.1 Spectra data

For 2002 and 2003, raw data from the radar are coherently integrated and decoded over blocks of 60 samples, this is called post-integration: effective T_{IPP} of 2.66 ms times 60 samples =

0.16s. Spectra data V_q are calculated from 64 discrete time series v_k, this is called incoherent integration: $0.16s \times 64 = 10.25s$. So one spectrum contains 10.25-second information. Summing up 6 spectra data incoherently makes about 1 minute, $10.25s \times 6 = 61.5s$, that's the time resolution of our data.

2.3.2 Signal to noise ratio (SNR)

SNR is defined as

$$SNR \equiv 10\log_{10}(\frac{P}{N} - 1), \tag{2.1}$$

where N (see section 2.3.2.1) is noise and P (see section 2.3.2.2) is power, it gives the information on the mean square of fluctuations in the refractive index. We set -10 dB as the threshold that only data with SNR > -10 dB are considered.

2.3.2.1 Noise

In the upper stratosphere, the backscatter cross-section is negligibly small. We set this region as our gap (table 2.2) to estimate noise (sky noise and interference). The method we use to estimate noise is simply averaging the spectra over the gap range as noise.

2.3.2.2 Power

P is the sum of the spectra at each height divided by the number of periodograms.

2.3.3 Spectral widths

There are three methods that we can use to estimate spectral widths (Sheth et al, 2005): 1) via autocorrelation functions; 2) via curve fitting (least square fitting) the spectra to a Gaussian model; 3) via calculating the second moment of the spectra. The third method doesn't work well in low SNR cases.

Table 2.2 Summary of the noise gap information for each observation

YEAR	MONTH	DATE	Noise gap (km)
2002	July	18-20	40-55
2003	March	5	40-55
	May	22-23	40-55
		27	60-63
		28 (LT: 6:13 am-12:08 pm)	60-63
		28 (LT: 12:09 pm-15:42 pm)	40-55
		29	40-50

Three different least-squares fitting procedures were discussed (Sheth et al., 2005). The first one is to fit $f_q(m)$ to $g+N$. The second one is to fit $ln(f_q(m))$ to $ln(g+N)$. The third one is to fit $ln(f_q(m))$ to $g+lnN$ (the details of these terms are discussed below). The fitting results of these three procedures were compared by Sheth et al and it was believed that the third fitting procedure gives better results. In this study, we first use the third procedure to get Gaussian shaped spectra then calculate the second moment of the Gaussian spectra as the spectral widths.

The discussion of least-squares fitting is taken from Kudeki et al. (1999). It has been shown in previous studies that fitting spectra to a Gaussian process is better than a parabola. The Gaussian probability density can be written as:

$$p(V_q) = \frac{e^{-|V_q|^2/<|V_q|^2>}}{\pi <| V_q |^2>} \tag{2.2}$$

where V_q is the 64-point discrete Fourier transform of a zero-mean, complex Gaussian random process, v_k. When the periodogram $|V_q|^2$ is integrated over a large number of independent measurements, the radar spectrum D_q has a probability density function $p(D_q)$:

$$p(D_q) = \frac{e^{\frac{-(D_q - <D_q>)^2}{2<D_q>^2/M}}}{\sqrt{2\pi} < D_q > / \sqrt{M}} \tag{2.3}$$

where M is the number of incoherent integrations and $D_q = <D_q> + \delta D_q$ (δD_q is he Gaussian distributed measurement error). If $< D_q >$ can be modeled as a known function $f(m)$ of a set of unknown state parameters, m and $m_{Maximum\text{-}likelihood}$ minimizes χ^2, we call this method least-squares fitting method:

$$\chi^2 = \sum_q \frac{(D_q - f_q(m))^2}{\sigma_q^2} \tag{2.4}$$

where σ_q^2 are the diagonal entries of the covariance matrix $< \delta D_q \, \delta D_q{}^T >$. For large M, $\sigma_q^2 = <D_q>^2/M$, so that

$$\chi^2 = M \sum_q [< D_q > (D_q - f_q(m))]^2 \tag{2.5}$$

In our Matlab routines, we used a variant of steepest descent method, Levenberg-Marquardt method, to get the optimization solutions of m above.

Since in our study we used the third fitting procedure by fitting $ln(f_q(m))$ to $g+lnN$, in our case, m is $\{A, \mu, p, \sigma_p\}$ and χ^2:

$$\chi^2 = M\sum_q [\ln(D_q) - \ln N(q\delta\varpi) - g(q\delta\varpi)]^2 \tag{2.6}$$

where N is the noise (see section 2.3.2.2), $q\delta\omega$ are discrete Doppler Frequency bins, g is the generalized Gaussian:

$$g(\varpi; m) = Ae^{-\left|\frac{\varpi-\mu}{\sigma_p}\right|^p}. \tag{2.7}$$

for $p > 2$ the function is more like Gaussian, for $p < 2$, the function is more spike-like.

After the solution of $m_{Maximum\text{-}likelihood}$ is reached by using the Levenberg-Marquardt method, the spectral width is estimated by calculating the 2nd moment of $N(q\delta\omega)exp(g(q\delta\omega; m_{Maximumlikelihood}))$. The spectral width due to turbulence can be reached by using equations 1.23, 1.24 and beambroadening effect calculation is discussed in section 2.3.6.

2.3.4 Winds

The parameter μ got from the fittings is the radial velocity.

For the days with 4 beam radar configuration (Table 2.1), by using 4 beams' radial velocity values, we can determine zonal (east-west) $\bar{u}(z)$ (eastward wind is positive, and westward wind is negative), meridional (south-north) $\bar{v}(z)$ (northward wind is positive and southward wind is negative) and vertical wind:

$$\overline{u}(z) = \frac{\mu_E - \mu_W}{2\sin\theta} \tag{2.8}$$

$$\overline{v}(z) = \frac{\mu_N - \mu_S}{2\sin\theta} \tag{2.9}$$

$$\overline{w}(z) = \frac{\mu_E - \mu_W}{2\cos\theta} \quad \text{or} \quad \overline{w}(z) = \frac{\mu_N - \mu_S}{2\cos\theta} \tag{2.10}$$

where θ is the zenith angle (= 2.5°) and μ_i are the radial velocities in the N, S, E, and W radar directions. Since we use fitting to obtain the radial velocities, there are errors coming from the fitting procedure. Plus, because of the phasing cables used by the radar, there are additional errors that should be considered when looking at zonal and meridional winds.

2.3.5 Horizontal wind shear

In the calculation of the Richardson number, we need the horizontal wind shear,

$$\left(\frac{du_h}{dz}\right) = \left\{\left(\frac{d\overline{u}}{dz}\right)^2 + \left(\frac{d\overline{v}}{dz}\right)^2\right\}^{1/2} \tag{2.11}$$

2.3.6 Beambroadening effect on spectral widths

The beambroadening effects are relatively small at Jicamarca because of its small half power half width of the effective radar beam *($\delta_{1/2}$)* of 0.7° comparing to MU's 1.3° and Gadanki's 1.5°. For most of the days, the beambroadening effect is less than 0.7 m/s, and mostly

$$\frac{\sigma^2{}_{beambroadening}}{\sigma_e{}^2} < 7\%$$

$$\sigma_{beambroadening} = \delta_{1/2} \frac{\pi}{180^{\circ}} | u_h | \quad \text{(Fukao et al., 1994)} \tag{2.12}$$

2.4 Temperature and Brunt-Vaisala frequency

In order to calculate the Richardson number and turbulence parameters, we need temperature information. In this study, we used MSIS (MSISE-90 and NRLMSISE-00) and the SABER temperature.

2.4.1 MSIS

The Mass-Spectrometer-Incoherent-Scatter (MSIS) empirical model was developed in the eighties (Hedin, 1987), starting with MSIS-83, then MSIS-86, later MSISE-90 and NRLMSISE-00.

MSIS-86 constitutes the upper part of the COSPAR (Committee on Space Research) International Reference Atmosphere (CIRA) 1986. Data sources include measurements from several rockets, satellites (OGO 6, San Marco 3, AEROS-A, AE-C, AE-D, AE-E, ESRO 4, and DE 2), and incoherent scatter radars (Millstone Hill, St. Santin, Arecibo, Jicamarca, and Malvern).

MSIS-86 expects inputs of day of year, Universal Time, altitude, geodetic latitude and longitude, local apparent solar time, solar F10.7 flux (for previous day and three-month average), and magnetic Ap index (daily or Ap history for the last 59 hours). Compared to GSWM, MSIS can be used to get results for the exact locations and days.

With the input, MSIS-86 calculates the following output for the specific day: number density of He, O, N_2, O_2, Ar, H, and N, total mass density; neutral temperature and exospheric temperature in 90 – 1000 km altitude region.

In this paper, MSISE-90 and NRLMSISE-00 (FORTRAN source codes available at http://uap-www.nrl.navy.mil/models_web/msis/msis_home.htm) temperatures are used.

2.4.1.1 MSISE-90

In the early nineties, MSIS-86 was revised in the lower thermosphere and extended into the mesosphere and lower atmosphere (Hedin, 1991), hence the name MSISE-90 (MSIS extended-90).

Zonal average tabulations from the MAP (Middle Atmosphere Program) Handbook 16 are the primary guide for the lower atmosphere for MSISE-90. Rocket and incoherent scatter radar data are used in the upper mesosphere and lower thermosphere.

Low-order spherical harmonics and Fourier series are used to describe the major variations throughout the atmosphere. With similar input as MSIS-86, users can get temperature and density profiles 0 – 1000 km altitude.

2.4.1.2 NRLMSISE-00

NRLMSISE-00 (Picone et al., 2002), the most recent version, developed based on MSISE-90. NRL stands for the US Naval Research Laboratory.

The main differences of NRLMSISE-00 to MSISE-90 include: the extensive use of drag and accelerometer data on total mass density, the addition of a component to the total mass density that accounts for possibly significant contributions of O+ and hot oxygen at altitudes above 500 km, and the inclusion of the SMM (Solar Maximum Mission) UV occultation data on O_2.

The output parameters of NRLMSISE-00 are the same as MSISE-90 with an extra anomalous oxygen number density.

MSISE-90 and NRLMSISE-00 temperatures needed to be interpolated to the right time resolution (1 minute). The height resolution for MSIS output is set according to JRO data as 150 m.

2.4.2 SABER

The TIMED (Thermosphere, Ionosphere, Mesosphere, Energetics and Dynamics) spacecraft mission studies the influences of the Sun and humans on the mesosphere and lower thermosphere/ionosphere (MLTI). The TIMED spacecraft was launched on December 7, 2001,

from Vandenberg Air Force Base, California, aboard a Delta II launch vehicle (Remsberg et al., 2003).

SABER (Sounding of the Atmosphere using Broadband Emission Radiometry) is one of the four instruments on NASA's TIMED Mission spacecraft. SABER can explore the mesosphere and lower thermosphere (MLT) globally extending from 60 km to 180 km. SABER helps researchers study seasonal, latitudinal and temporal variations in MLT. SABER provides the measurements of vertical distribution of infrared radiation emitted by various atmospheric gases (O_3, H_2O, N_2, CO_2) and also provides the temperature information (Remsberg et al., 2003).

The experiment technique of SABER is inversion of thermal Earth limb emission profiles measured by an infrared broadbank multispectral radiometer covering the range from 1.27 μm to 17 μm (Russell III et al., 1994).

SABER covers equatorward of 52° latitude in each hemisphere almost continuously. It scans from 52°S to 83°N during the north-looking mode for about 60 days, switches to an analogous south-looking mode, then repeat. Vertical scans are measured every 52 s, giving a profile spacing along the orbit of about 3° of latitude for 15 orbits per day (Remsberg et al., 2003).

Because of the nature of the satellite orbit, it's impossible to get the temperature profiles exactly at JRO on the days we have radar measurements, we extracted the SABER data on the days of our measurements which are geophysically the closest (< 300 km) to JRO.

Unlike models, SABER cannot provide temperature for a whole day, instead, we will only have one or two profiles each day for a certain time depending on the satellite position. Plus considering only the closest profiles, we may hardly get any profiles for a specific day at all. In order to have some profiles to calculate for all our measurements and at the same time not loosing the integrity of the data. We use some of the neighboring days data as well. There is no SABER measurements for July, 2002. We only have 2003 March and May SABER temperatures.

Despite its small number of profiles available, SABER temperatures give us more detailed layers instead of those smoothed lines provided by the models. The height resolution of SABER temperature profile is approximately 2 km (Remsberg et al, 2003) although the data we obtain are about 0.35 km apart from interpolation.

2.5 Richardson number

The likelihood of the turbulence can be evaluated by means of the Richardson's number (eq. 1.6):

$$Ri \equiv \frac{F_{bouyancy}}{F_{inertial}} = \frac{\omega_B^2}{(\frac{du_h}{dz})^2}$$

If the Richardson number is much less than 1, buoyancy is unimportant in the flow. If it is much greater than 1, buoyancy is dominant. If the Richardson number is of order 1, then the flow is likely to be buoyancy-driven.

Turbulence can be caused by shear instability ($\omega_B^2>0$, Ri >0) or convective instability ($\omega_B^2<0$, Ri <0). Shear instability may occur in a stable environment in the form of breaking waves. This occurs when Ri < 0.25. Ri may vary rapidly across this sheared boundary.

2.6 Turbulent parameters: energy dissipation rate and eddy diffusivity

With the information of ω_B and the spectral width due to turbulence, we can calculate ε and K (equation 1.29 and 1.30).

Since the values of ω_B are estimated from models and SABER temperatures, the results of ε and K for different data source will be discussed and compared.

CHAPTER 3

RESULTS AND DISCUSSION

3.1 Radar data results

The radar images from 7-17 LT, 60-85 km altitude ranges are discussed in the following sections for each day (table 1.1).

3.1.1 SNR

All the SNR images are displayed with data between -10 to 20 dB. The greater correlation between north/west pair and south/east pair is due to the overlap between mainlobes and sidelobes (Sheth et al., 2005). The north and east beams sometimes have stronger echoes. It may due to the large defects in the antenna pattern (yellow circles) in the north and east beams only (Fig. 3.1).

These defects may also generate double-peaked spectra that may give us wrong velocities (Fig. 3.2: red box). So in order to determine if the echoes are true or just artifacts, we need to look into the details of the spectra. Spikes above 80 km are due to meteor trails.

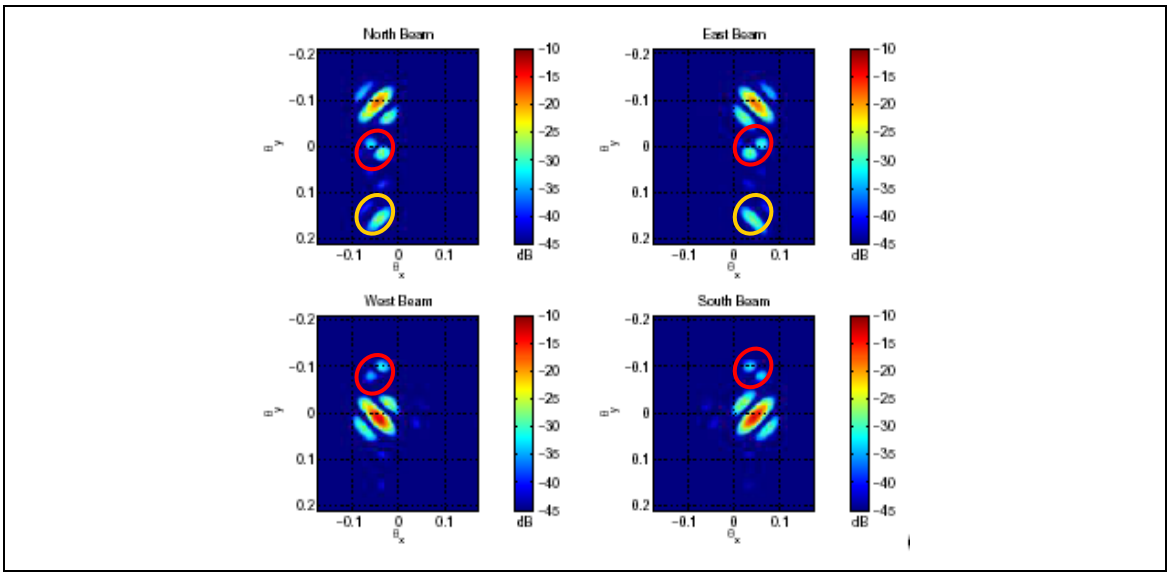

Figure 3.1 Two-way antenna beam patterns for the four beams. Direction cosines are defined as $\theta_x = \sin\theta\cos\phi$ and $\theta_y = \sin\theta\sin\phi$ where θ is zenith angle and and ϕ is azimuth angle. The yellow circles show where the large defects are. The red circles show where the small defects are. [Sheth et al., 2005]

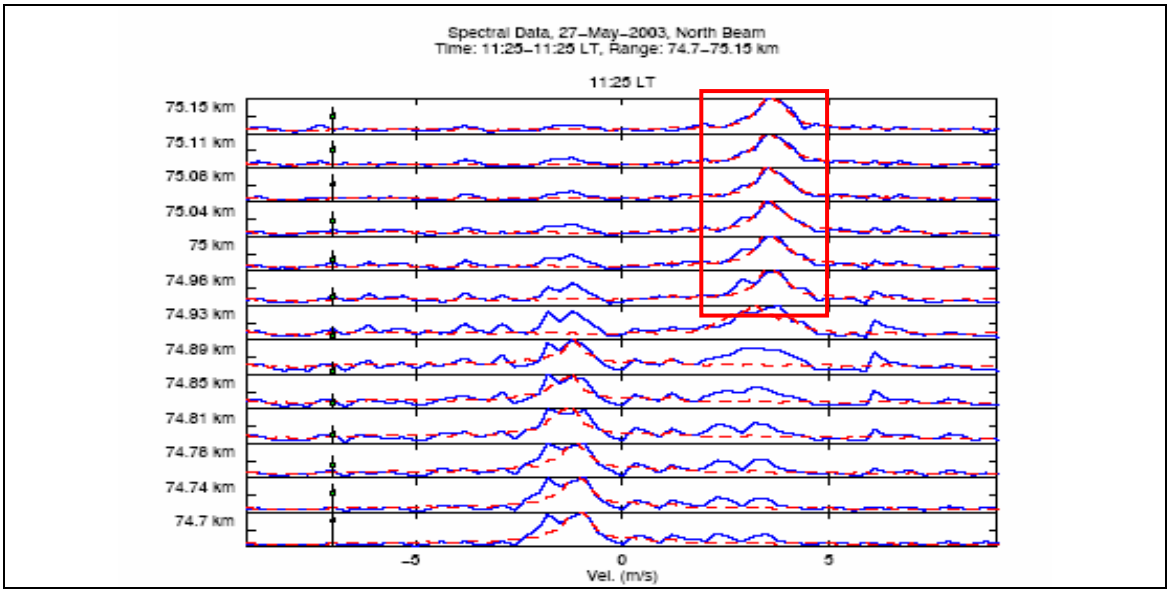

Figure 3.2 Double-peak spectra (red box) example [Sheth et al., 2005]

SNR maps for 7/20/02 (Fig. 3.3) show many blobs of turbulence from 9-17 LT. At around 77 km there is a thin sheet between 8-11 LT, between 12-15 LT it gets spreaded. In the region 67-75 km, between 10-17 LT, there are several strong turbulent blobs which last less than 1 hour. Around 65 km, there are two thin sheets and one of them gets thicker at 15-17 LT which is not obvious in the south beam.

The SNR maps from 3/5/03 (Fig. 3.4) show several blobs in 70-77 km altitude and one relatively thick small sheet continued about 3 hours at 75 km. At around 68 km there is a thin sheet in north and east beam.

The 5/23/03 SNR maps (Fig. 3.5) show two thick descending layers with strong echoes: one from 9-12 LT and a more continuous but weaker one from 12 to 17 LT, at 70-75 km.

SNR maps from 5/27/03 (Fig. 3.6) show a thick layer above a narrower layer lasting almost 8 hours.

The SNR maps (Fig. 3.7) from 5/28 are combined by two parts with different height resolution (table 2.1). There is a main thin layer at 73 km and more blobs the second half of the day.

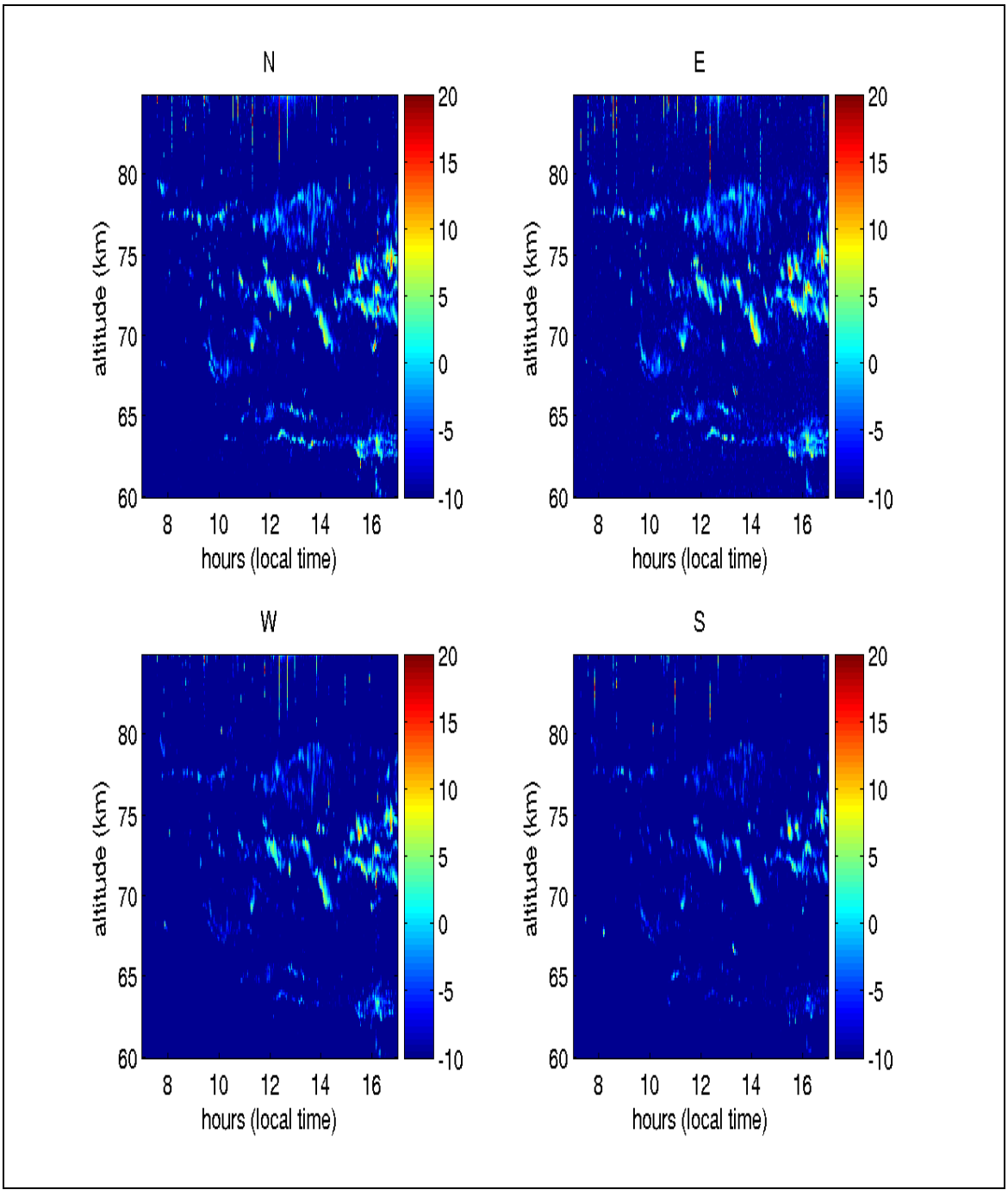

Figure 3.3 SNR maps from 7/20/02 for the north, east, west and south beam

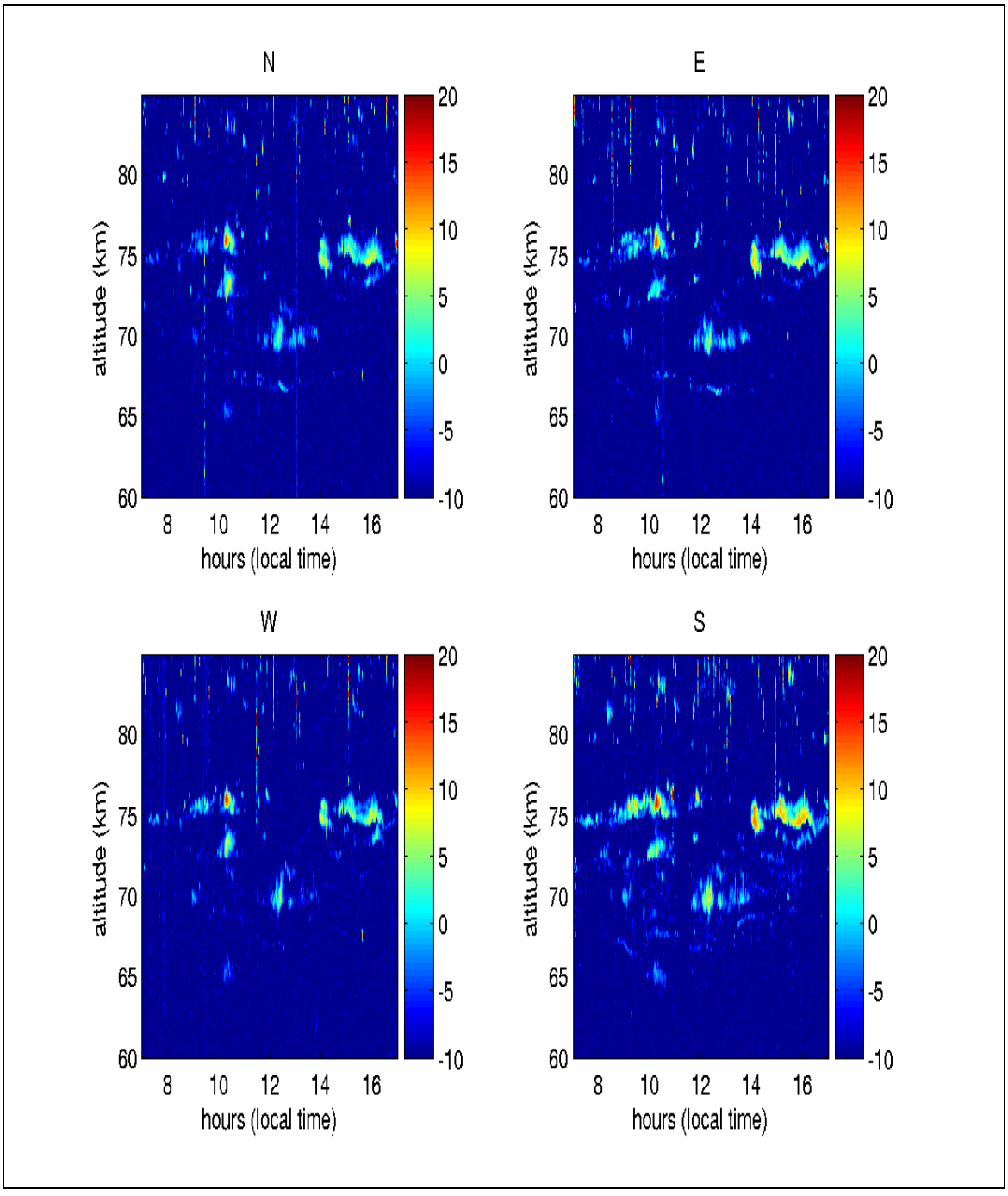

Figure 3.4 SNR maps from 3/5/03 for the north, east, west and south beam

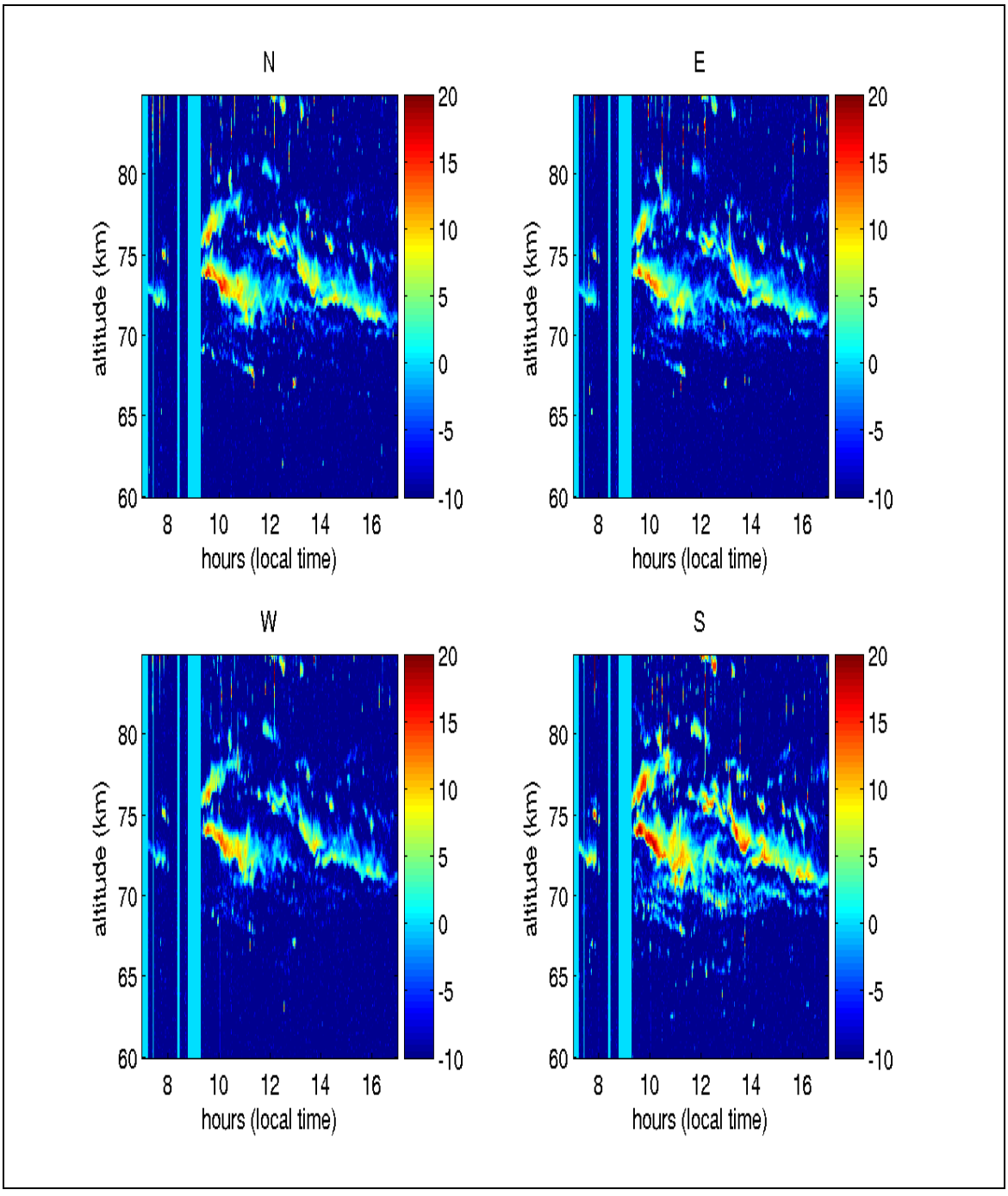

Figure 3.5 SNR maps from 5/23/03 for the north, east, west and south beam

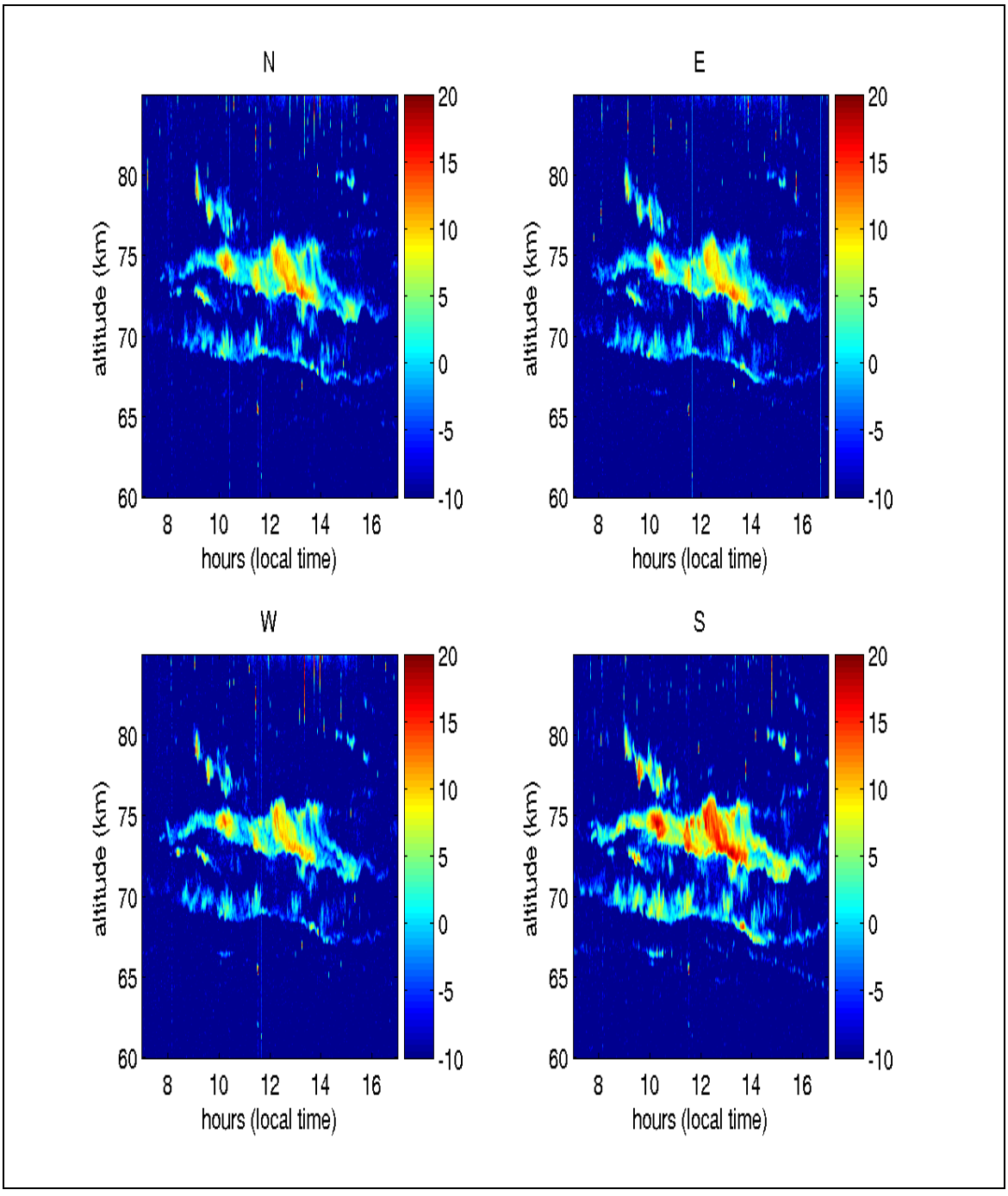

Figure 3.6 SNR maps from 5/27/03 for the north, east, west and south beam

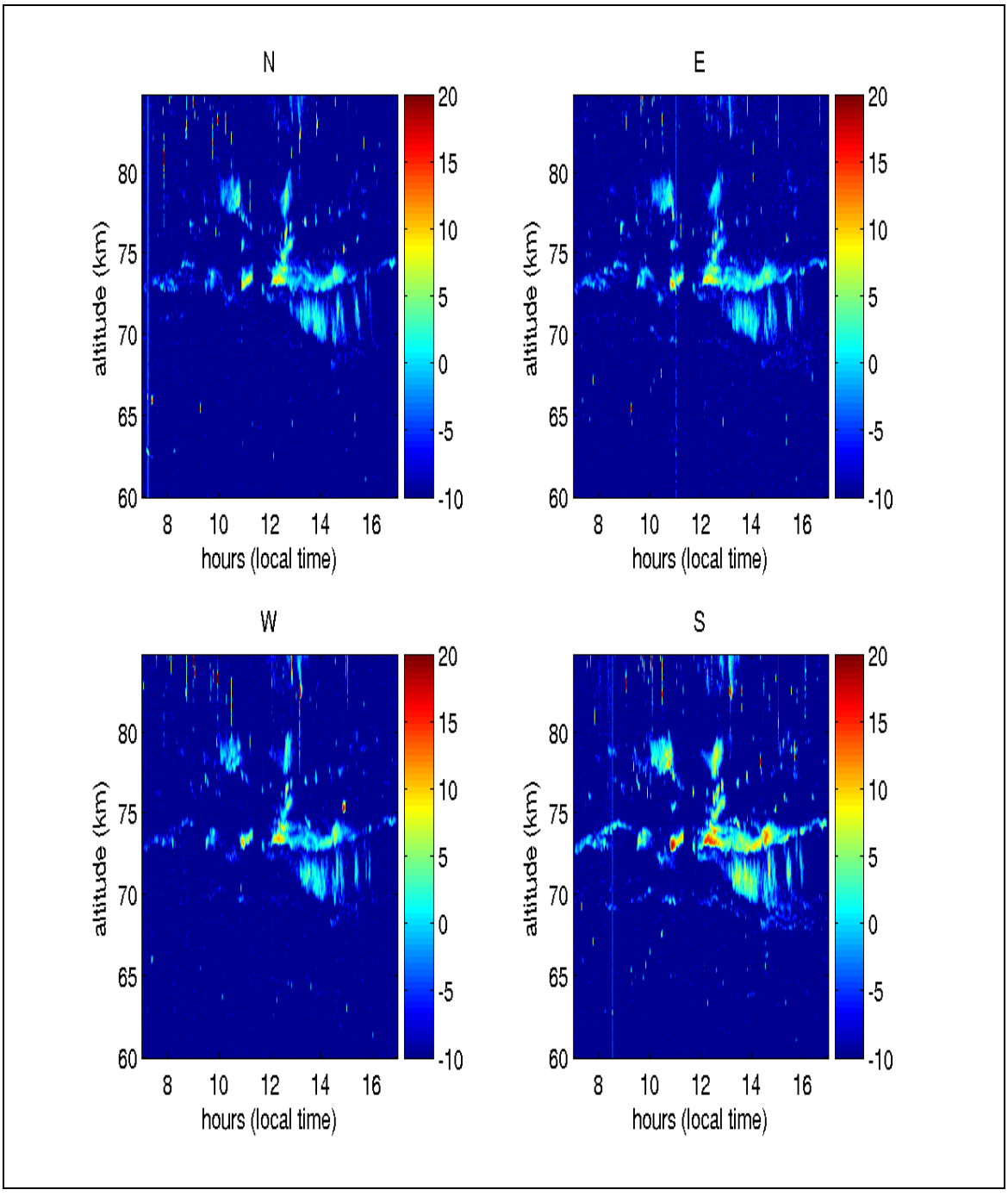

Figure 3.7 SNR maps from 5/28/03 for the north, east, west and south beam

3.1.2 Winds

Zonal and meridional wind maps are shown with wind less than 30 m/s.

7/20 wind maps (Fig. 3.8) have similar features as the SNR maps. There are strong negative zonal winds all day just like 7/18 and 19. The difference is that there are negative meridional winds at 70-75 km and positive meridional winds at around 78 km, 12-14 LT. This may suggest tide.

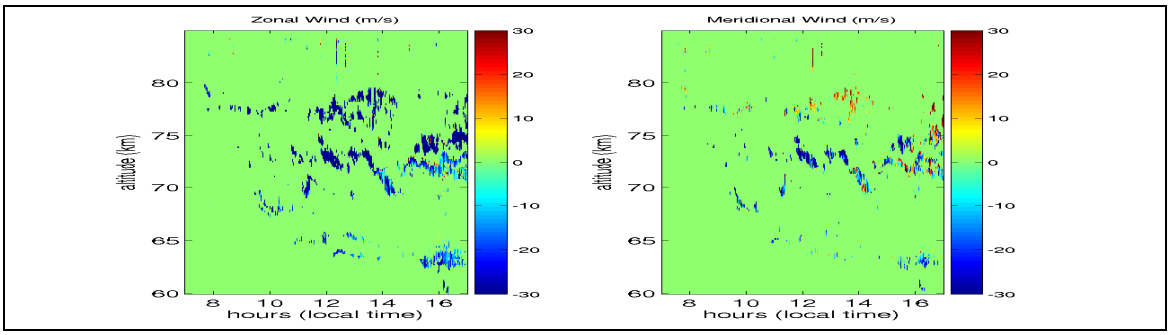

Figure 3.8 Wind maps for 7/20/02

The wind maps for 3/5/03 (Fig. 3.9) show the similar structures as the SNR maps. There seem to be wind shear at around 10 LT, 73 km and 14-16 LT, 75 km.

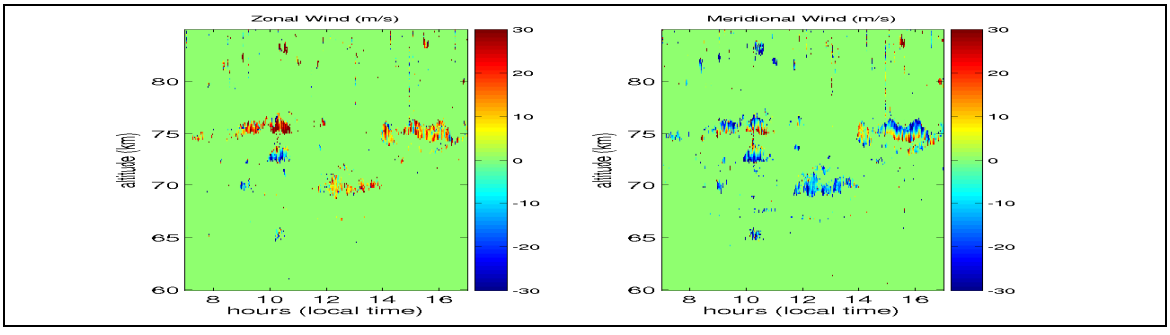

Figure 3.9 Wind maps for 3/5/03

The 5/23/03 wind maps (Fig. 3.10) show strong wind shears in both zonal and meridional direction. At around 70 km, winds are negative, to about 75 km winds are positive, and there is also a change of direction at about 77 km 10-12 LT.

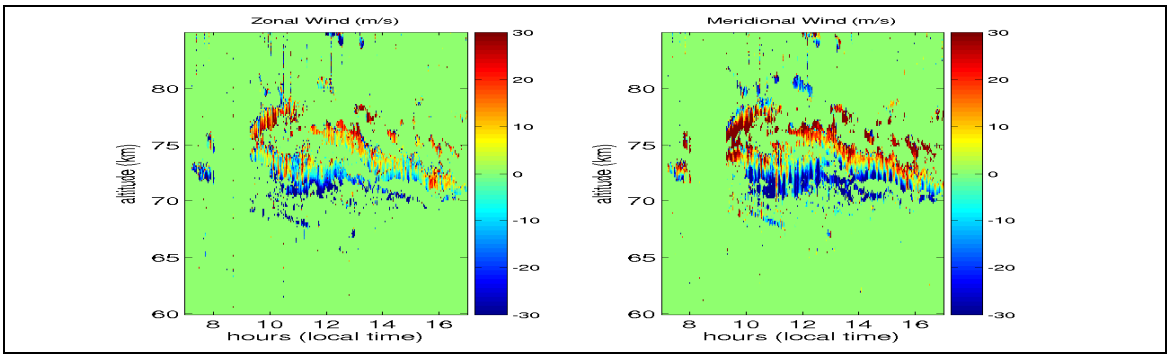

Figure 3.10 Wind maps for 5/23/03

There are strong wind shears in meridional direction lasting at least 8 hours at around 73 km and 70 km in 5/27/03 (Fig. 3.11). Another direction change may be mistaken as wind shear at the top edge of the layer around 75 km is actually caused by double-peaked spectra.

There is a strong wind shear in meridional direction in the second half of the day in 5/28 (Fig. 3.12). A blob at 77 km, 10-11 LT also shows wind shear.

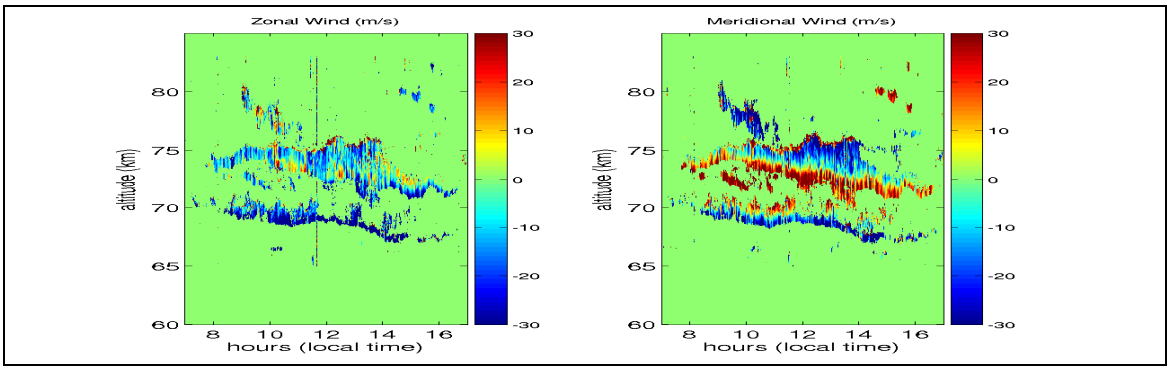

Figure 3.11 Wind maps for 5/27/03

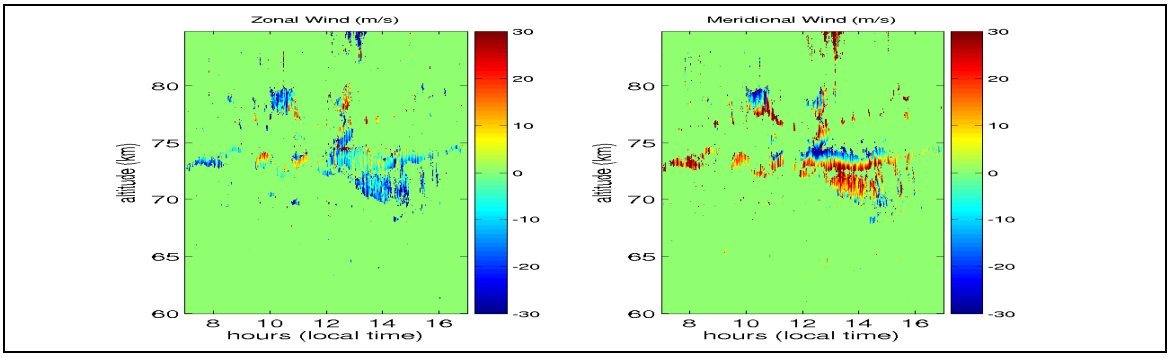

Figure 3.12 Wind maps for 5/28/03

Of all the days in May/03, meridional winds change direction vertically in the 74-77 km region. Sometimes wind shears occur even at some lower region, 71 or 72 km. Below the altitude 71 km, wind shears in meridional winds are rarely seen.

3.1.3 Beam broadening and spectral widths

Radar spectral widths σ_e images are shown in the scale between 0 to 2.5 m/s. The beambroadenings $\sigma_{beambroadening}$ are in the scale between 0 to 0.75 m/s. The square of the half power half widths due to turbulence σ_{turb}^2 are in scale between 0 to 5 m^2/s^2.

The σ_e map for each beam from 7/20/02 (Fig. 3.13) is similar to the SNR maps on the main structures. The variations in all the layers are obvious. The beambroadening effect (Fig. 3.14) is stronger for the 77 km structure and the 73 km layer than the layer just below it. The weak layers at around 65 km do not have large beambroadening effect either. Consequently σ_{turb}^2 (Fig. 3.15) show not much difference between all the layers.

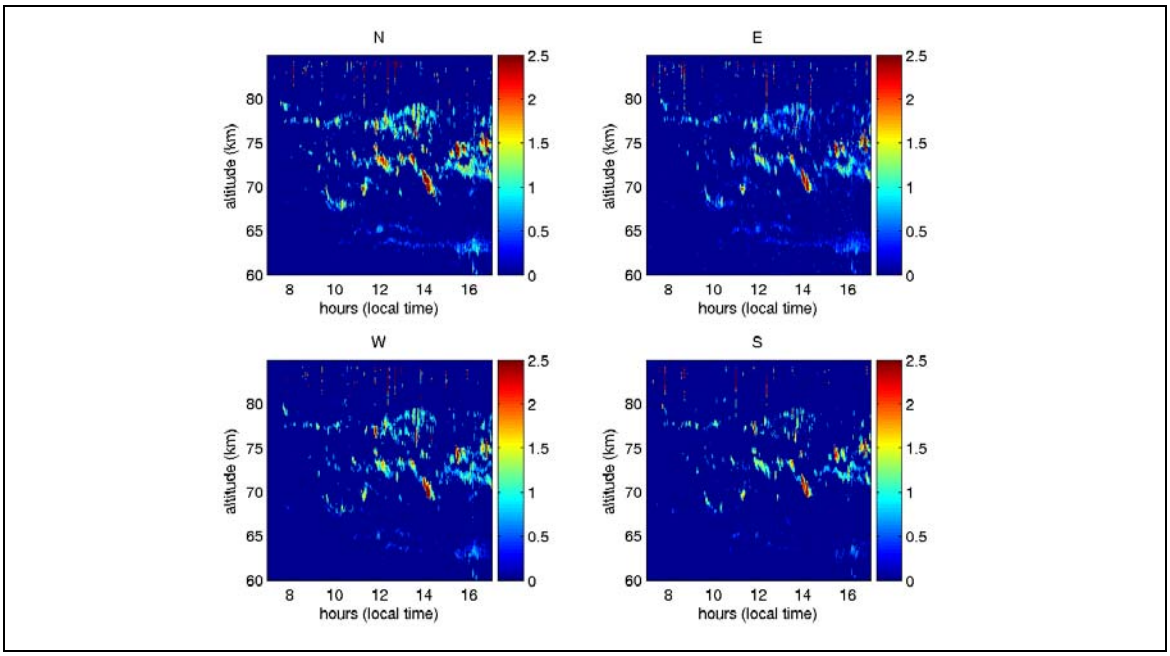

Figure 3.13 σ_e maps for 7/20/02

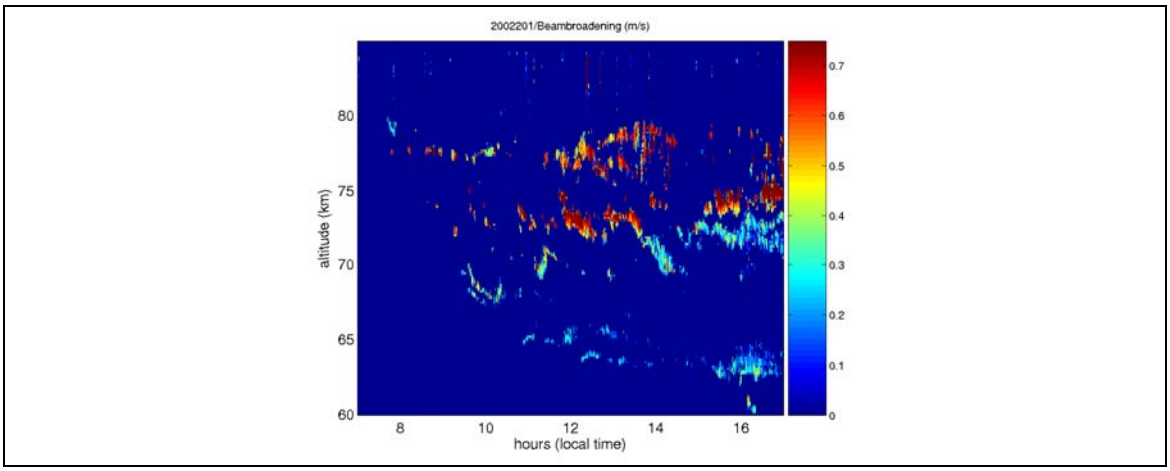

Figure 3.14 $\sigma_{beambroadening}$ map for 7/20/02

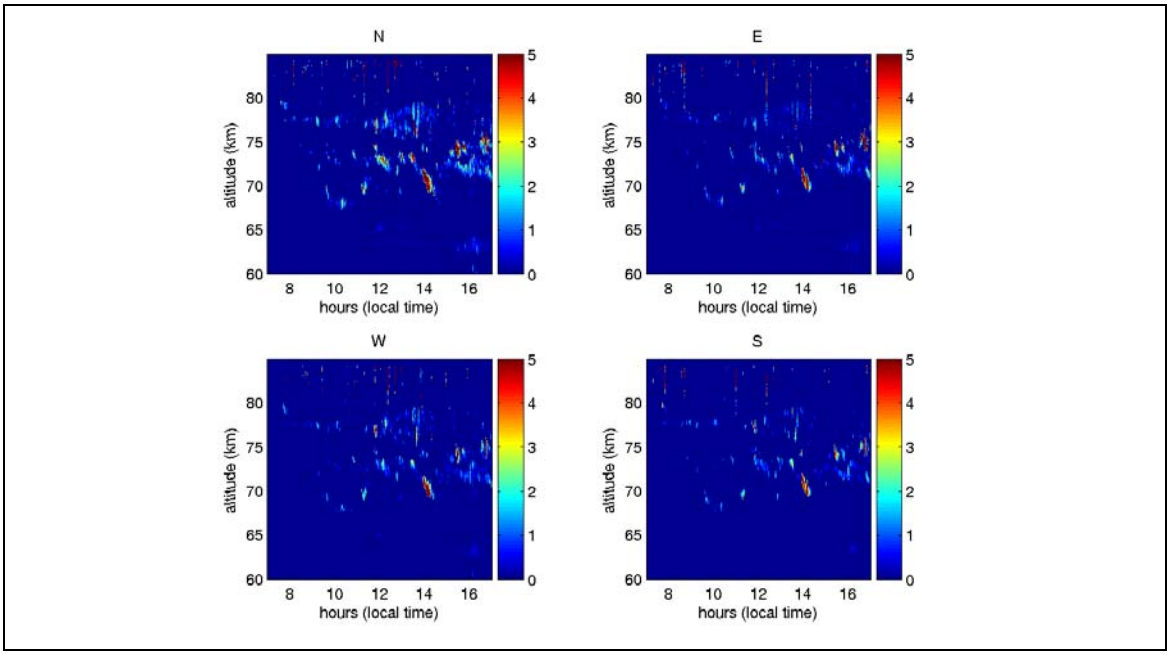

Figure 3.15 σ_{turb}^2 maps for 7/20/02

The σ_{turb}^2 map for each beam from 3/5/03 (Fig. 3.16) loses a lot of the significance of the blobs. Only the one at 75 km still remains the largest values.

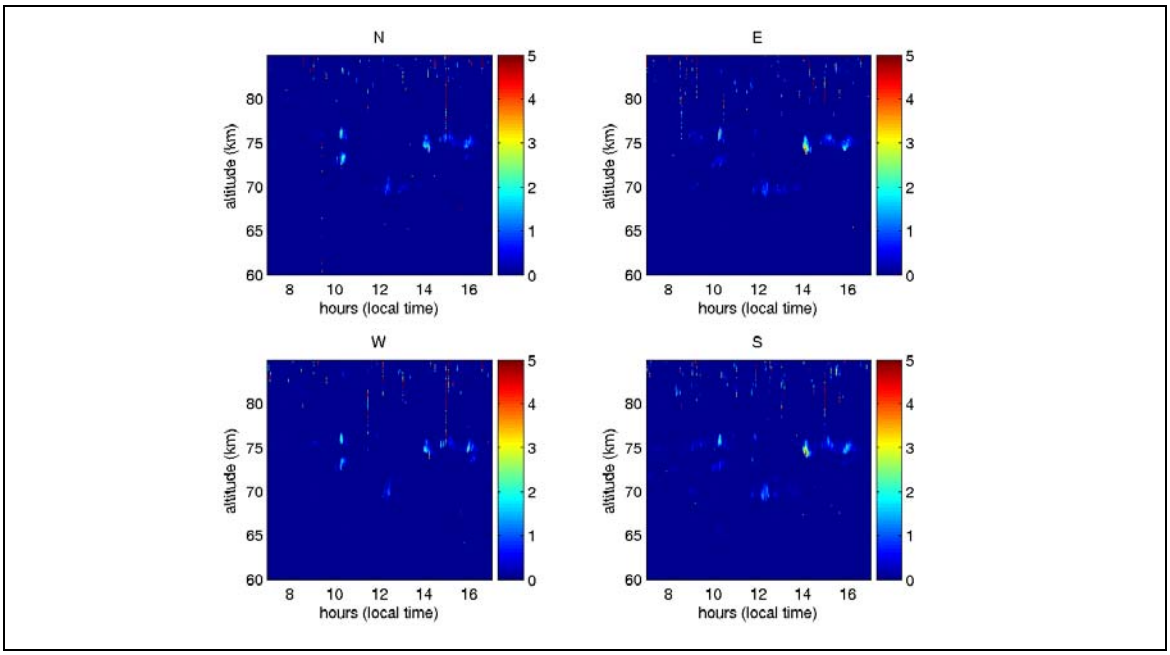

Figure 3.16 σ_{turb}^2 maps for 3/5/03

The σ_{turb}^2 map for each beam from 5/23/03 (Fig. 3.17) shows 2 descending layers similar as the SNR maps. At around 10 LT, 73 km and 76 km, the spectral widths are the largest. At 14 LT, 73 km there are also large-width spectra.

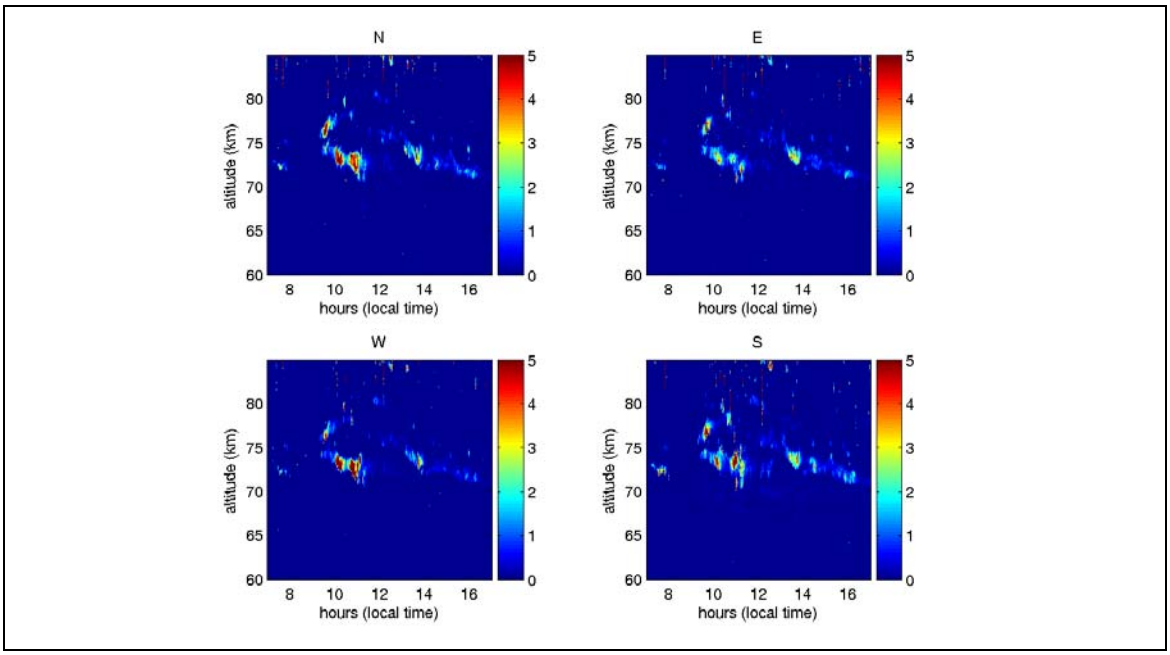

Figure 3.17 σ_{turb}^2 maps for 5/23/03

The σ_{turb}^2 map for each beam from 5/27/03 (Fig. 3.18) shows 2 layers, one thick and one thin, similar as the SNR maps. At the top of the thick layer, there are large spectral widths due to double peaks. The spectra widths of this day are generally wider than the other days we have. At the center of the thick layer, there are several regions with large spectral widths.

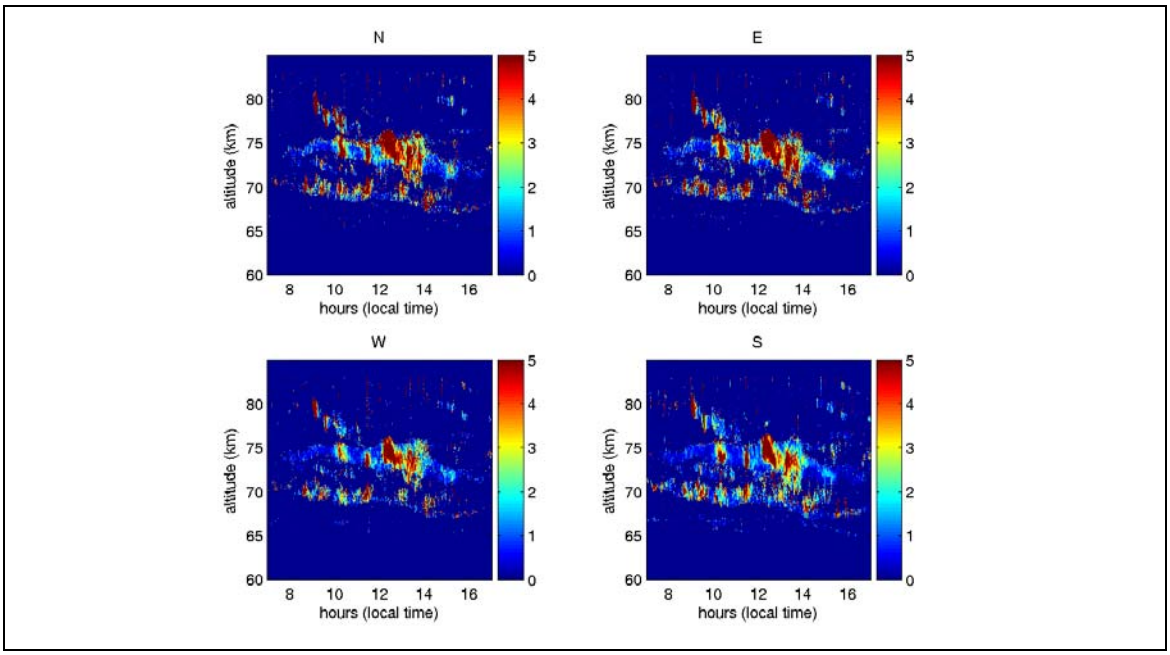

Figure 3.18 σ_{turb} maps for 5/27/03

The σ_{turb}^2 map for each beam from 5/28/03 (Fig. 3.19) shows the similar layers as the SNR maps, but the values are not quite correlated. In the SNR maps the structures have almost the same SNR values, while in σ_{turb}^2 maps, some of them have much wider spectrum than the others.

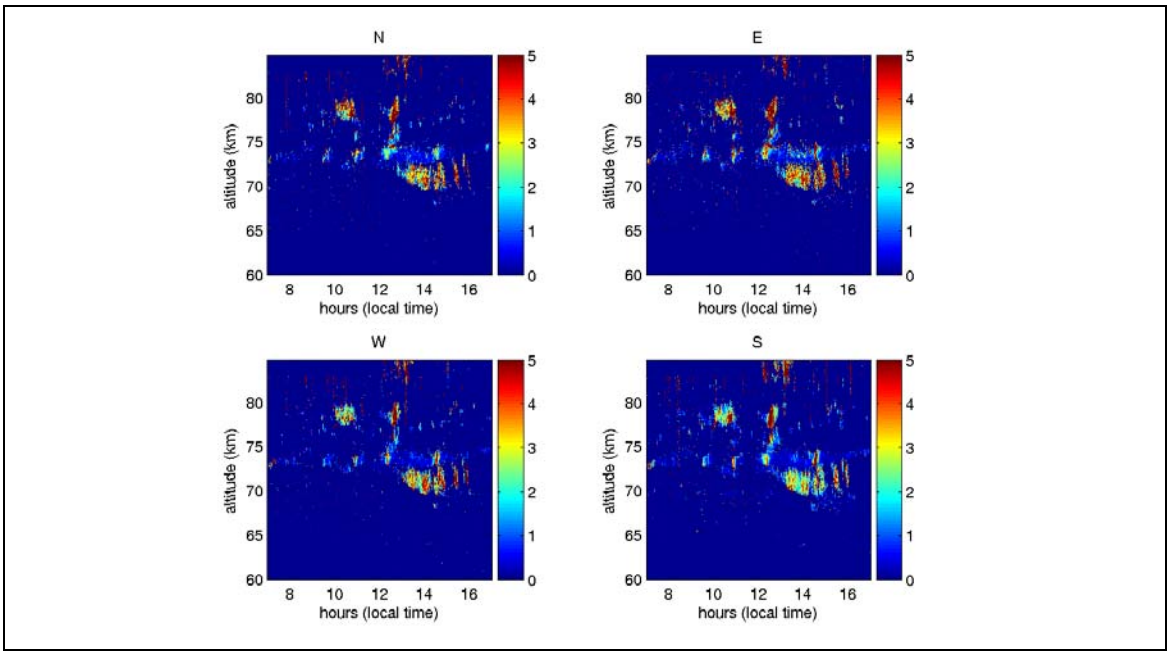

Figure 3.19 σ_{turb}^2 maps for 5/28/03

3.1.4 Wind shear

The horizontal wind shear du_h/dz images for each day are shown in the scale from 1-100m/s/km. Mostly the wind shears are the strongest at the edge of the layers or the blobs, which is very natural considering zero wind field above or below the layers. In some of the days, there are strong wind shears in the middle of the layers or blobs.

The wind shear map of 7/20/02 (Fig. 3.20) shows strong wind shear at the edges of two main layers at 77 km and 73 km. The weak layers in the SNR maps (Fig. 3.3) have weaker wind shear at 65 km. Not considering the spikes above (the red line) 80 km. The largest wind shear data are just below 75 km.

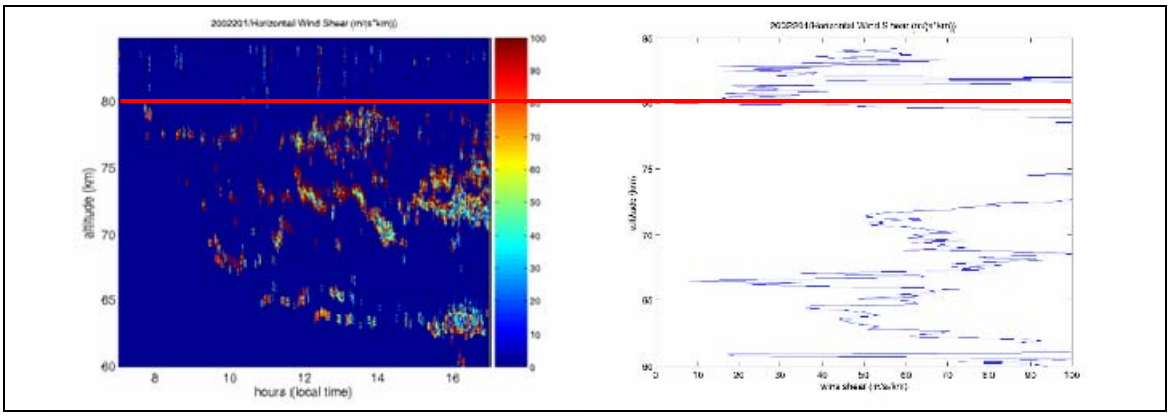

Figure 3.20 7/20/02 wind shear (m/s/km):
left graph is the wind shear image; right plot is the wind shear median profile

The wind shear map of 3/5/03 (Fig. 3.21) shows stronger wind shear at the edges of the blobs at 75 km, 10:30 LT, weaker wind shear in the structure at 75 km, 14-17 LT, even weaker wind shear in the structure at 70 km, 12-14 LT.

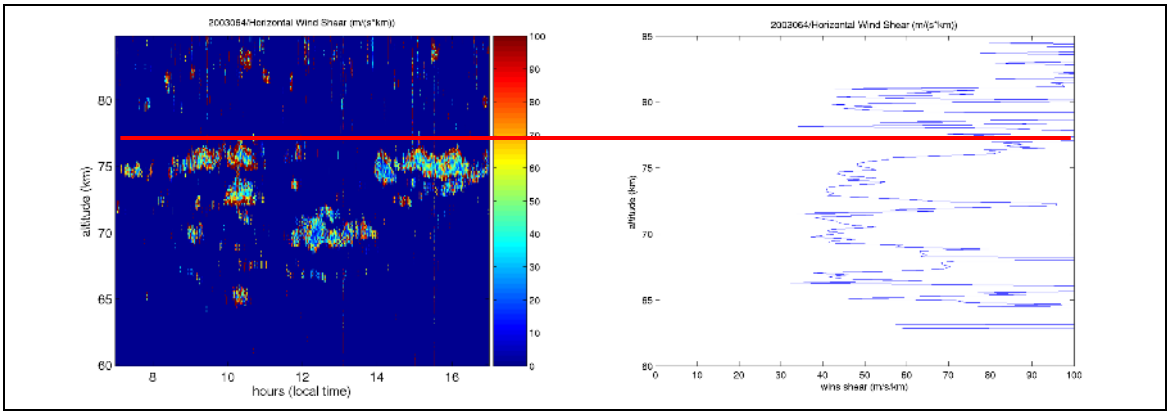

Figure 3.21 3/5/03 wind shear (m/s/km):
left graph is the wind shear image; right plot is the wind shear median profile

The wind shear map of 5/23/03 (Fig. 3.22) shows strong wind shear at the edges of the layer. At around 8 LT, there are two blobs with big wind shears too.

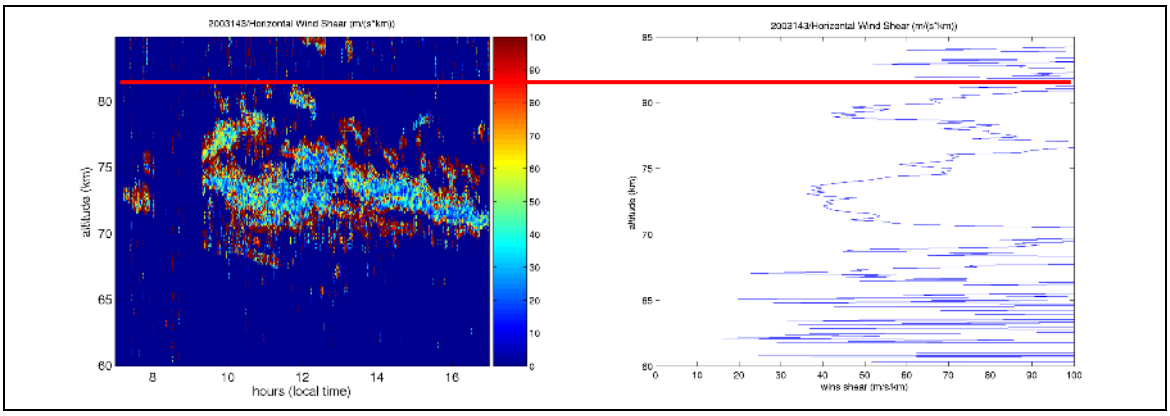

Figure 3.22 5/23/03 wind shear (m/s/km):
left graph is the wind shear image; right plot is the wind shear median profile

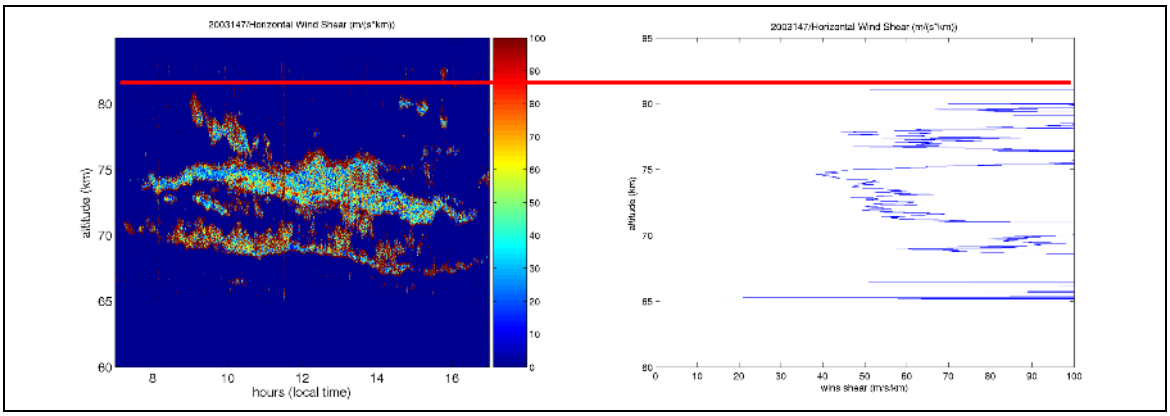

Figure 3.23 5/27/03 wind shear (m/s/km):
left graph is the wind shear image; right plot is the wind shear median profile

The wind shear map of 5/27/03 (Fig. 3.23) shows very strong wind shear at the edges of both layers. There is also one small strong-wind-shear region in the middle of the thick layer at 74 km, 13:30 LT.

The wind shear map of 5/28/03 (Fig. 3.24) shows very strong wind shear at the edges of the layers and blobs above. There is also strong wind shears in the middle of a blob at 15 LT, 70-73 km.

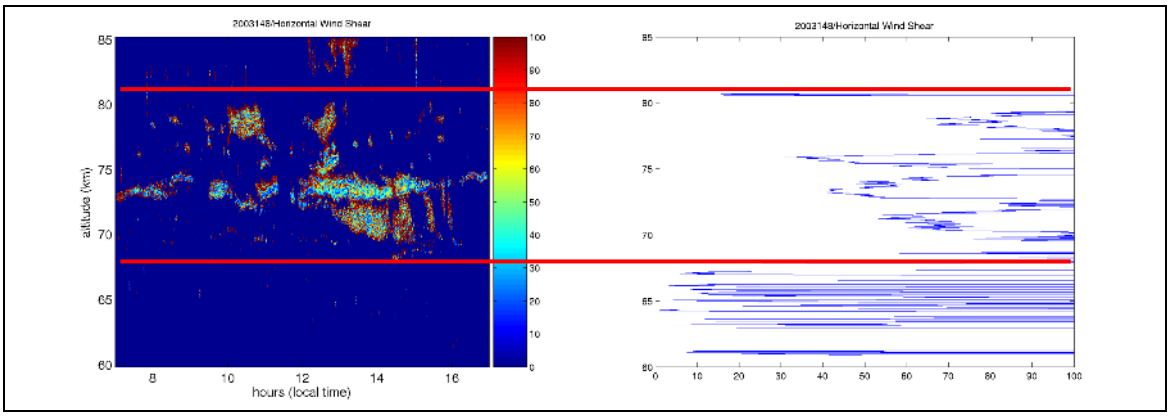

Figure 3.24 5/28/03 wind shear (m/s/km):
left graph is the wind shear image; right plot is the wind shear median profile

3.2 Temperature and Brunt-Vaisala frequency

3.2.1 MSIS

Temperature images of each of the observation day were generated from MSISE-90. One image from each month is shown below from 7-17 LT, 60-85 km. Due to the different input of F10.7 and AP index above 80 km, there is an obvious boundary at 80 km. The temperature images for the same months are similar.

Same date temperature images from NRLMSISE-00 are shown at the right of MSISE-90 temperatures in the same scale. Due to the same reason as MSISE-90, there is an obvious boundary at 80 km. The temperature images for the same month are similar.

The temperature image of July (closer to solstice) shows the largest tidal amplitude. The image of March (equinox) (fig 3.26) shows the least.

Compared to the temperature images of July/2002 and May/2003 from MSISE-90, the images of NRLMSISE-00 show larger amplitude. The March temperatures differ only slightly in the phase.

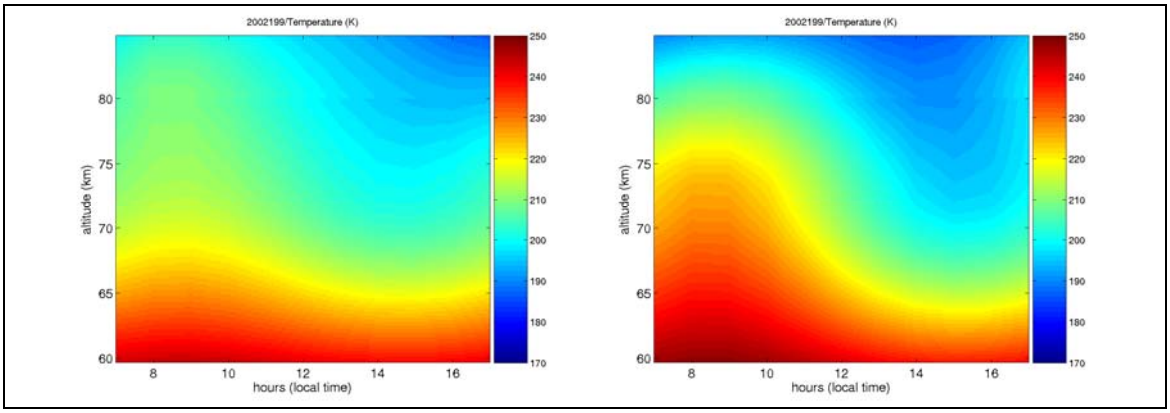

Figure 3.25 Temperature map for 7/18/02 (MSIS):
the left is MSISE-90; the right one is NRLMSISE-00

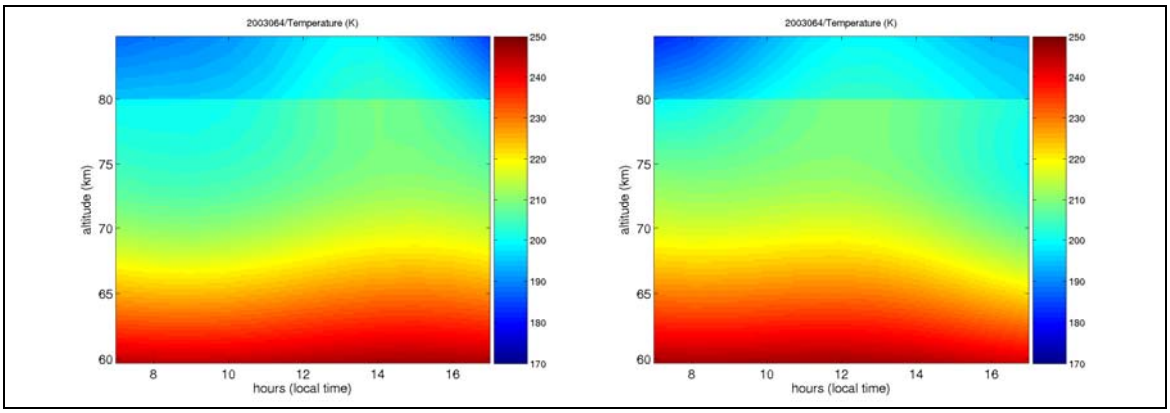

Figure 3.26 Temperature map for 3/5/03 (MSIS):
the left is MSISE-90; the right one is NRLMSISE-00

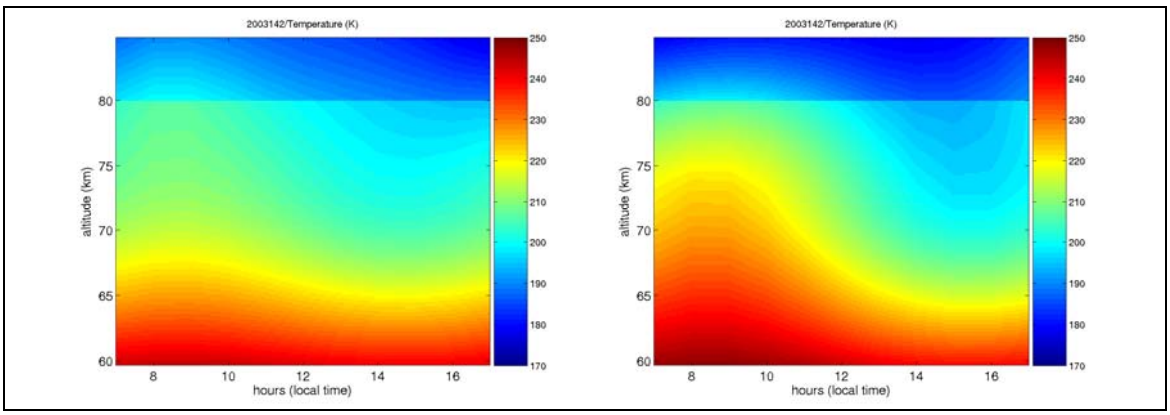

Figure 3.27 Temperature map for 5/22/03 (MSIS):
the left is MSISE-90; the right one is NRLMSISE-00

By using equation 1.7, Brunt-Vaisala frequency for each day is calculated. Examples of one day from each month of the observation are shown below. Because of the boundary of temperature profile at 80 km, there is a belt of inconsistent ω_B at 80 km. ω_B are increasing with height for all the days.

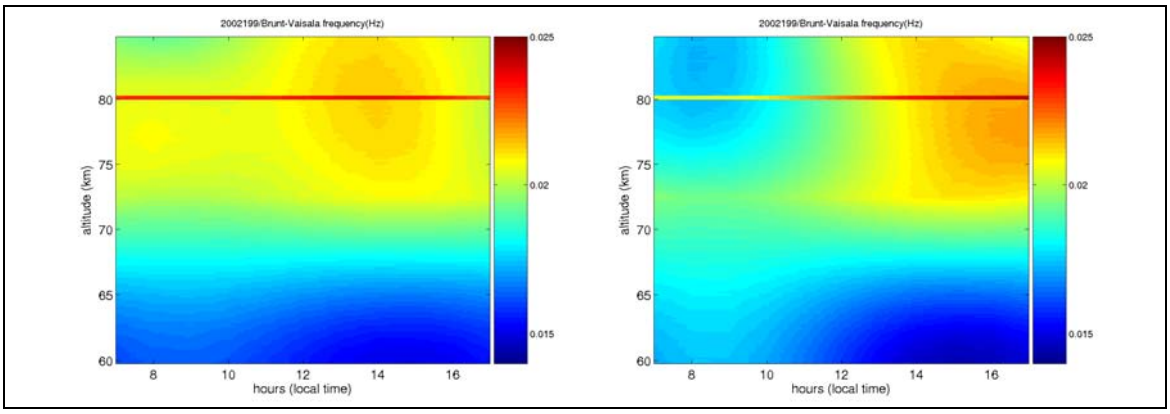

Figure 3.28 ω_B map for 7/18/02 (MSIS):
the left is MSISE-90; the right one is NRLMSISE-00

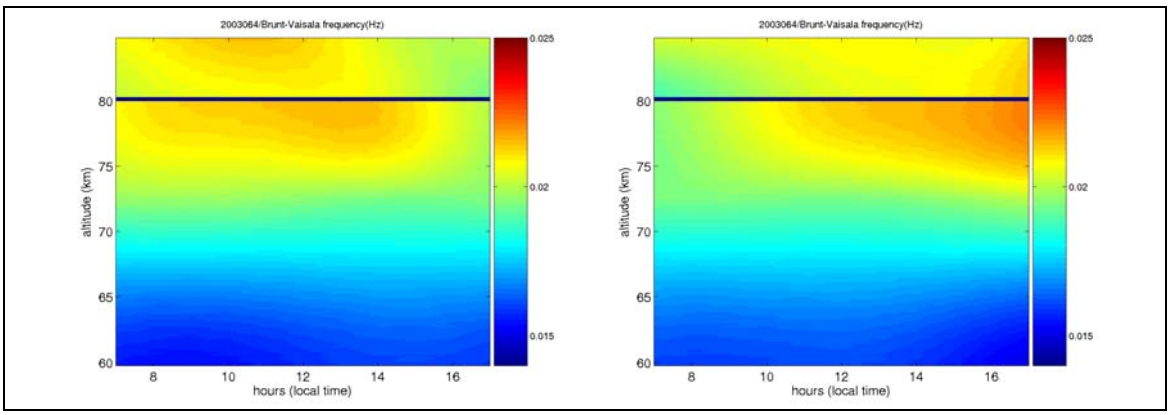

Figure 3.29 ω_B map for 3/5/03 (MSIS):
the left is MSISE-90; the right one is NRLMSISE-00

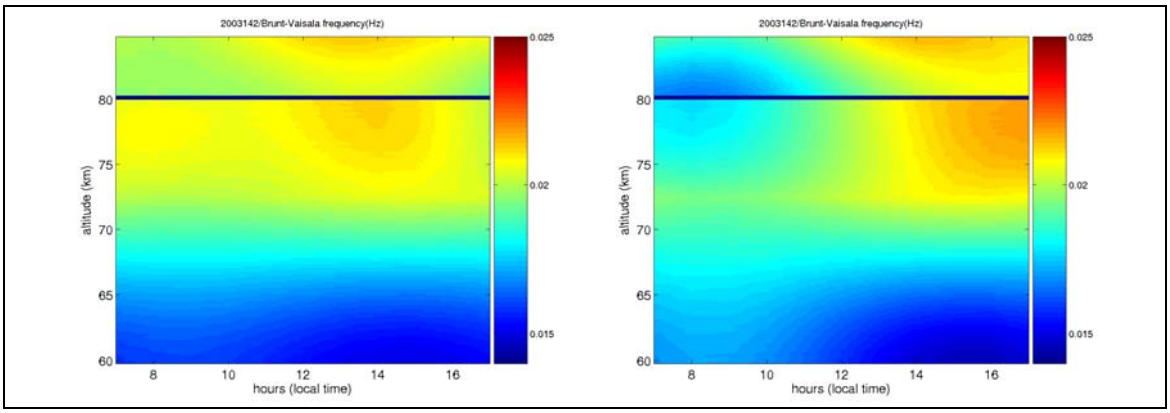

Figure 3.30 ω_B map for 5/22/03 (MSIS):
the left is MSISE-90; the right one is NRLMSISE-00

3.2.3 SABER

The temperature profiles of SABER and MSISE-90, NRLMSISE-00, GSWM temperature at the same time are shown below. The location of the SABER profile and the distance from JRO are also shown for each graph.

Among all the available data, SABER temperatures have more variation with height and usually show quite different features at different time during the same day; while for MSIS there have almost no change. GSWM data are the same for the whole month. Temperature for MSIS has a strong variation at 80 km as mentioned earlier. Because of that Brunt-Vaisala frequency ω_B for MSIS at 80 km have a sudden decreasing to less than 0. SABER ω_B are all greater than 0, indicating no convective turbulence and are appropriate for ε estimation.

For all the JRO observation days, there are only one SABER profiles that have close enough location (< 300 km) for the same day and time measurements. They are shown below (fig 3.31) compared with the same time MSIS and GSWM data. SABER temperatures decrease with height but not as much as model temperatures do. The minimum of SABER temperatures is about

195 K; while the minima of model temperatures are 170 K, 180 K and 190 K for GSWM, NRLMSISE-00 and MSISE-90 respectively. Temperature gradients for SABER are smaller below 70 km compared to above 70 km. The SABER ω_B profile (fig 3.32) decreases with height till 67 km then increase with height with much fluctuation. The MSIS profiles have inconsistent values at 80 km due to the temperature data. The tendency of MSIS profiles are increasing with height smoothly.

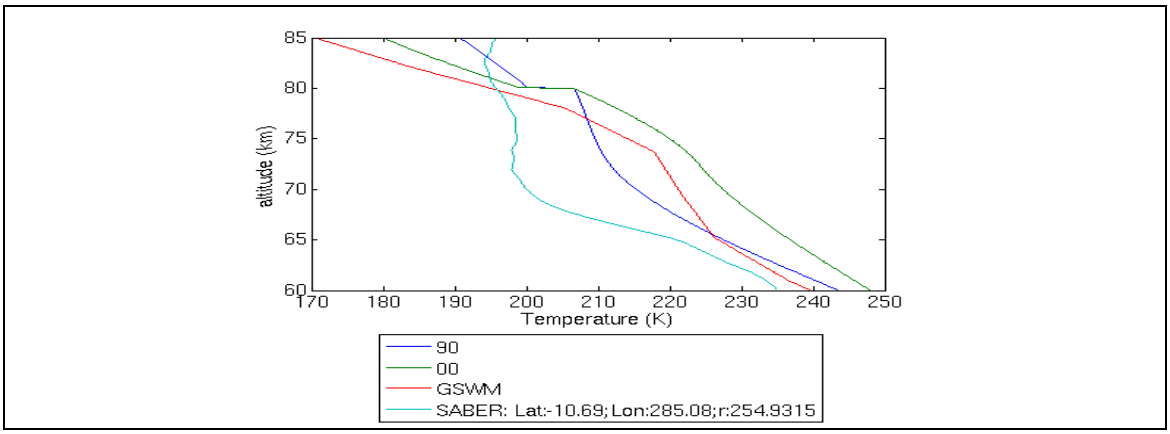

Figure 3.31 Temperature profiles for 5/28/03 at 8:32 LT

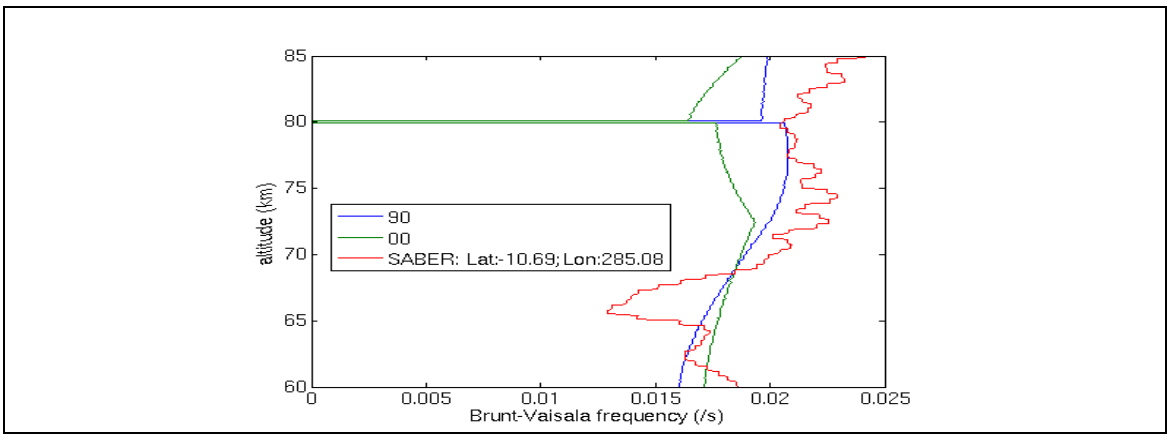

Figure 3.32 ω_B profiles for 5/28/03 at 8:32 LT

3.3 Richardson number

The Richardson numbers calculated by radar wind data and MSIS, SABER temperature are shown for some available days. All the Richardson number estimated are less than 1 and most of them are less than 0.25. There are not much difference between the Richardson numbers calculated using MSISE-90 and NRLMSISE-00. The figures shown below are all estimated using MSISE-90. Since the wind shears are the largest at the edges of the layers or blobs. Richardson numbers are smaller at the edge and larger in the middle, mostly positively correlated to SNR.

The 7/20/02 Richardson numbers (fig 3.33) have smaller values at the top of the 73 km layer and lower edge of the 64 km layer. Not considering the data above the red line (where only spikes from meteor trails can be seen), most of the Ri are very small, less than 0.25. The largest Ri occur just above 65 km.

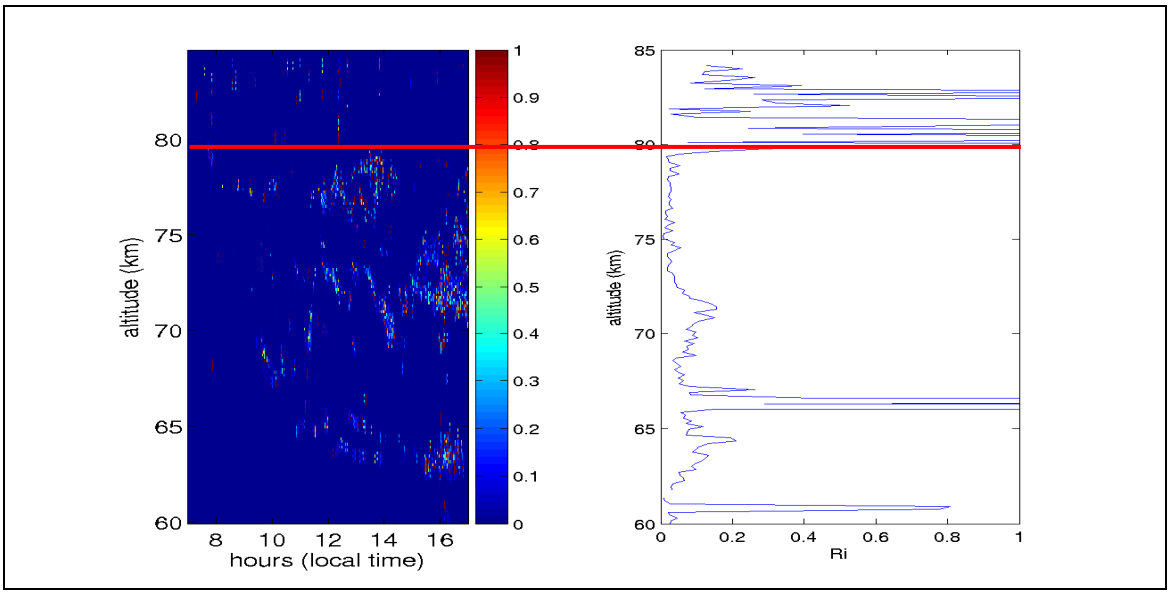

Figure 3.33 7/20/02 Ri:
left graph is the whole day image; right plot is the median profile

The 3/5/03 Richardson numbers (fig 3.34) have smaller values at the edges of the 75 km layer, 8-12 LT and a very thin stripe of larger Ri in the middle. The blob at 70 km, 12-14 LT has larger Richardson numbers. The structure at 75 km, 14:30-17 LT have smaller Ri at the top. All the Ri daily median values are small.

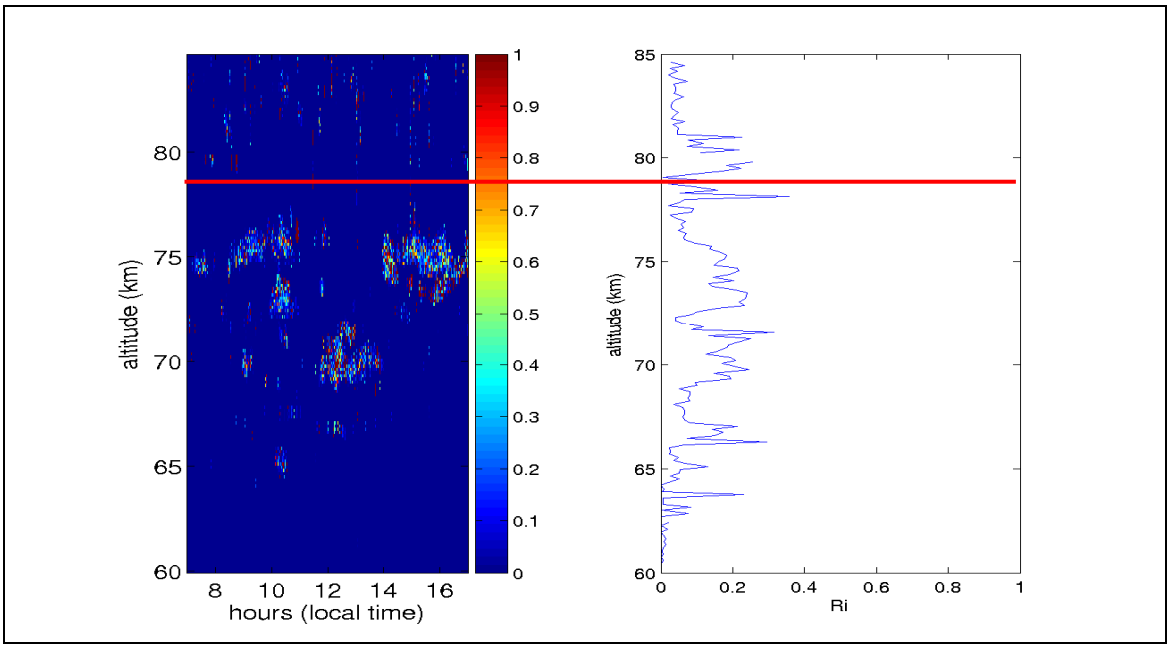

Figure 3.34 3/5/03 Ri:
left graph is the whole day image; right plot is the median profile

The 5/23 Richardson numbers (fig 3.35) have more relatively large values (mostly still < 1 though) than the previous day.

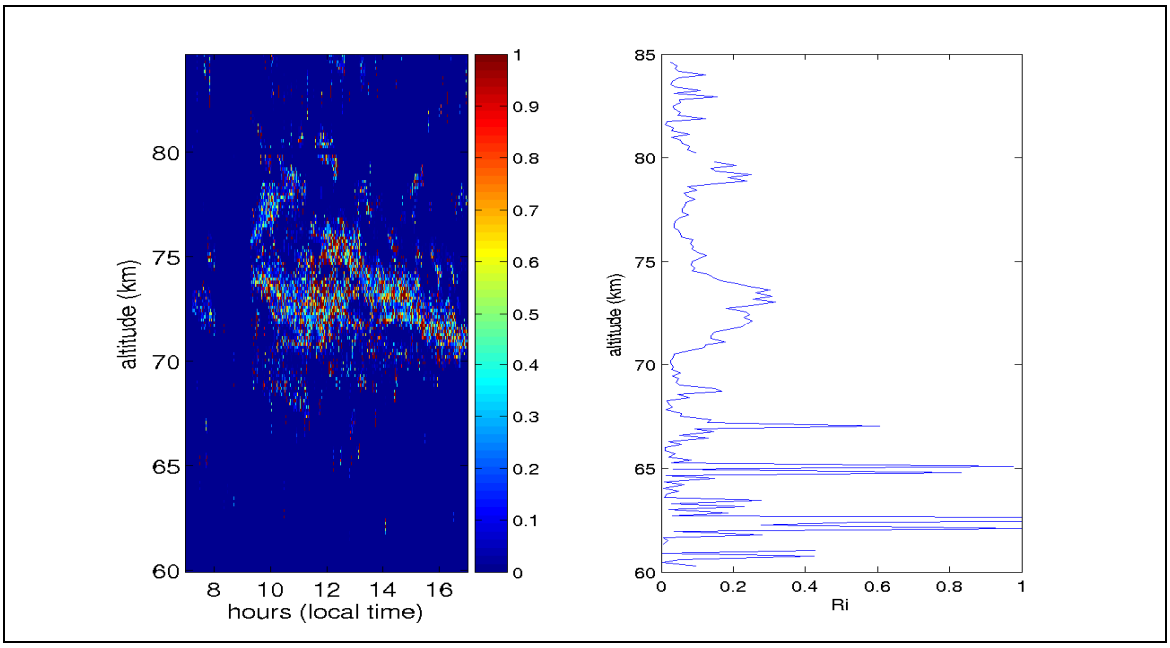

Figure 3.35 5/23/03 Ri:
left graph is the whole day image; right plot is the median profile

Compared to 5/23, the 5/27/03 Richardson numbers (fig 3.36) have more small values. At the very top edge of the long lasting layer, there is a thin stripe of small Richardson numbers due to the double peak spectra and just below it a thin stripe of larger Ri. The rest of the Ri are all very small. The large median value at 65 km can be considered as noise.

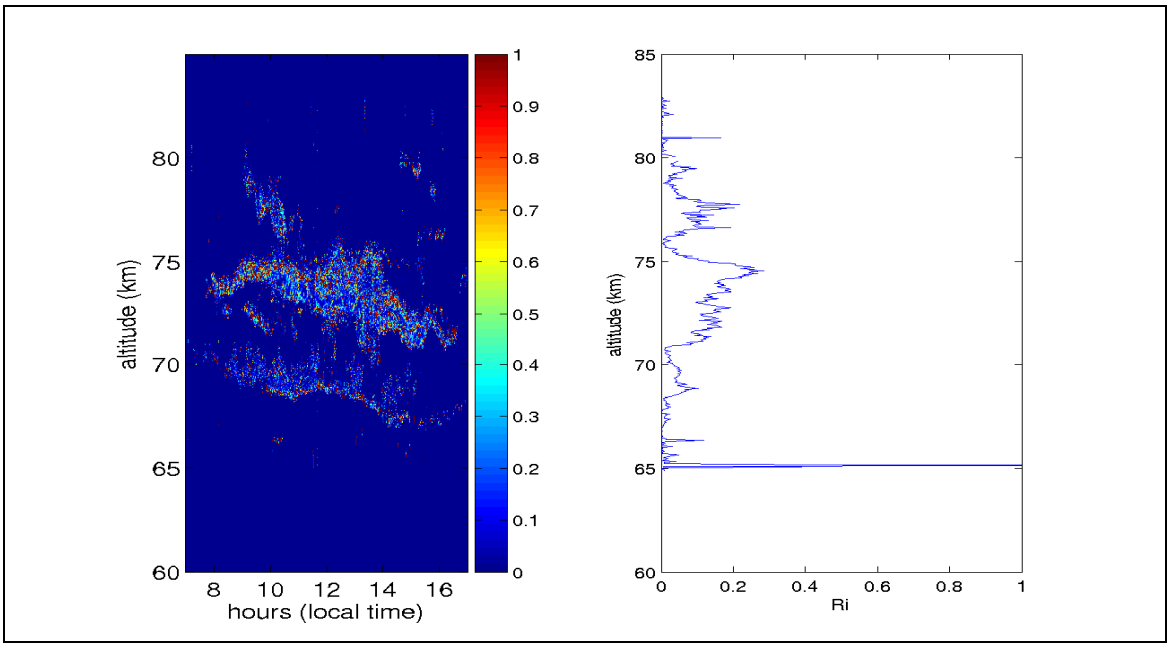

Figure 3.36 5/27/03 Ri:
left graph is the whole day image; right plot is the median profile

The 5/28/03 Richardson numbers (fig 3.37) have larger values in the first half of the day. The R_i of the two blobs at 85 km are always small. Different from a lot of other days, there are smaller values in the middle of the layer instead of at the edges. The large median values below 67 km can be considered as noise.

At 8:32 LT, there are little activities in SNR images and the Ri estimated by MSIS and SABER show less than 0.1 values below 75 km. At the layer around 80 km, Ri values are spreaded from 0.001-0.47. In general, there is not much difference between the values estimated by MSIS and SABER.

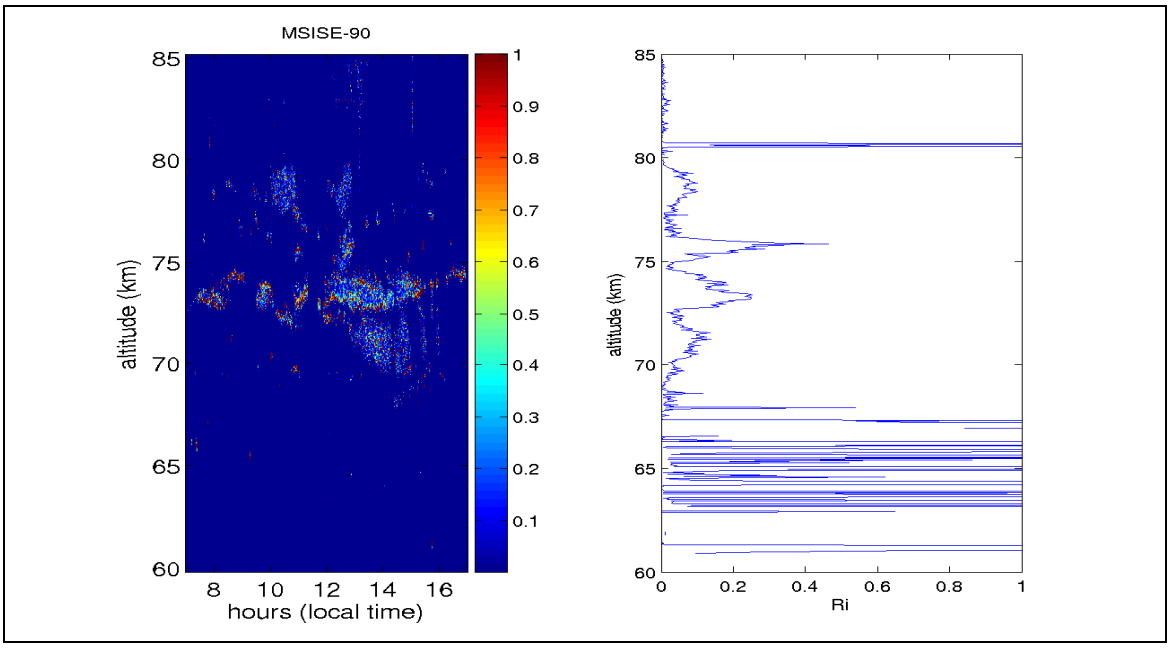

(a) 5/28/03 Ri:
left graph is the whole day image; right plot is the median profile

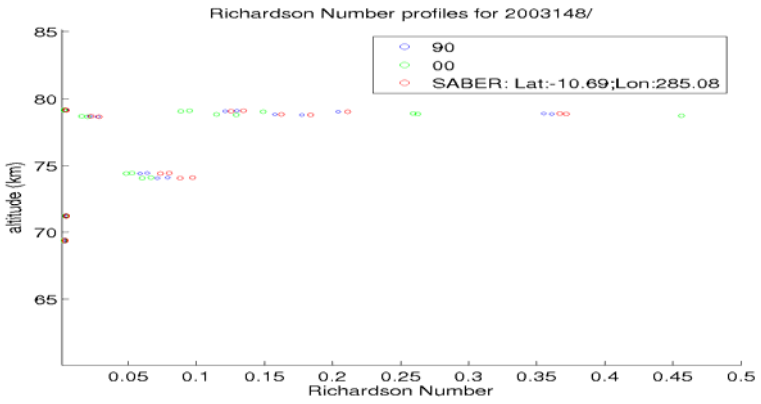

(b) Richardson numbers for 5/28/03, 8:32 LT (MSIS and SABER)

Figure 3.37 Richardson numbers for 5/28/03

3.4 Turbulent parameters: energy dissipation rate and eddy diffusivity

ε and log K are estimated using MSIS and SABER (when available) for each beam then averaged. There is not much difference between ε and K estimated using different version of MSIS. The temperature effect (ω_B) on ε and K is much smaller than the effect of spectral widths. Since daily variation of ω_B is between 0.015-0.025, which is quite small comparing to the larger daily variation of spectral widths.

Values of ε and K are mostly positively correlated. ε values are mostly less than 10 mW/kg or even smaller. For some of the days larger ε can be seen.

The daily medians of ε and K are compared with the results from MU radar and Indian radar. Since JRO is in the southern hemisphere. We compare JRO March, May and July data with September, November and January data from the other two radars respectively.

3.4.1 Daily variation

Most of the ε for 7/20/02 (fig 3.38) are less than 5 mW/kg. One blob at 70 km, 14 LT has the largest values. Log K images also have the maximum at the same altitude and time. Most of the log K values are less than 0.5 (K less than 3.2 m^2/s).

Due to the spikes above 80 km (fig 3.39), the large values of medians of ε and log K above 80 km are not considered. Daily medians of ε increase with height and have maximum of 6 mW/kg around 74 km. Then ε decrease but still have larger magnitude than the values below 74 km. Daily medians of Log K also increase with height with maximum of 0.65 (around 4.5 m^2/s) at 74 km, then decrease above 74 km.

Monthly medians of K from the MU radar (Fukao et al., 1994) January/1986 are increasing with height from 1.8-5.6 m^2/s. January /1988's K has maximum at around 75 km then decrease with similar magnitude as 1986. January monthly medians of log K from Indian radar (Rao et al., 2001)

increase with height to about 75-77 km then decrease. The magnitude of log K is from 0 – 0.6 (K is from 1-4 m^2/s. Both radars show the same magnitude of K as JRO data. The Indian radar has a similar tendency (increase then decrease with height) as JRO data.

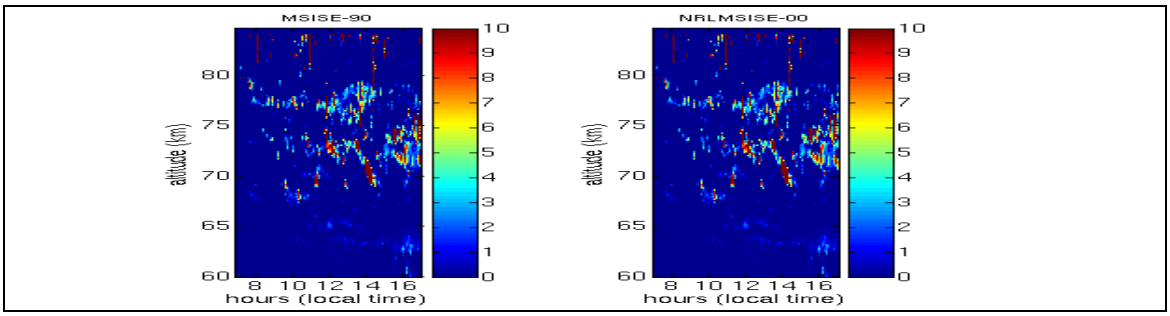

(a) ε (mW/kg) map for 7/20/02 (MSIS)

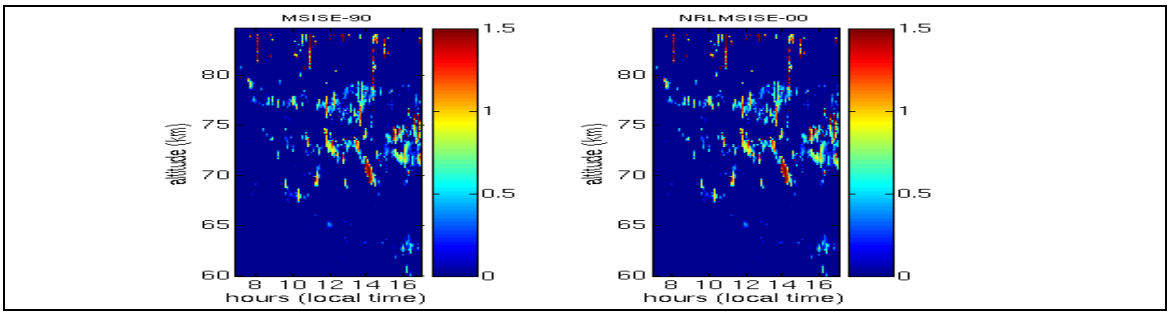

(b) Log K (m^2/s) map for 7/20/02 (MSIS)

Figure 3.38 Turbulent parameter maps for 7/20/02 (MSIS)

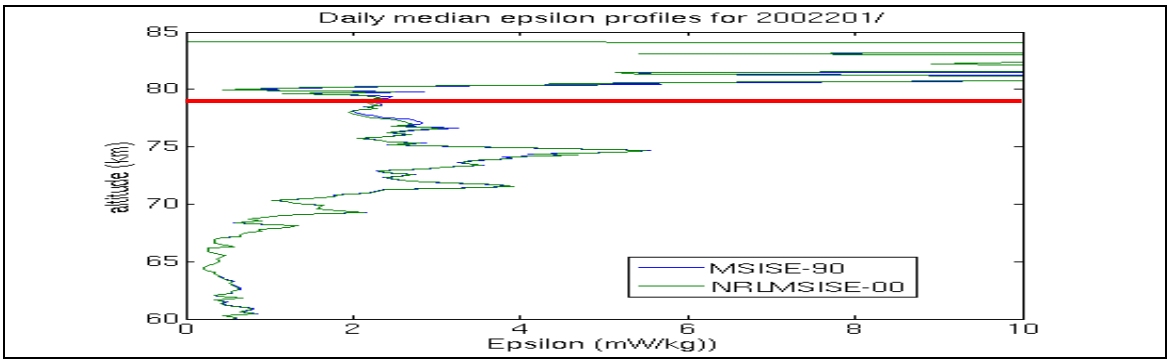

(a) ε (mW/kg) daily medians for 7/20/02 (MSIS)

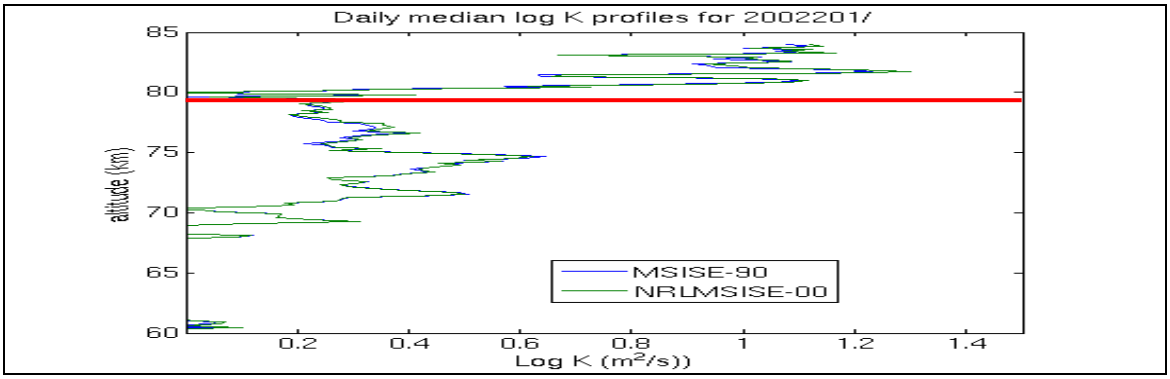

(b) Log K (m^2/s) daily medians for 7/20/02 (MSIS)

Figure 3.39 Turbulent parameter daily medians for 7/20/02 (MSIS)

Most of the ε for 3/5/03 (fig 3.40) are quite small, less than 4 mW/kg. The strongest turbulence occurs at 75 km, both 14 LT and 16 LT. Log K are also small with most of the value around 0.5.

There are some structures above 80 km. They are too weak to appear in the daily median plots (fig 3.41). Most of the values above 80 km are from spikes above and are not considered. The

magnitude of ε are small on 3/5/03, with the maxima less than 1 mW/kg at 74 km and 70 km. Log K are very small on this day the maximum is less than 0 (< 1 m^2/s).

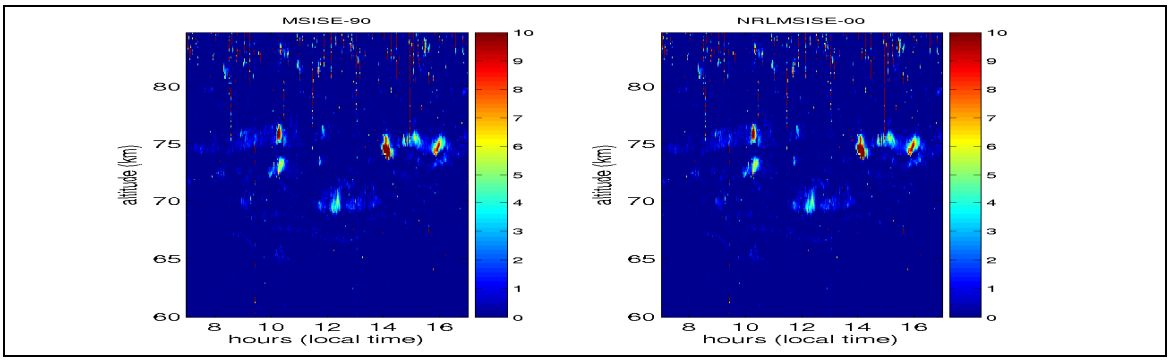

(a) ε (mW/kg) map for 3/5/03 (MSIS)

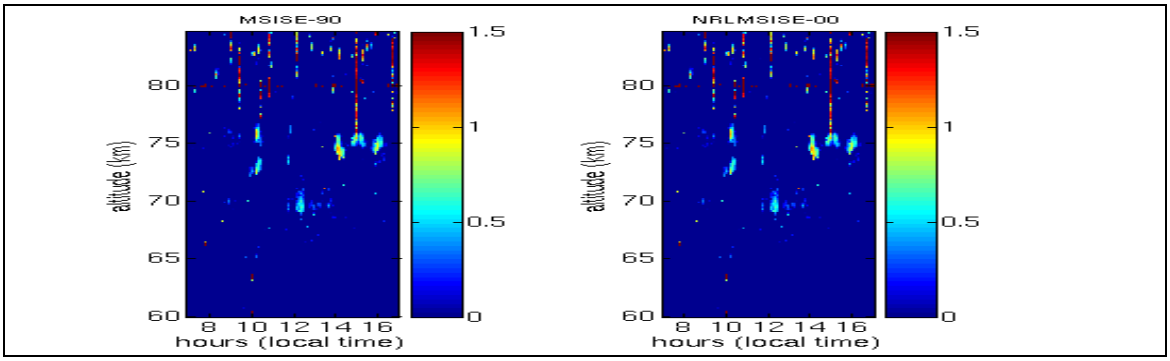

(b) Log K (m^2/s) map for 3/5/03 (MSIS)

Figure 3.40 Turbulent parameter maps for 3/5/03 (MSIS)

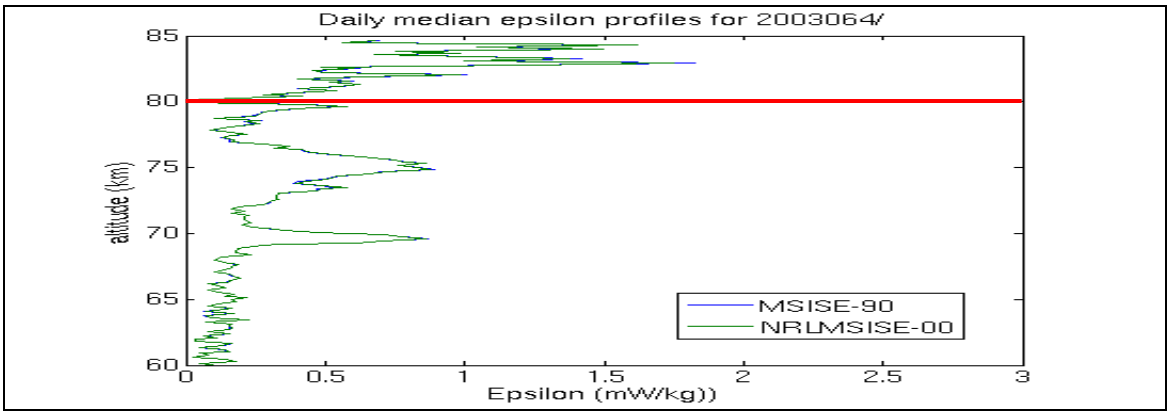

(a) ε (mW/kg) daily medians for 3/5/03 (MSIS)

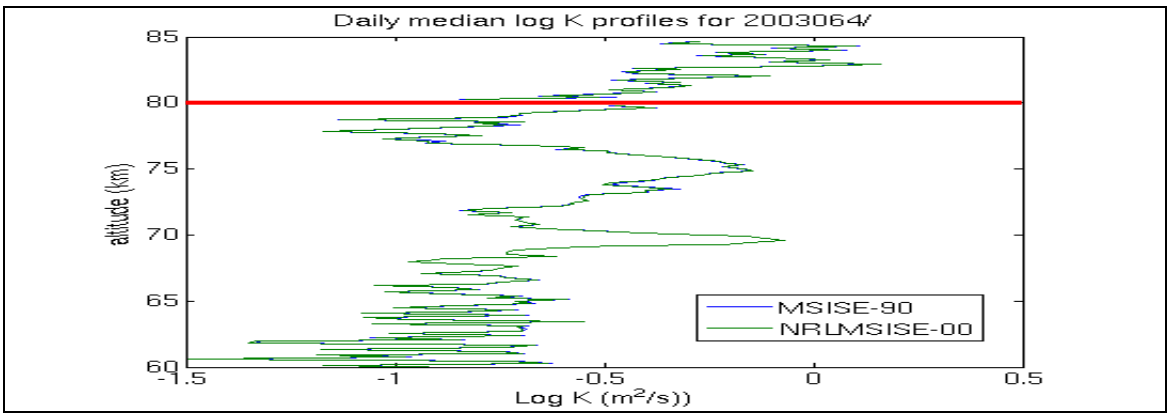

(b) Log K (m^2/s) daily medians for 3/5/03 (MSIS)

Figure 3.41 Turbulent parameter daily medians for 3/5/03 (MSIS)

September monthly medians of K from MU radar (Fukao et al., 1994) are about the same magnitude as January's data increasing with height generally with maxima at around 80 km. The magnitude is from 1.8-5.6 m^2/s. September monthly medians of log K from Indian radar (Rao et al., 2001) increase with height to about 75 km then decrease. The magnitude of log K is from 0 – 1.5 (K is from 1-31.6 m^2/s), larger than January's data. There is only one day of March data to compare

with the monthly medians of other two radars. Much smaller magnitude of *K* is also observed in JRO with a similar increase and decrease tendency as the Indian radar but with much smaller magnitude.

SNR for 5/23/03 (fig. 3.42) are much stronger than the previous day. The maxima are in the middle of the two layers. ε in these two layer go two extremes, the strongest values are in the middle around 20 mW/kg and the rest are very weak less than 6 mW/kg. Log *K* images keep only the structures with stronger ε.

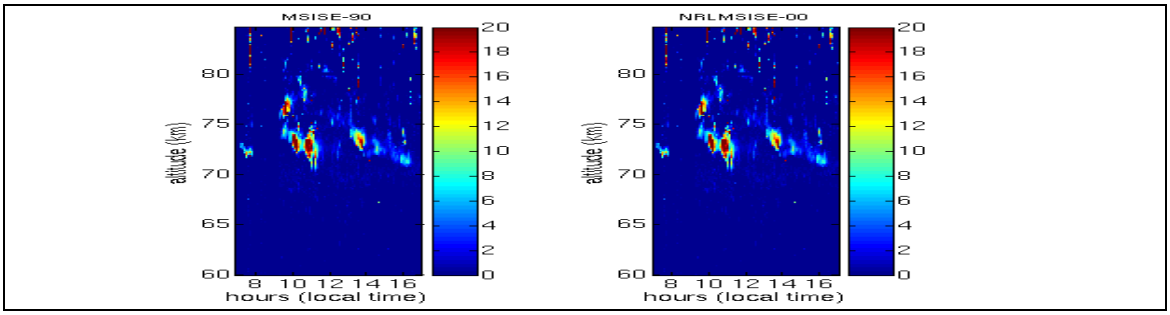

(a) ε (mW/kg) map for 5/23/03 (MSIS)

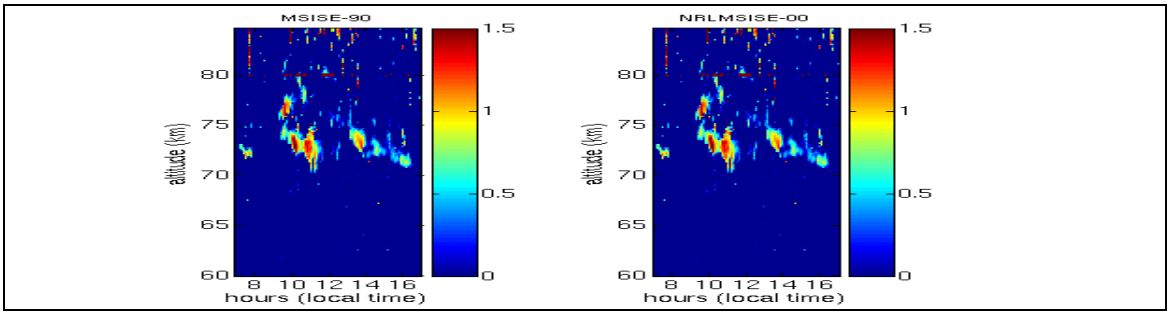

(b) Log *K* (m^2/s) map for 5/23/03 (MSIS)

Figure 3.42 Turbulent parameter maps for 5/23/03 (MSIS)

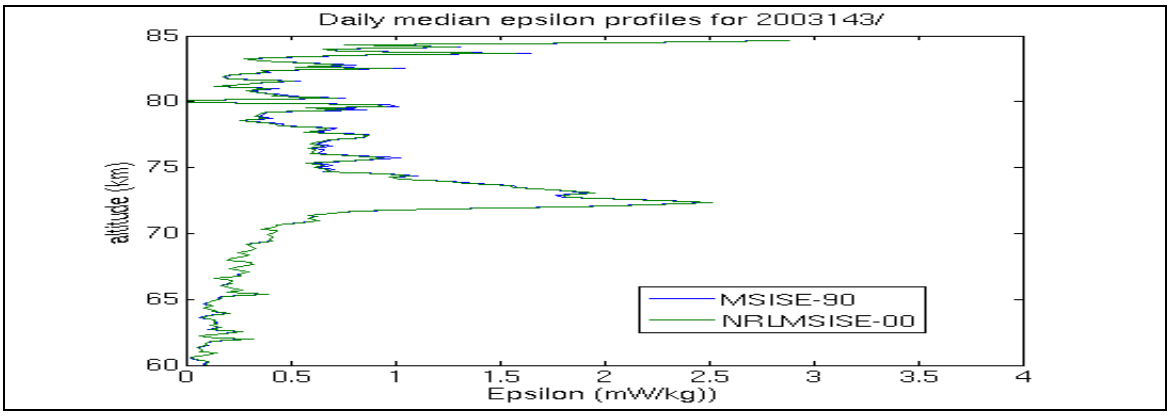

(a) ε (mW/kg) daily medians for 5/23/03 (MSIS)

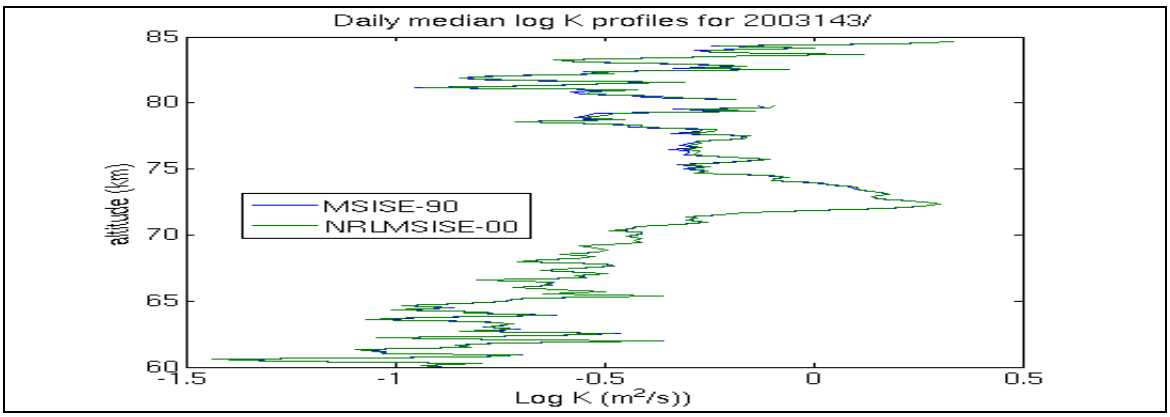

(b) Log K (m^2/s) daily medians for 5/23/03 (MSIS)

Figure 3.43 Turbulent parameter daily medians for 5/23/03 (MSIS)

The daily medians of ε (fig 3.43) increase with height and the maximum is at around 73 km then decrease above. Though the maximum ε values are larger for 5/23 than 5/22, the daily medians are on the contrary larger for 5/22. The maximum of 5/23 is about 2.5 mW/kg. Most of the data are less than 1 mW/kg. Log K are quite small for 5/23 the maximum is less than 0.5 and most of the data are less than 0.

ε and K are the strongest for 5/27/03 (fig 3.44). Large ε are everywhere during the whole day. The strongest turbulence are in the middle of the layer at 75 km and the 70 km layer hitting 30 mW/kg for ε and 2 for log K.

Even not considering the values above 80 km. The daily medians of ε (fig 3.45) are quite large, the maximum is about 30 mW/kg. Overall ε are increasing with height till about 75 km. Log K medians for 5/27 are also much larger than other days in May/03. The maxima are around 1.3-1.4.

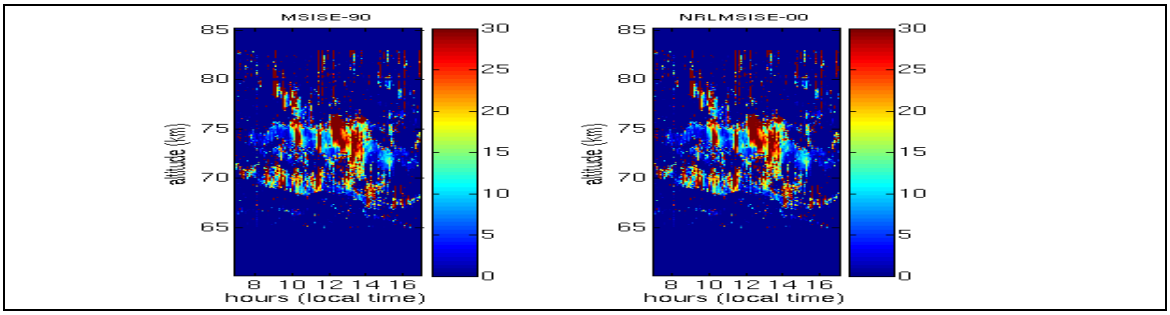

(a) ε (mW/kg) map for 5/27/03 (MSIS)

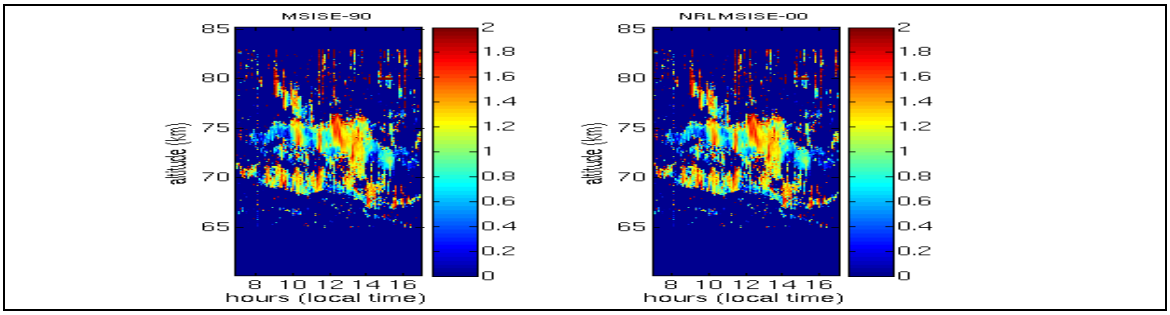

(b) Log K (m^2/s) map for 5/27/03 (MSIS)

Figure 3.44 Turbulent parameter maps for 5/27/03 (MSIS)

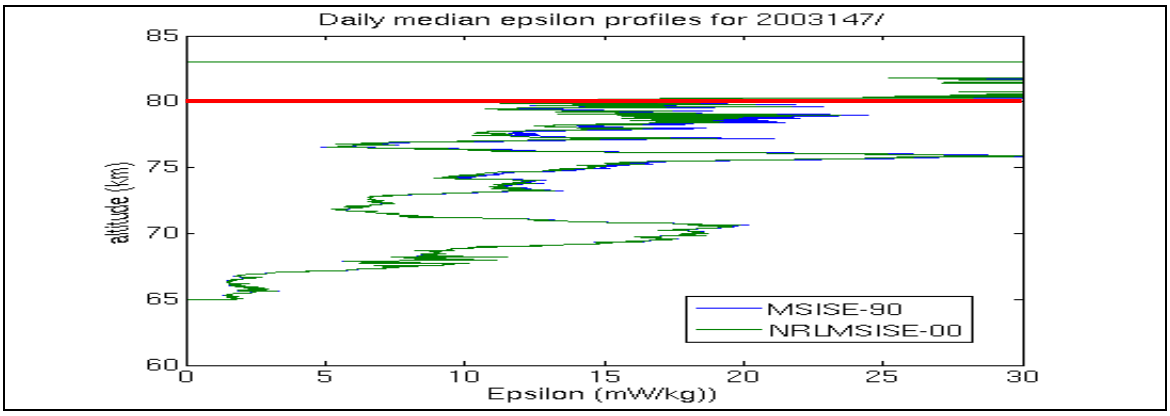

(a) ε (mW/kg) daily medians for 5/27/03 (MSIS)

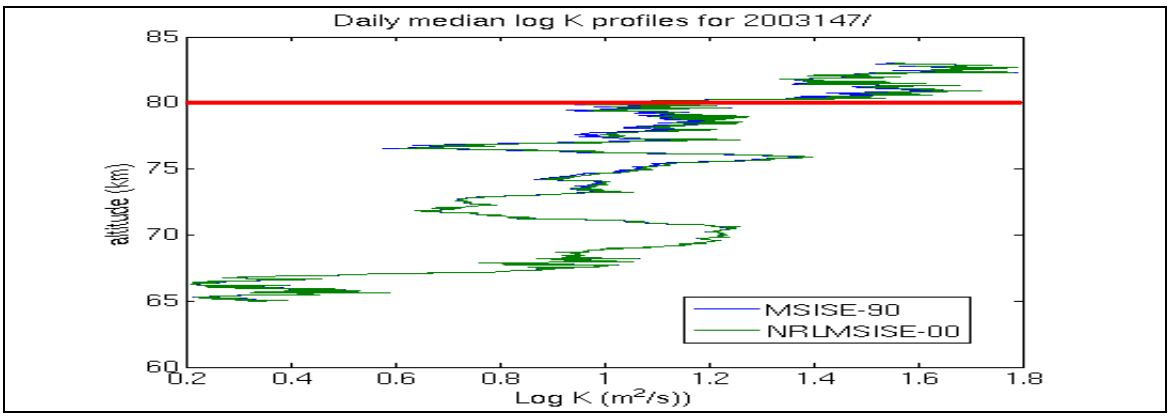

(b) Log K (m^2/s) daily medians for 5/27/03 (MSIS)

Figure 3.45 Turbulent parameter daily medians for 5/27/03 (MSIS)

ε and log K for 5/28/03 (fig 3.46) are larger in the lower layer, second half of the day and also larger in two blobs at just below 80 km. Though not over all as strong as 5/27, the maxima of ε also reach 30 mW/kg.

Since the echoes above 80 km are due to the spikes above, the daily medians of ε and log K (fig 3.47) above 80 km are not considered. The values below 65 km are not considered either, since

the echoes below 65 km have lots of large values, not real turbulence structures but dots of noises. The maxima of ε and log K occur at around 70 km. Values above or below 70 km are much smaller.

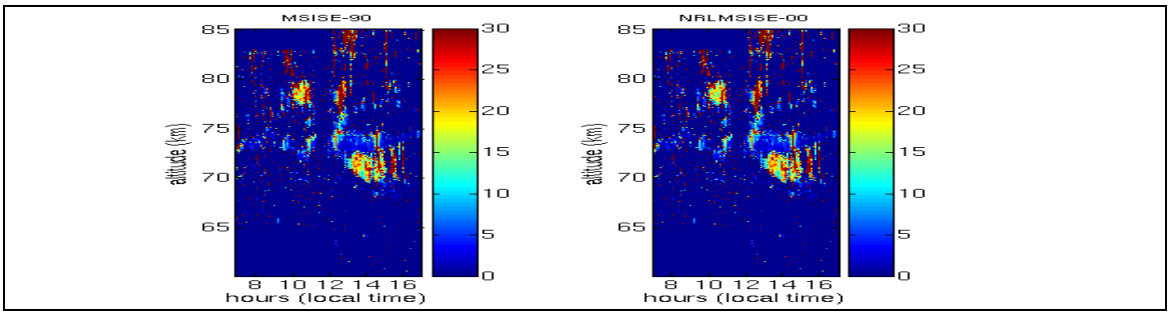

(a) ε (mW/kg) map for 5/28/03 (MSIS)

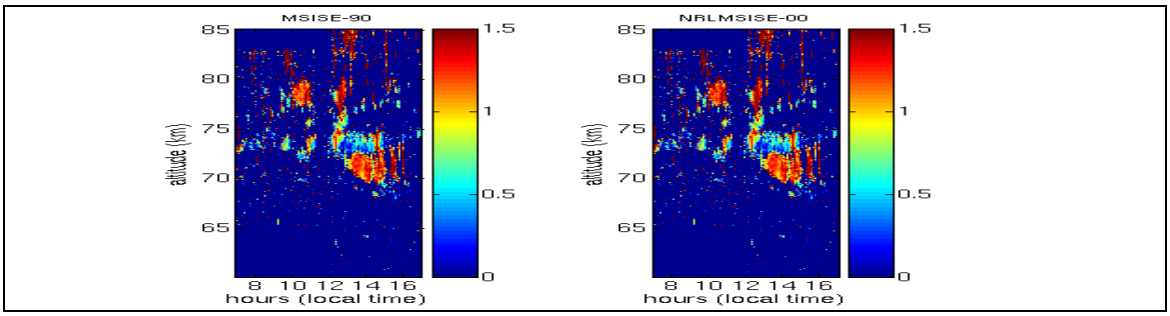

(b) Log K (m^2/s) map for 5/28/03 (MSIS)

Figure 3.46 Turbulent parameter maps for 5/28/03 (MSIS)

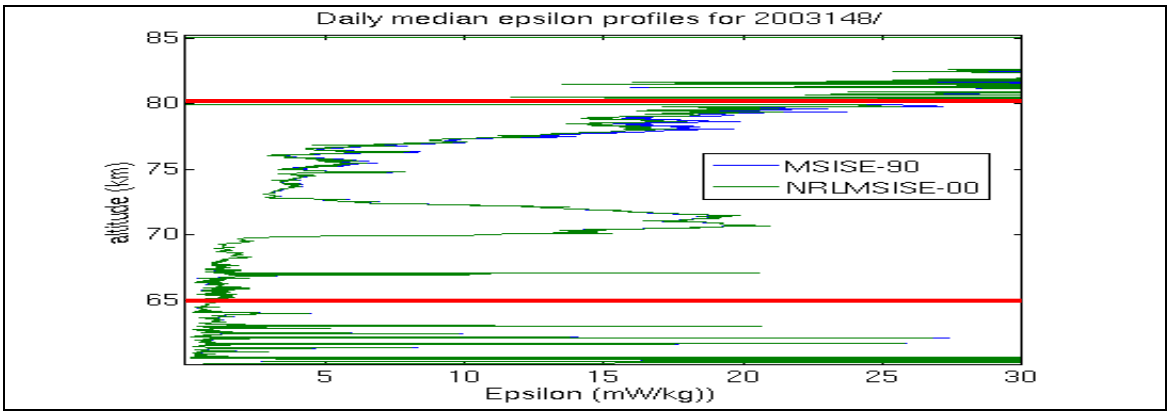

(a) ε (mW/kg) daily medians for 5/28/03 (MSIS)

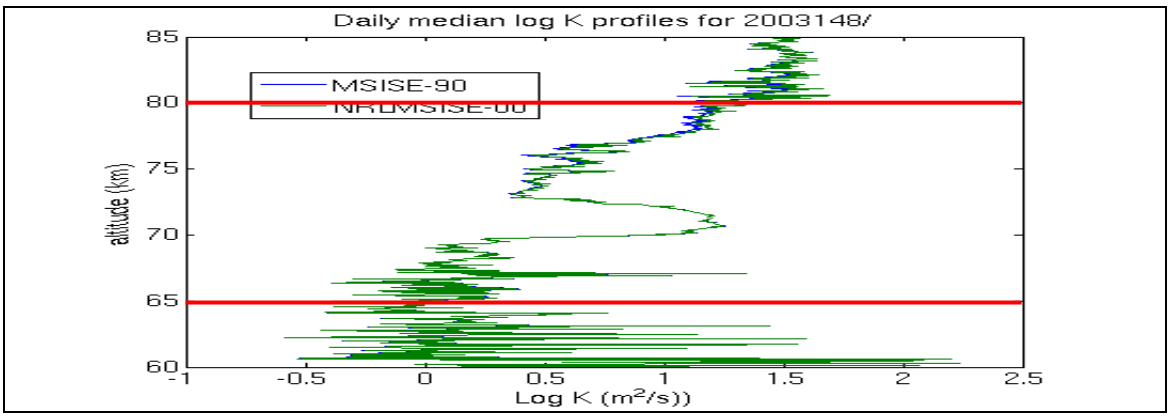

(b) Log K (m^2/s) daily medians for 5/28/03 (MSIS)

Figure 3.47 Turbulent parameter daily medians for 5/28/03 (MSIS)

ε and log K profiles (fig 3.48) for 5/28/03, 8:32 LT are shown below. 8:32 LT is the start of the day that no strong echoes are received. The values of ε and log K are not large: ε maxima are less than 7 mW/kg.

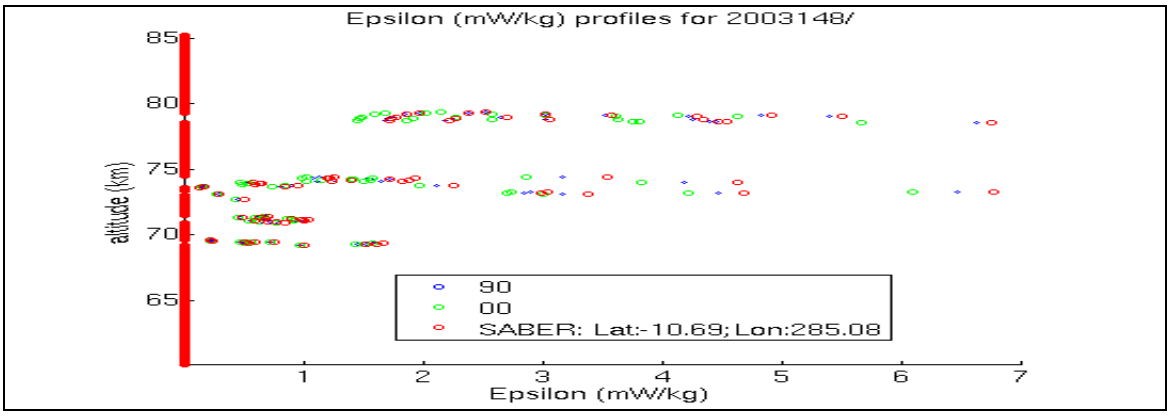

(a) ε (mW/kg) profiles

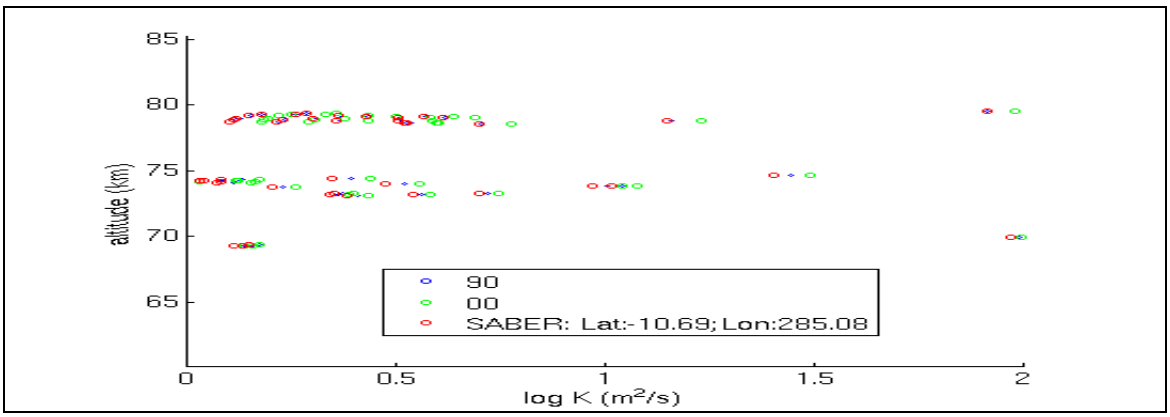

(b) Log K (m^2/s) profiles

Figure 3.48 Turbulent parameter profiles for 5/28/03, 8:32 LT (MSIS and SABER)

November monthly medians of K from MU radar (Fukao et al., 1994) are only available for 1988. They are about the same magnitude as January's data with maxima at around 77 km. The magnitude is from 1-10 m^2/s. November monthly medians of log K from Indian radar (Rao et al., 2001) increase with height to about 75-77 km then decrease. The magnitude of log K is from 0 – 0.9 (K is 1-8 m^2/s), also smaller than September's data but about the same as January's. JRO May log K

are in the range of 0-1.4 (1-25 m^2/s). The May monthly median of JRO is similar to MU radar with a similar increase and decrease tendency as the two radars.

The overall ε of JRO data are on the same order as the data from Rockets (Lübken, 1997), 1-10 mW/kg. In some days, there are bigger ε (up to 50 mW/kg) observed in strong turbulent layers.

3.4.2 Variation within layers

Several events have been studied for each observation. SNR, square of spectral widths due to turbulence, wind field, Richardson numbers and ε for each event are shown together for better comparison. Since the results calculated by using MSIS models are almost the same. Richardson number and ε images shown below are all calculated by using MSISE-90 temperatures

Two events from 7/20/02 are chosen:

(1) 13:26-14:38 LT, 68.71-73.62 km (fig 3.49): a descending structure with strongest SNR in east beam, the weakest in south beam. Though the SNR strengths are not extraordinarily strong, σ_{turb}^2 are quite large and ε very strong in this case. The zonal winds are all eastward. The meridional winds are almost all northward, a big difference with the previous two days.

(2) 15:27-16:10 LT, 73.06-75.13 km (fig 3.50): the strongest SNR of the day. There are two blobs with the strongest SNR not totally separate from each other in this structure. Both north and east beams have the strongest SNR. σ_{turb}^2 are also the biggest in these two beams. Zonal winds are much stronger in the eastward direction and meridional winds are much stronger in the northward direction than the first event. Almost all the Richardson numbers are less than 0.25. The strongest ε occur in the middle of the two blobs.

Among all these event in the three days of July/02 at different altitudes (70-75 km, 77-79 km), neither zonal nor meridional winds have changed direction vertically.

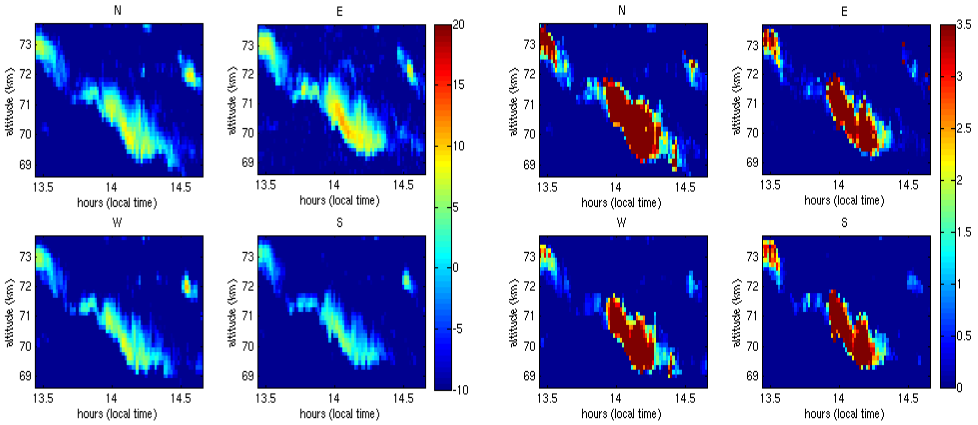

(a) SNR (b) σ_{turb}^2

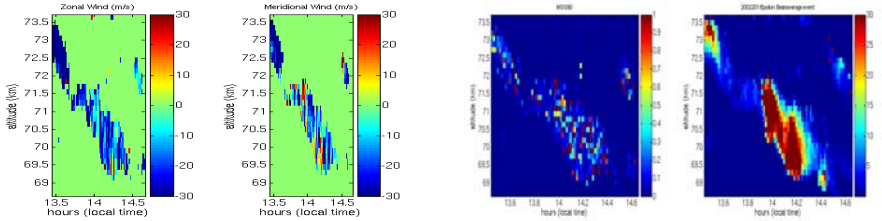

(c) Wind (d) Ri (e) ε

Figure 3.49 7/20/02, 13:26-14:38 LT, 68.71-73.62 km

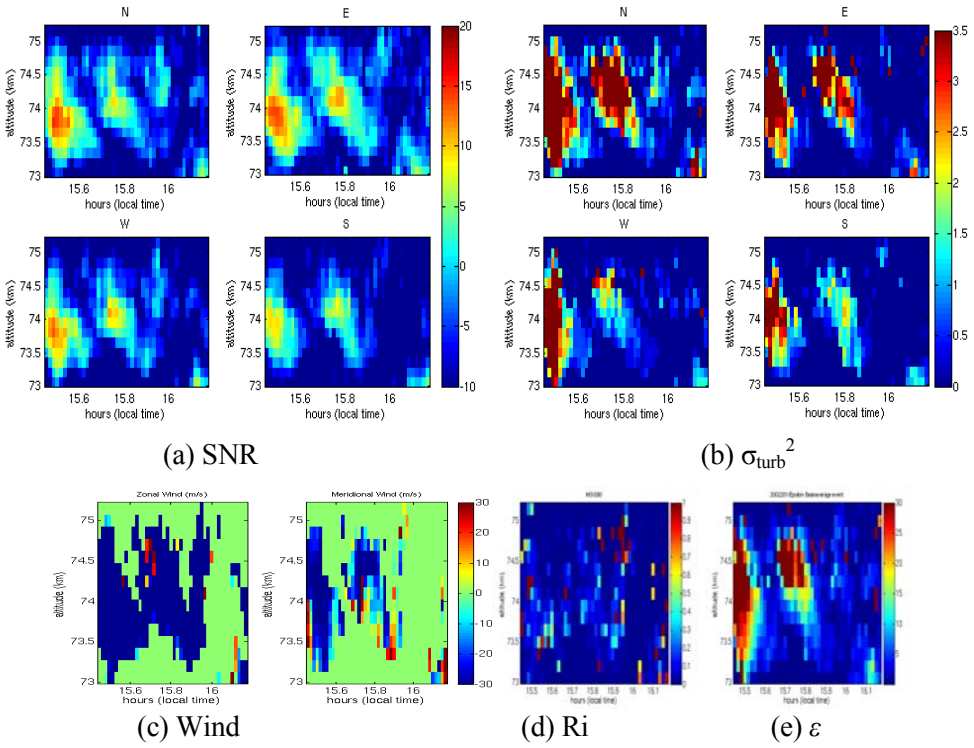

(a) SNR (b) σ_{turb}^2

(c) Wind (d) Ri (e) ε

Figure 3.50 7/20/02, 15:27-16:10 LT, 73.06-75.13 km

Two events from 3/5/03 are chosen:

(1) 14-16:29 LT, 74.19-76.08 km (fig 3.51): one of the strongest structures in 3/5. The south beam has a relatively stronger SNR, the rest of the beams have similar magnitude of SNR. σ_{turb}^2 are larger in the east and south beams. Zonal winds are mostly westward and meridional winds are southward at the lower edge and northward at the top edge. These are all different from the winds of July/02. ε are almost positively correlated with σ_{turb}^2. ε maxima are about 15 mW/kg.

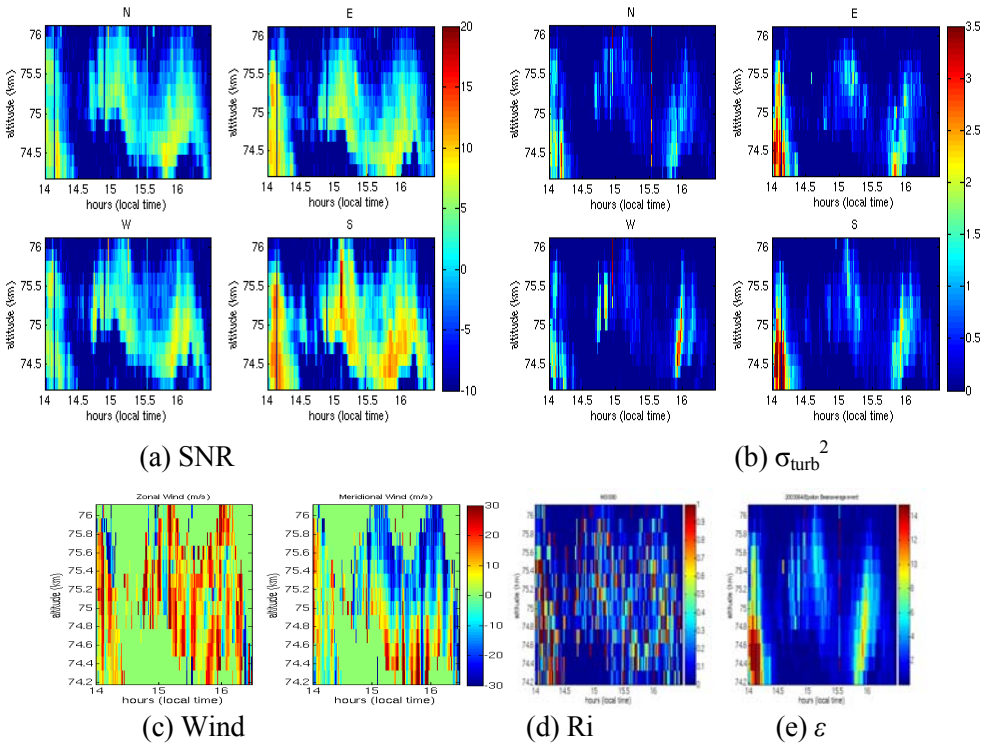

Figure 3.51 3/5/03, 14-16:29 LT, 74.19-76.08 km

(2) 9:12-10:48 LT, 74.16-76.46 km (fig 3.52): overall a little bit stronger SNR than the first case. σ_{turb}^2 are not larger than the first case and ε are about the same as the first case, the maxima are about 15 mW/kg. The zonal winds are stronger in westward direction. Meridional winds are similar with the first case with direction change vertically.

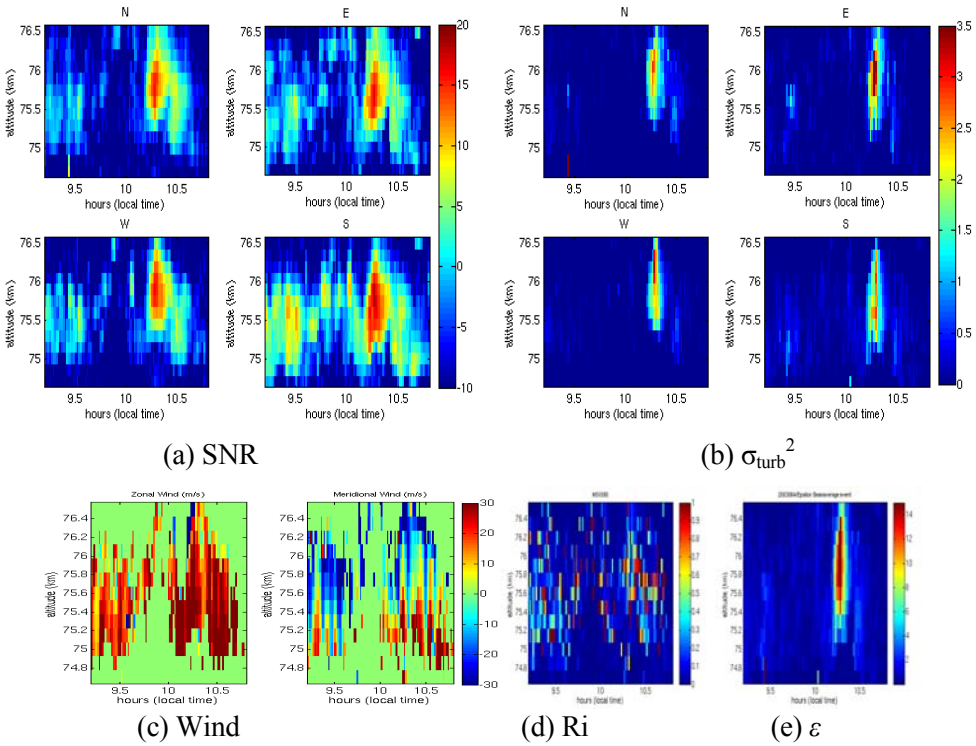

(a) SNR (b) σ_{turb}^2

(c) Wind (d) Ri (e) ε

Figure 3.52 3/5/03, 9:12-10:48 LT, 74.16-76.46 km

Two events from 5/23/03 are chosen:

(1) 9:35-11:02 LT, 71.54-74.57 km (fig 3.53): one of the strongest SNR for the day. South beam has bit stronger SNR. The strongest SNR are all in the middle of the descending layer with the same descending shape. σ_{turb}^2 are very large for this event, though the largest σ_{turb}^2 are in the middle of the layer, they are not in the same descending shape. The largest σ_{turb}^2 are 2 blobs in the middle not coinciding with the strongest SNR. Both zonal and meridional winds have changed direction vertically. ε in this case are very strong reaching 30 mW/kg. ε do not have the exactly same pattern as σ_{turb}^2.

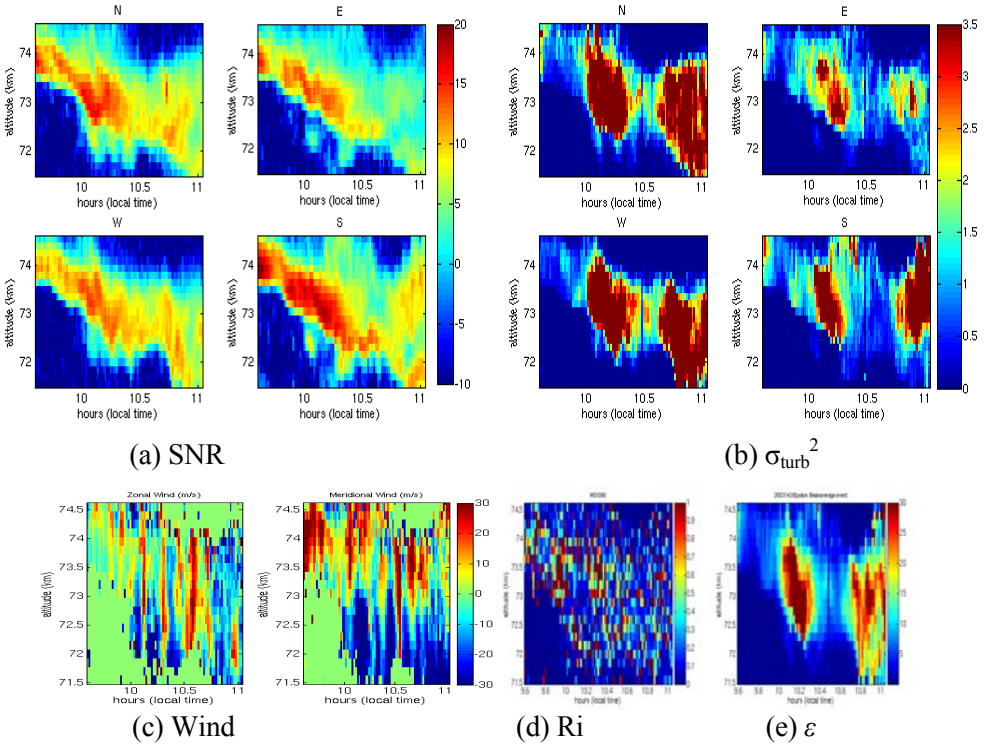

Figure 3.53 5/23/03, 9:35-11:02 LT, 71.54-74.57 km

(2) 13:07-15:08 LT, 71.54-75.32 km (fig 3.54): this event happens later than the first one at about the same altitude. SNR are not as strong as the first case. So are zonal winds, σ_{turb}^2 and ε. Meridional winds are about the same as the first case.

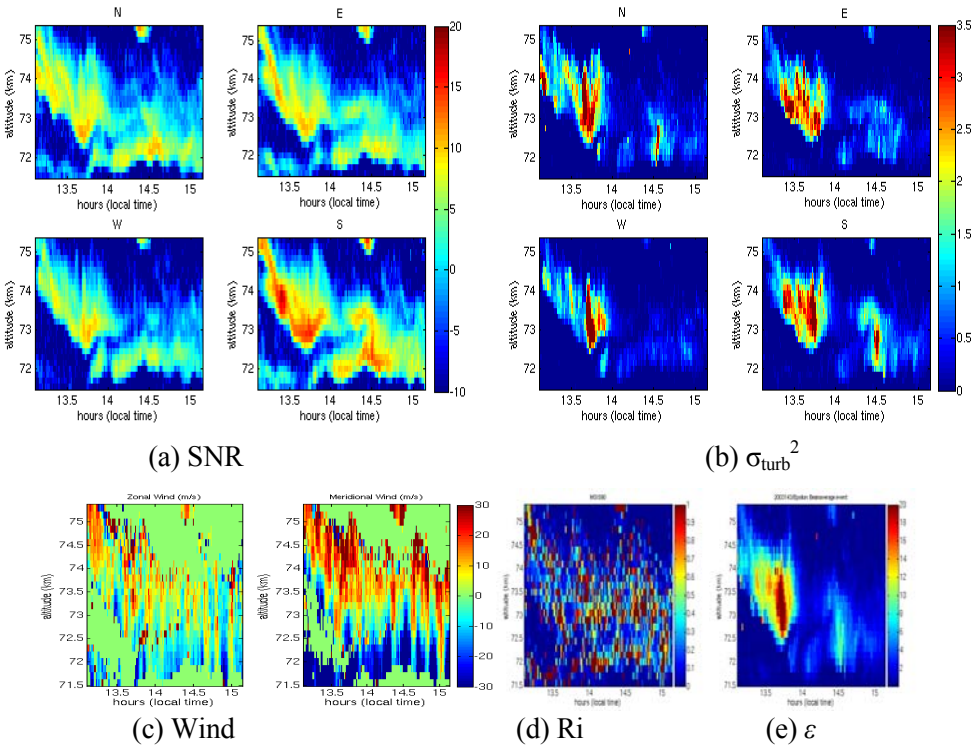

Figure 3.54 5/23/03, 13:07-15:08 LT, 71.54-75.32 km

Three events from 5/27/03 are chosen, all the Richardson numbers are very small:

(1) 8:57-10 LT, 76.84-80.48 km (fig 3.55): the highest activities on this day. Compared to other days, SNR are not particularly large for this case, but σ_{turb}^2 and ε are all very large for this event. ε maxima are about 40 mW/kg. Zonal winds are not strong in the eastward direction. At the top of the lower blob, there is changing direction with height. Meridional winds are mostly northward, no change of direction at this altitude.

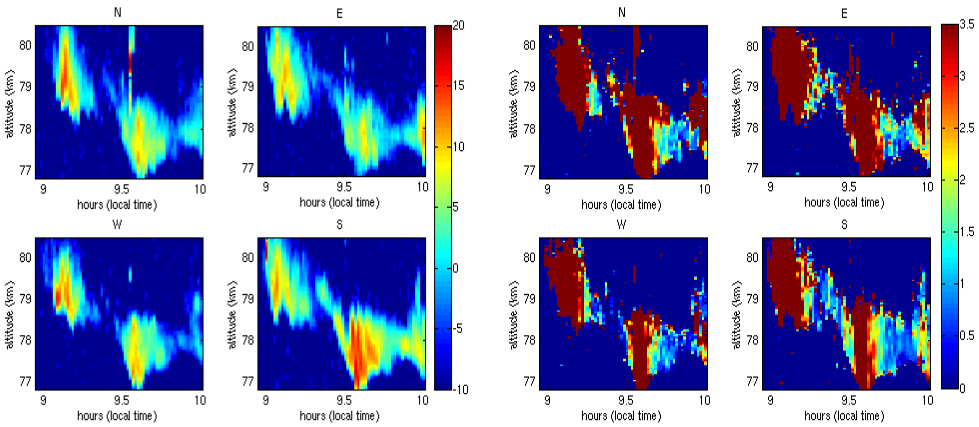

(a) SNR (b) σ_{turb}^2

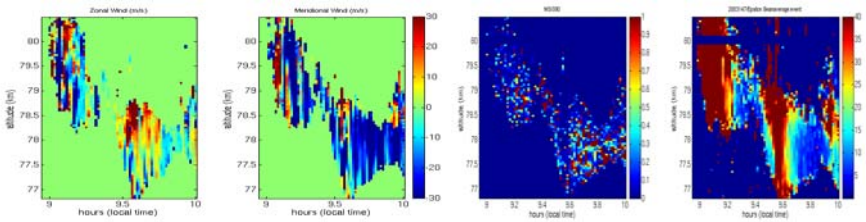

(c) Wind (d) Ri (e) ε

Figure 3.55 5/27/03, 8:57-10 LT, 76.84-80.48 km

(2) 12:05-14:14 LT, 71.8-76.65 km (fig 3.56): the strongest SNR of the day (upper layer) and also the largest σ_{turb}^2 in all the beams. Zonal winds are mostly eastward except one spot at 73 km, 12:30 LT. The top edge of positive winds are false information due to the double-peak spectra. There is obvious meridional wind direction change at this altitude. ε are very large in this case reaching 40 mW/kg in the middle of the layer.

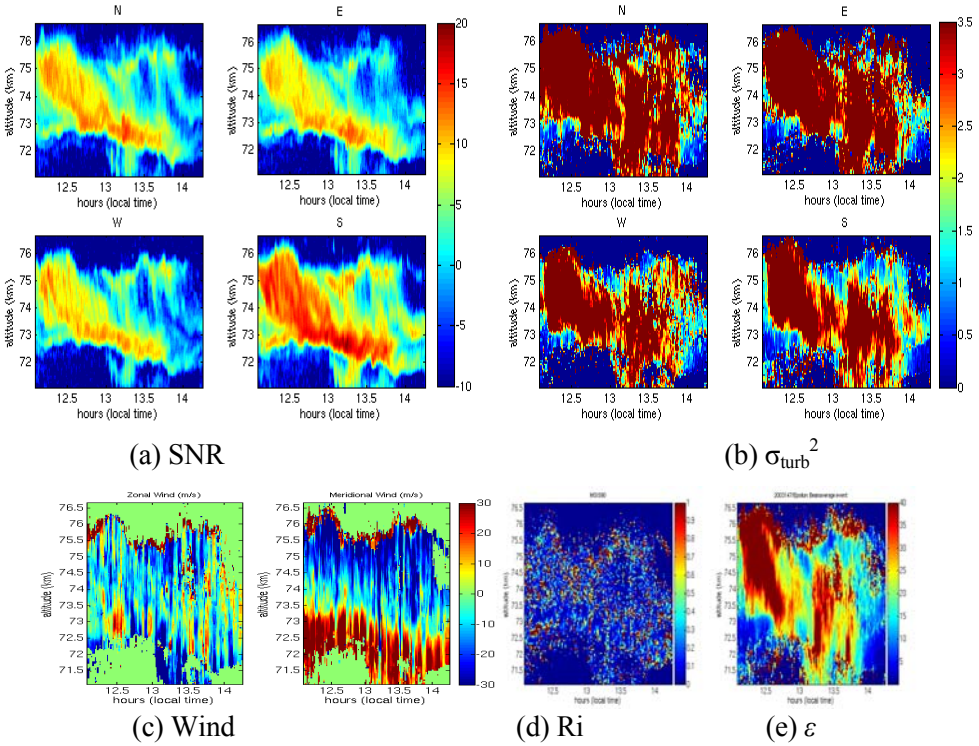

Figure 3.56 5/27/03, 12:05-14:14 LT, 71.8-76.65 km

(3) 13:35-13:57 LT, 67.1-68.8 km (fig 3.57): a part from the lower and much thinner layer. Although the strongest SNR are about the same magnitude of the previous case, σ_{turb}^2 are quite small in this case. ε are much weaker than the higher cases. There is no change of direction in winds at this altitude.

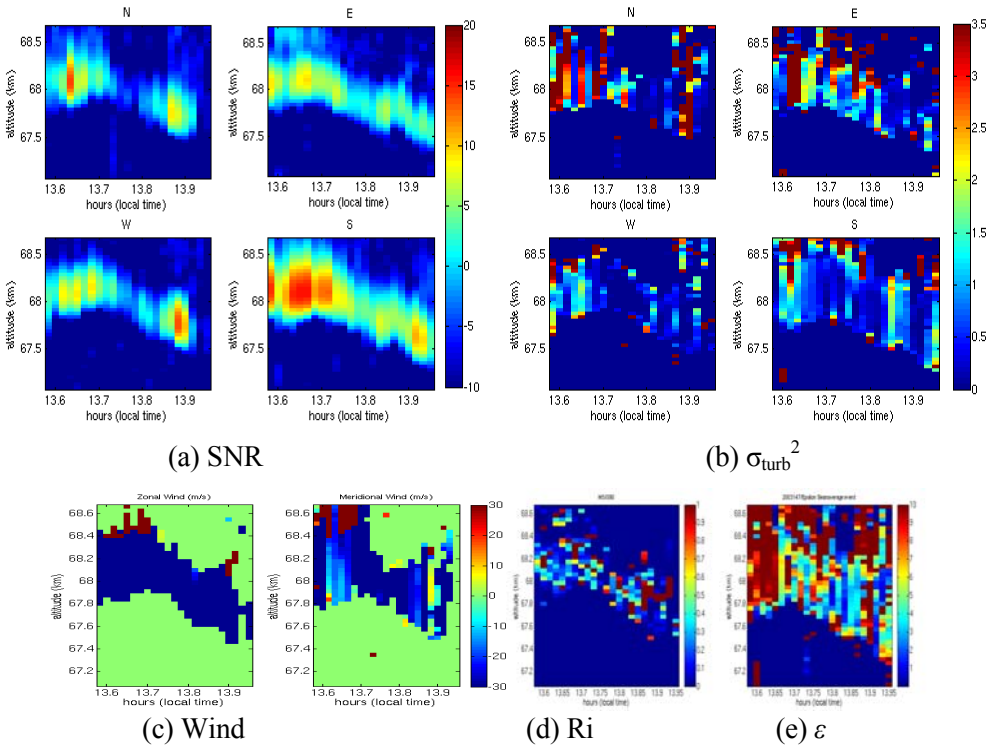

Figure 3.57 5/27/03, 13:35-13:57 LT, 67.1-68.8 km

Three events from 5/28/03 are chosen:

(1) 12:05-14:48 LT, 72.3-74.03 km (fig 3.58): part of the long layer with strong echoes. The strongest SNR are in the first part of this event, around 12:30 LT. σ_{turb}^2 are mostly positively correlated with SNR. Zonal winds are not strong but with eastward wind at the edges and westward wind in the center. Meridional winds change from southward below to northward upper like some other cases in this altitude. Richardson numbers are small in the center and larger at the edges. ε are quite large for this case, mostly positively correlated with σ_{turb}^2, maxima reaching 40 mW/kg at the end of the event.

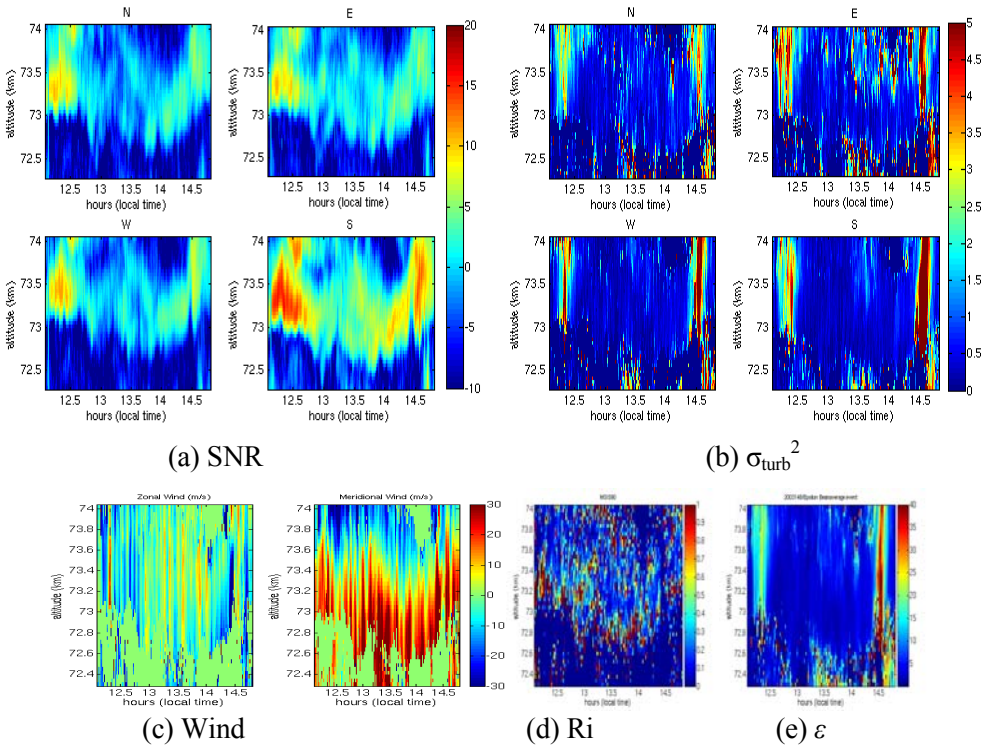

Figure 3.58 5/28/03, 12:05-14:48 LT, 72.3-74.03 km

(2) 10:14-10:53 LT, 76.94-79.46 km (fig 3.59): a blob in the upper part of the image. Compare to the previous event, SNR of this event are not overall strong; while σ_{turb}^2 are much stronger than the previous case. At the same time winds are stronger. Zonal winds are dominated by eastward winds. Meridional winds change direction vertically. Richardson numbers are all quite small. ε are stronger than the previous case, even though SNR are not stronger.

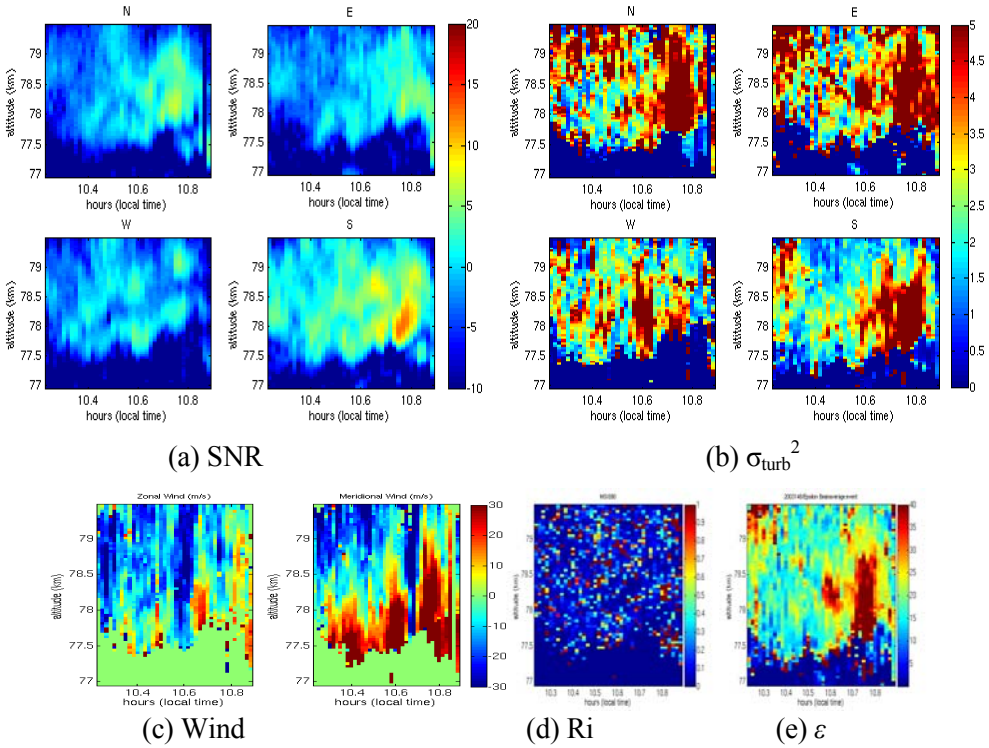

Figure 3.59 5/28/03, 10:14-10:53 LT, 76.94-79.46 km

(3) 13:12-14:24 LT, 69.39-72.1 km (fig 3.60): a part of the layer at a lower altitude just below the main layer. Compare to the previous two events, SNR of this event are weaker. But σ_{turb}^2 still remain large. Winds are not as strong as the second case. Mostly eastward zonal winds dominate and meridional winds are dominated by southward winds. There are no meridional wind shears found in this lower altitude case. Richardson numbers are all about the same as the previous case. ε are weaker than the previous case.

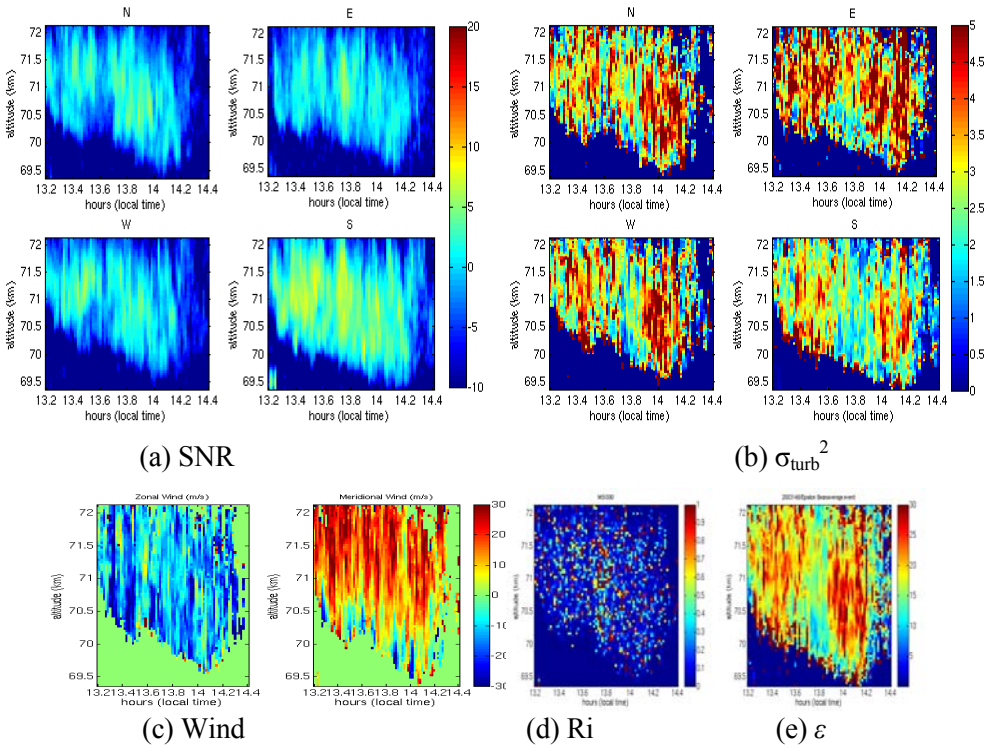

(a) SNR (b) σ_{turb}^2

(c) Wind (d) Ri (e) ε

Figure 3.60 5/28/03, 13:12-14:24 LT, 69.39-72.1 km

3.5 Correlation Coefficients

The vertical profiles for correlation coefficients of σ_{turb}^2 (each beam) and the wind shears, ε and SNR (each beam) for each day are calculated (section 3.5.1). The correlation coefficients for these values in some strong SNR event (section 3.5.2) are also calculated. The wind shears have been smoothed into curves for every minute avoiding the unrealistic sudden changes over adjacent altitude.

3.5.1 Daily profiles of correlation coefficients

σ_{turb}^2 (each beam) and the wind shear (fig 3.61) do not show clear correlations no matter for wider days or narrower days.

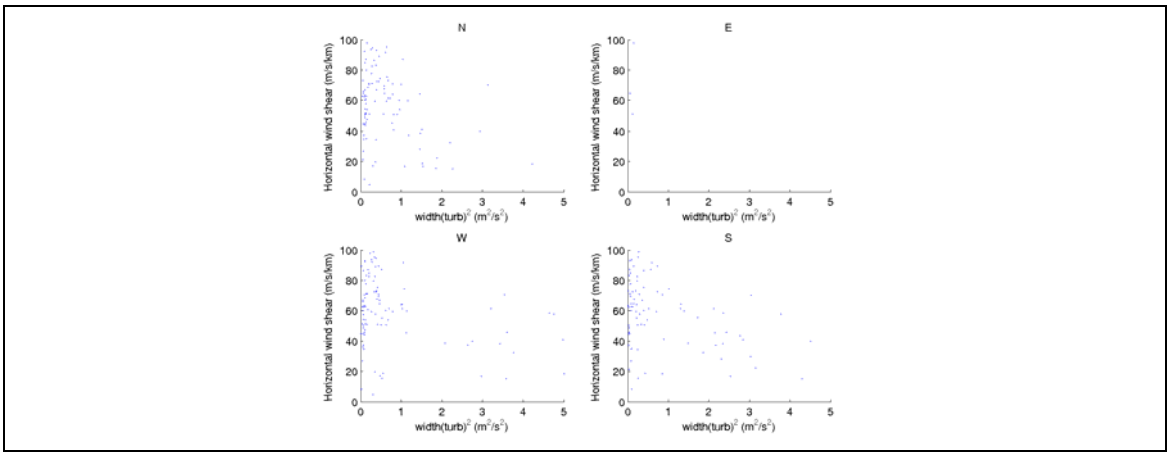

7/20/02

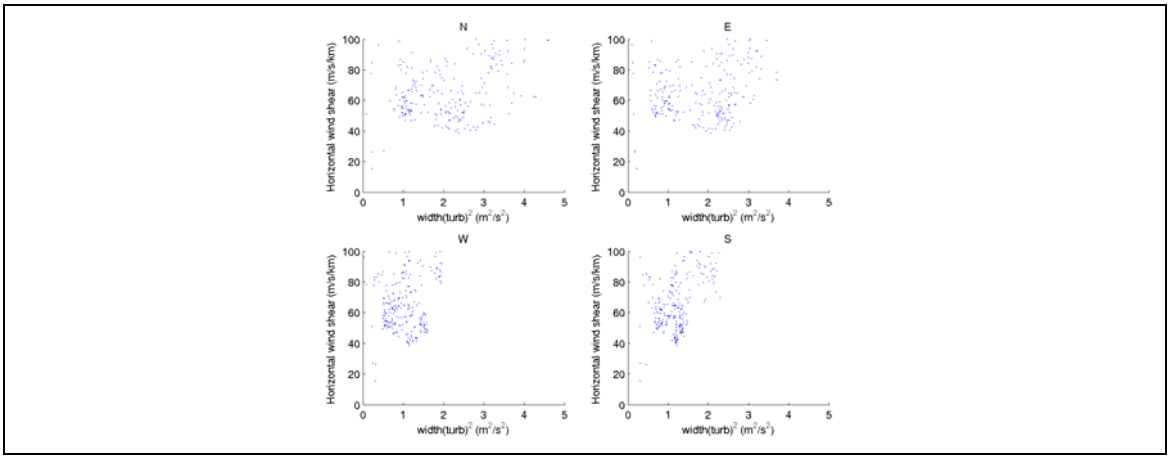

5/27/03

Figure 3.61 The scatter plots of σ_{turb}^2 (each beam) vs wind shear

The correlation coefficients of ε and SNR (fig 3.62) on 7/18/02 are mostly positive. The change with height is related to the intensity of SNR, the larger the SNR at this level, the larger the correlation between ε and SNR. The maxima of the correlation coefficients are about 0.7-0.75.

The variations among different days are not correlated with the strength of SNR of that day. Though SNR in 5/23/03 (fig 3.64) is much stronger than those of 7/18/02 (fig 3.62), the correlation coefficients are not larger. They are about the same magnitude.

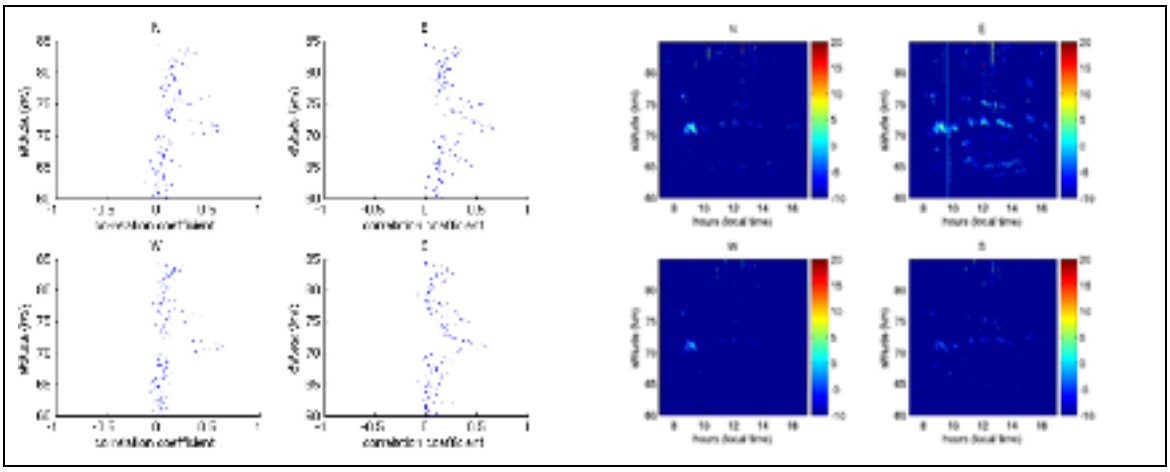

Figure 3.62 Correlation coefficient profile of ε and SNR compared with SNR images (7/18/02)

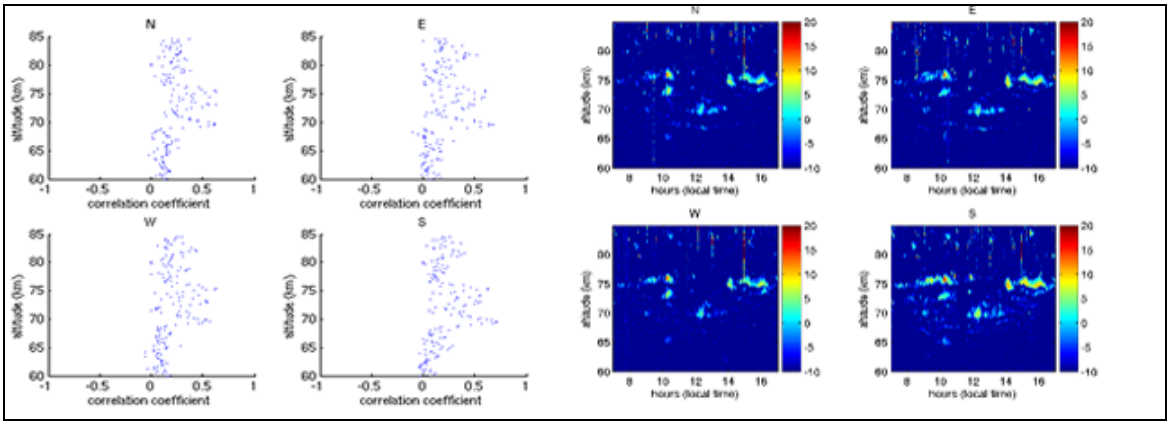

Figure 3.63 Correlation coefficient profile of ε and SNR compared with SNR images (3/5/03)

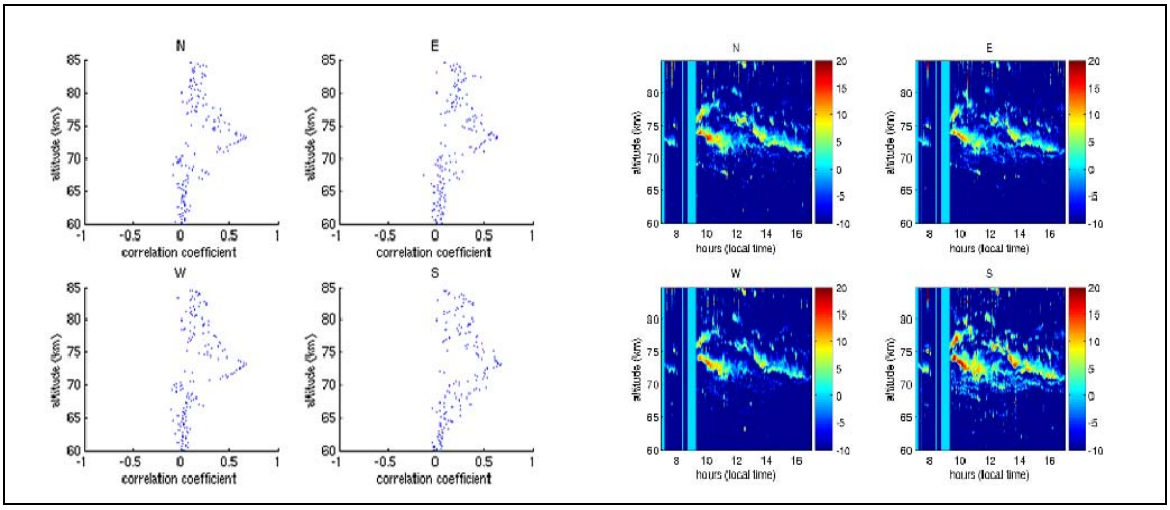

Figure 3.64 Correlation coefficient profile of ε and SNR compared with SNR images (5/23/03)

3.5.2 The correlation coefficients of some events

The same correlation coefficients for some chosen events are calculated and compared. These events are about the same as the ones chosen in the section 3.4.2.

7/20/02 (fig 3.65 and 3.66), the two events selected (similar to Fig 3.49 and Fig. 3.50) all have positive correlations between SNR and ε as well as wind shear and σ_{turb}^2. The correlation between SNR and ε are larger, mostly ~ 0.75. The correlation between wind shear and σ_{turb}^2 though positive but with small correlation coefficients (not shown).

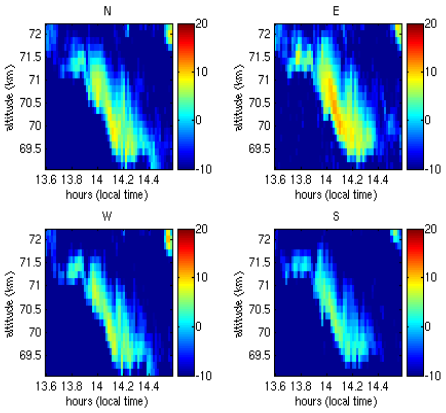

(a) SNR

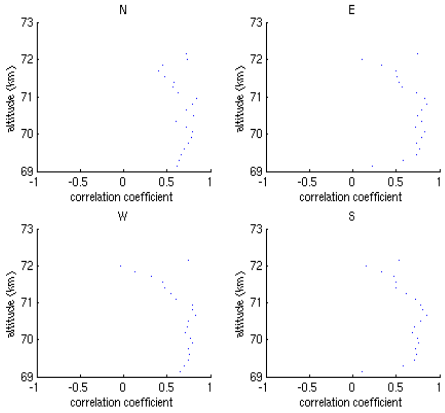

(b) correlation coefficients of ε and SNR

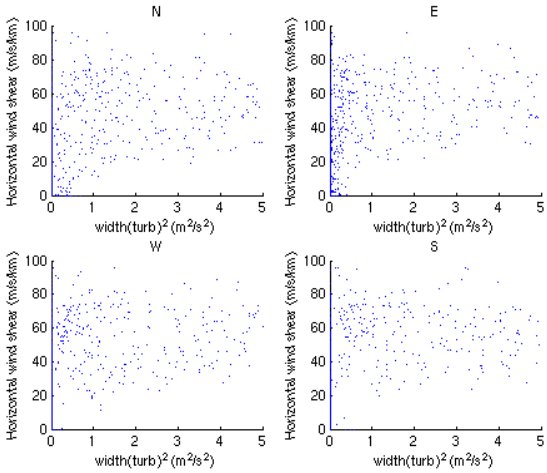

(c) scatter plots of wind shear vs. σ_{turb}^2

Figure 3.65 7/20/02, 13:36-14:34 LT, 69.08-72.11 km

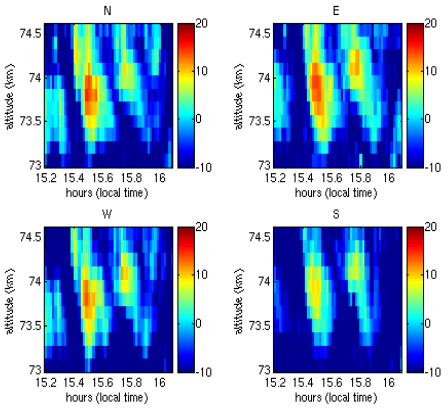

(a) SNR

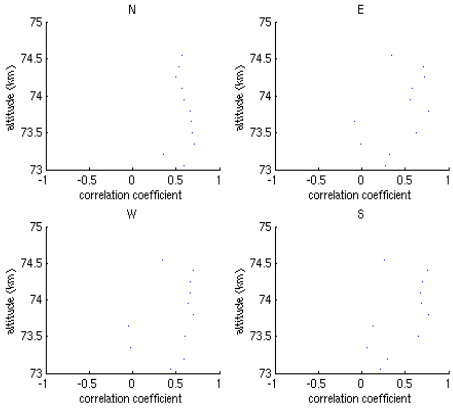

(b) correlation coefficients of ε and SNR

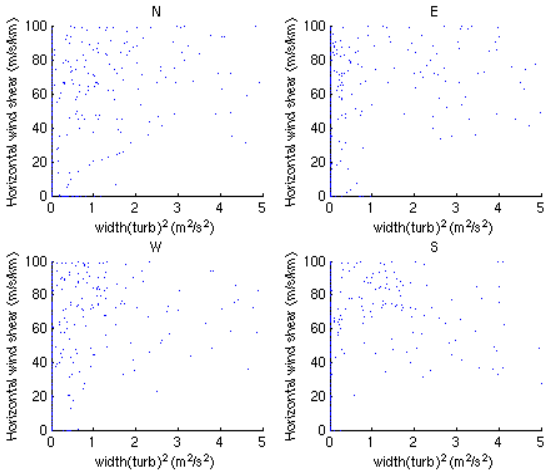

(c) scatter plots of wind shear vs. σ_{turb}^2

Figure 3.66 7/20/02, 15:12-16:05 LT, 73.06-74.57 km

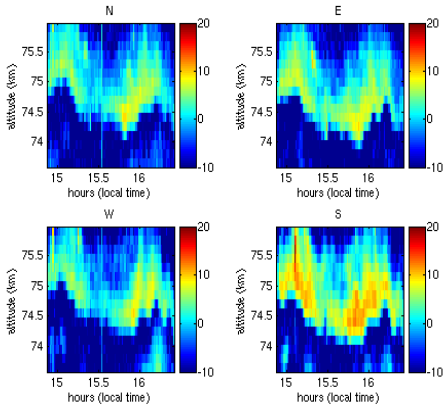

(a) SNR

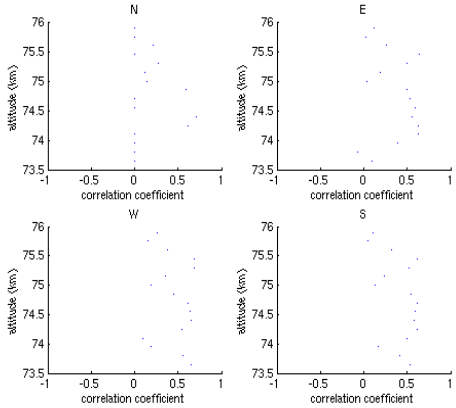

(b) correlation coefficients of ε and SNR

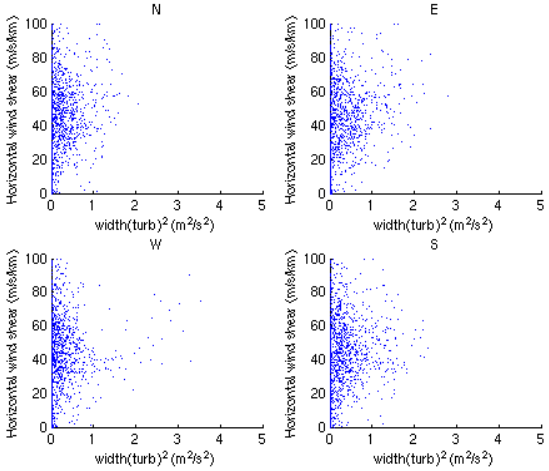

(c) scatter plots of wind shear vs. σ_{turb}^2

Figure 3.67 3/5/03, 14:53-16:25 LT, 73.62-75.89 km

3/5/03 (fig 3.67), the one event selected (similar to Fig. 3.51) have positive correlations between SNR and ε as well as wind shear and σ_{turb}^2. The correlation between SNR and ε are not as large as 7/20/02. The scatter plots of wind shear vs. σ_{turb}^2 are quite different from the ones of

7/20/02 because 3/5/03 has much narrower widths. The over all correlation coefficients are not improved (not shown).

5/27/03 (fig 3.68), the one event shown here (similar to Fig. 3.55) have positive correlations between SNR and ε as well as wind shear and σ_{turb}^2. The correlation coefficients between SNR and ε are mostly larger than 0.5. The correlation between wind shear and σ_{turb}^2 are quite small.

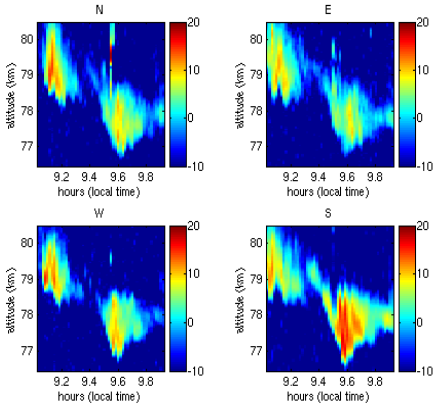

(a) SNR

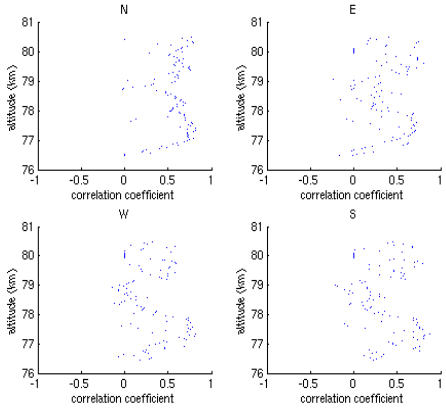

(b) correlation coefficients of ε and SNR

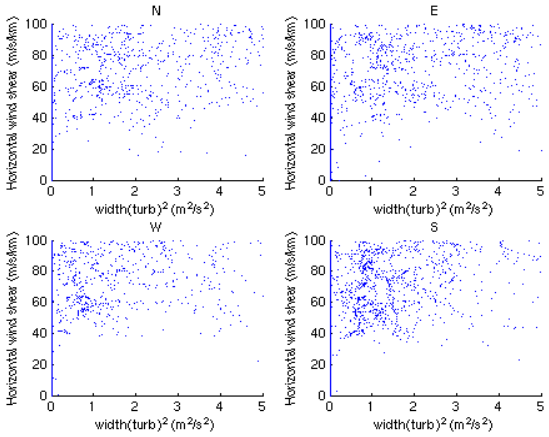

(c) scatter plots of wind shear vs. σ_{turb}^2

Figure 3.68 5/27/03, 9:02-9:55 LT, 76.45-80.48 km

CHAPTER 4

CONCLUSIONS

We analyzed Jicamarca mesospheric data for July 2002, March and May, 2003. From the spectral widths of the radar signals, turbulent energy dissipation rates ε and eddy diffusivities K were derived. The correlation relationship of horizontal wind shears and spectral widths as well as SNR and ε are also studied. We present our conclusions and summarize our results in the following paragraphs.

Meridional winds exhibit a change of direction between 74-77 km in March and May, 2003. Sometimes wind shears occur even at lower altitudes, 71 or 72 km. Below 71 km, wind shears in meridional winds are rarely seen due to lack of strong echoes. There were no meridional wind shears observed in July/02. The chance for zonal winds to change direction is much less compared to meridional winds in most cases. This suggests meridional winds contain more tidal modulations than zonal winds.

Different temperature data sets obtained from models and satellite were used to calculate ε and K, but the difference between the results was not significant. This indicates that the spectral widths have a much larger effect on the turbulent parameters. The reason for this may be that there is much smaller daily variation in the Brunt-Vaisala frequency (0.015-0.025 /s) than in the variance (square of the spectral widths) of the wind fluctuations (0-7 m^2/s^2).

Some large values of ε, about 50 mW/kg can be found in the middle of turbulent structures. Daily medians of ε were calculated for each altitude and range from about 1-10 mW/kg. They usually increase with height up to about 75-77 km, then decrease slightly above.

The values of K are mostly less than 35 m^2/s but occasionally can reach more than 100 m^2/s. For some quiet days, they can be less than 5 m^2/s. The altitude profile of K exhibits the similar behavior of ε.

The values for ε and K in July/02 and March/03 were the smallest; in May/03 we observed the largest values.

For July, 2002 and May 2003 we form monthly medians of K and compared them with the MU radar (Fukao et al., 1994) and the Indian radar (Rao et al., 2001) results.

For July, both radars show small values for K as found from JRO data (1-5 m^2/s). The July profile of the Indian radar behaves similarly as JRO data.

For May, our data are in the range of 1-25 m^2/s, in the same order of magnitude as the MU radar data. The magnitude of K from the Indian radar data is smaller (~ 5 m^2/s). All three radars have maxima at around 75-77 km.

The overall values for ε from JRO data are on the same order as data from the rockets (1-10 mW/kg) obtained in polar winter (Lübken, 1997). On some days, we observed large ε (up to 50 mW/kg) in strong turbulent layers.

The similar values from radars and rockets is an indication that both techniques can yield valid estimates for ε. However, values of ε vary strongly in time and space and detailed comparisons are difficult (Royrvik and Smith, 1984). Furthermore, the formulas we used to estimate ε and K based on a lot of assumptions, which may contribute uncertainties in the results.

The correlation coefficients between σ_{turb}^2 and the wind shear are mostly positive but small (0.2-0.3). This may indicate other processes besides wind shear may contribute to turbulence.

The correlation between SNR and ε is mostly positive with correlation coefficients up to 0.75. The positive correlation between SNR and ε gives us confirmation that the scatterers are

distributed by isotropic turbulence. The correlation coefficients for stronger SNR days have similar values for weaker SNR days.

Comparing the correlation coefficients from different layers in the same day, there is no direct relationship between height and the coefficients. There is also no indication that layers with stronger SNR have larger ε than layers with weaker SNR. This suggests that SNR values are not good indicators of turbulence strength.

APPENDIX A SNR IMAGES

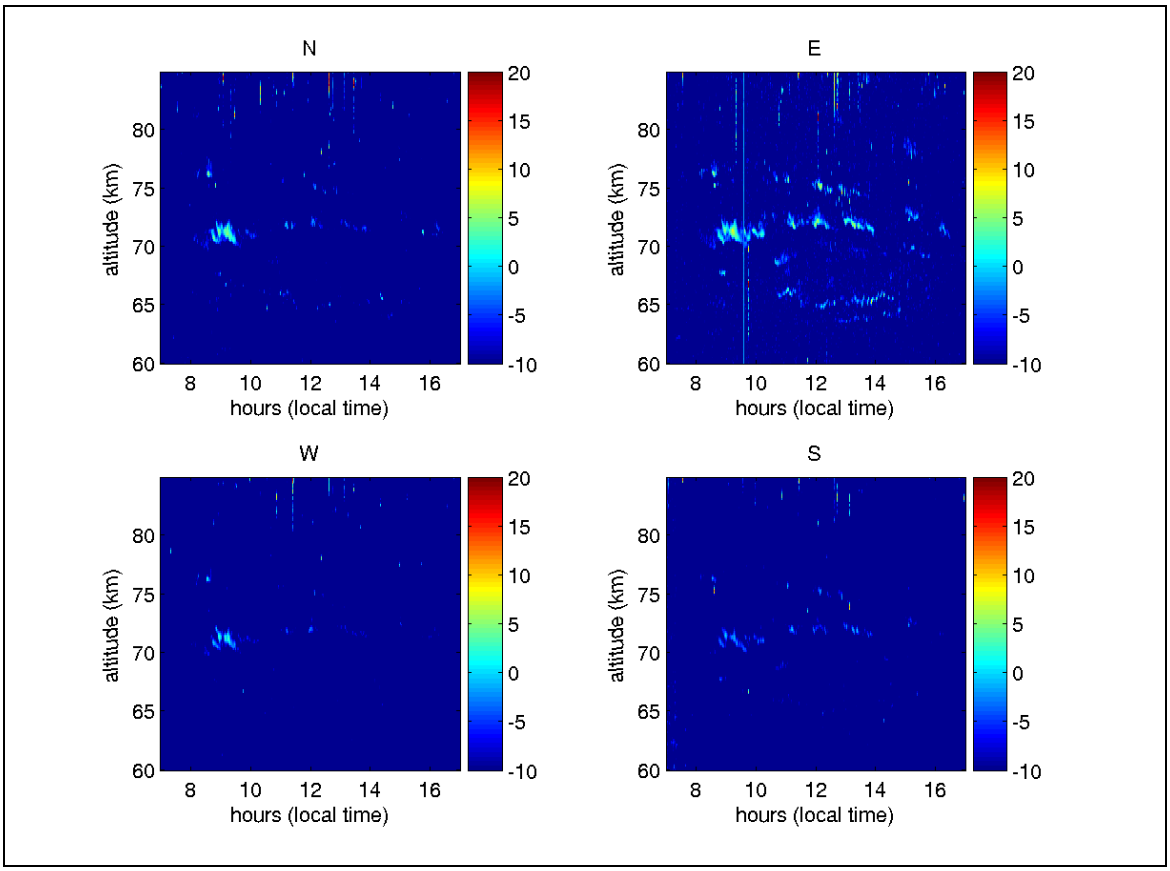

Figure A.1 SNR maps from 7/18/02 for the north, east, west and south beam

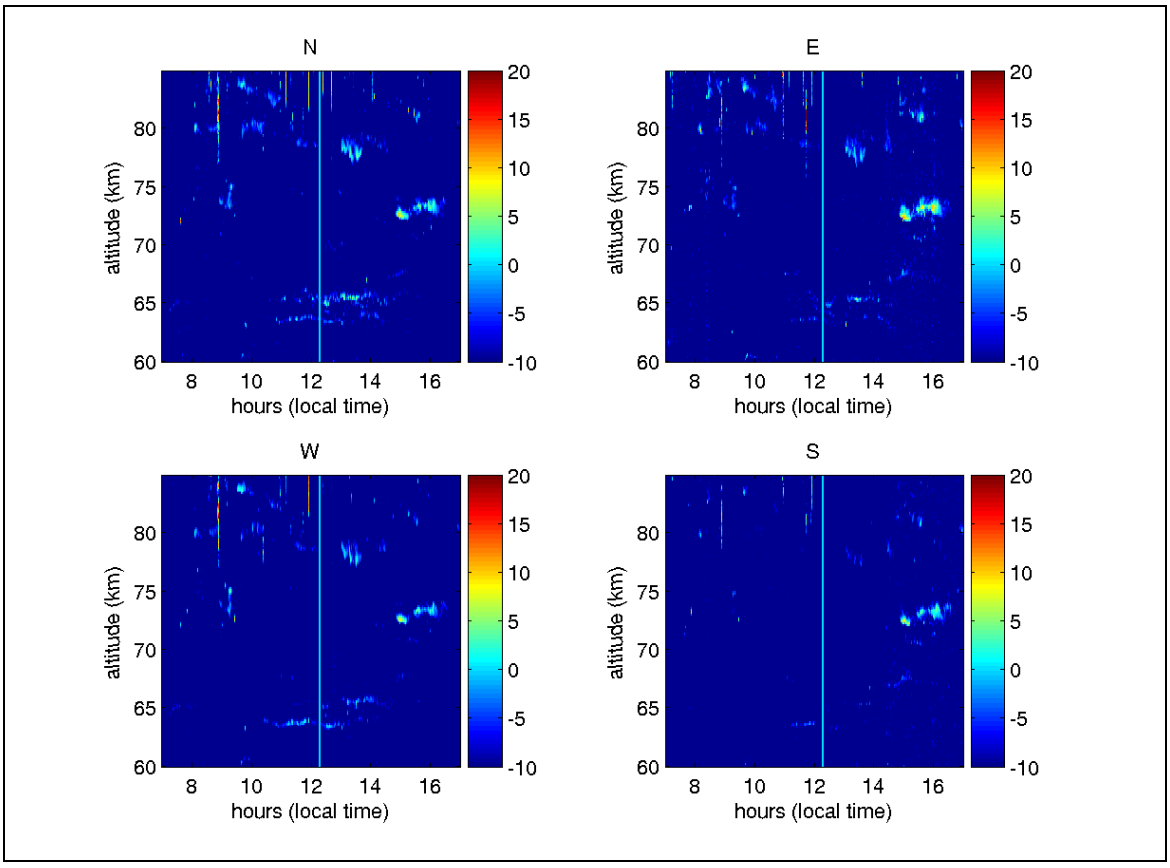

Figure A.2 SNR maps from 7/19/02 for the north, east, west and south beam

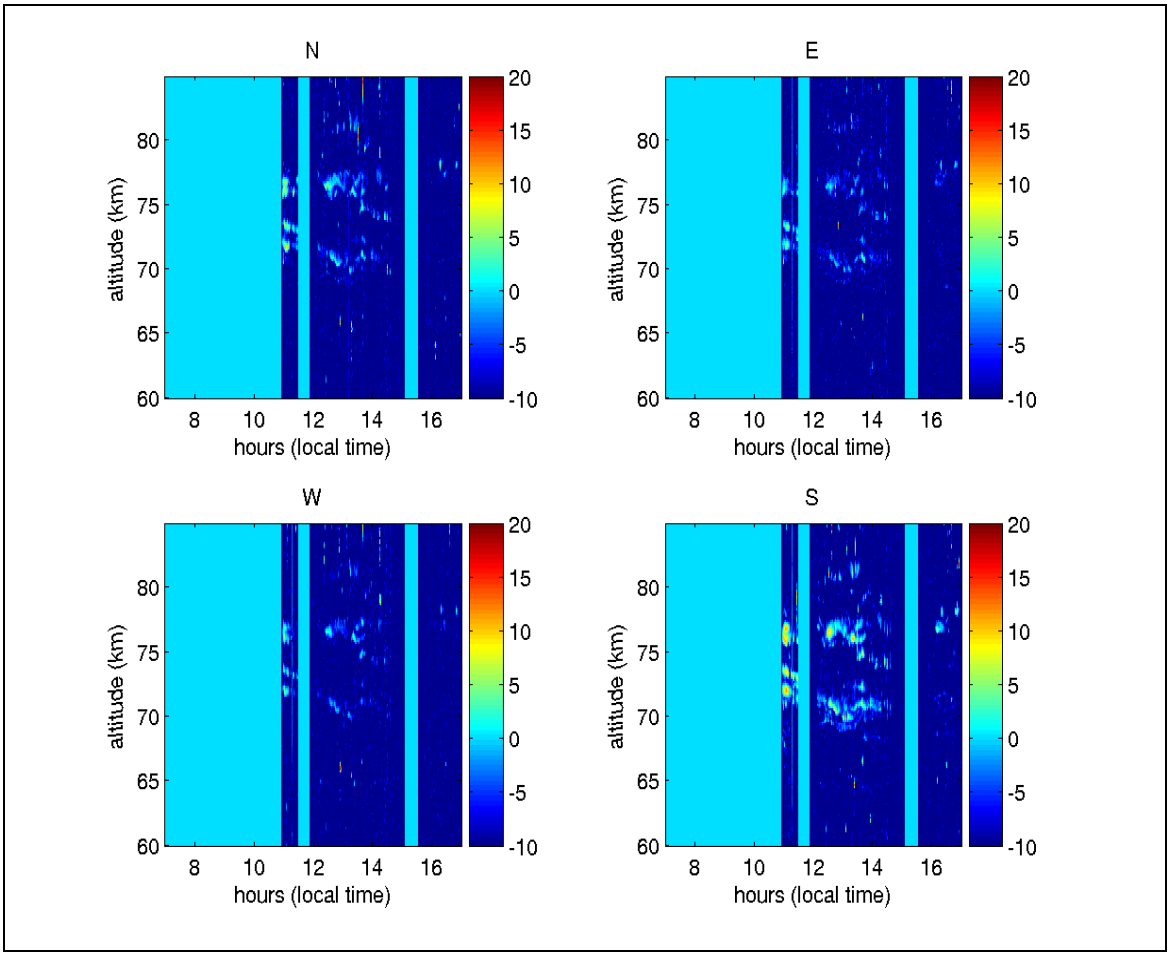

Figure A.3 SNR maps from 5/22/03 for the north, east, west and south beam

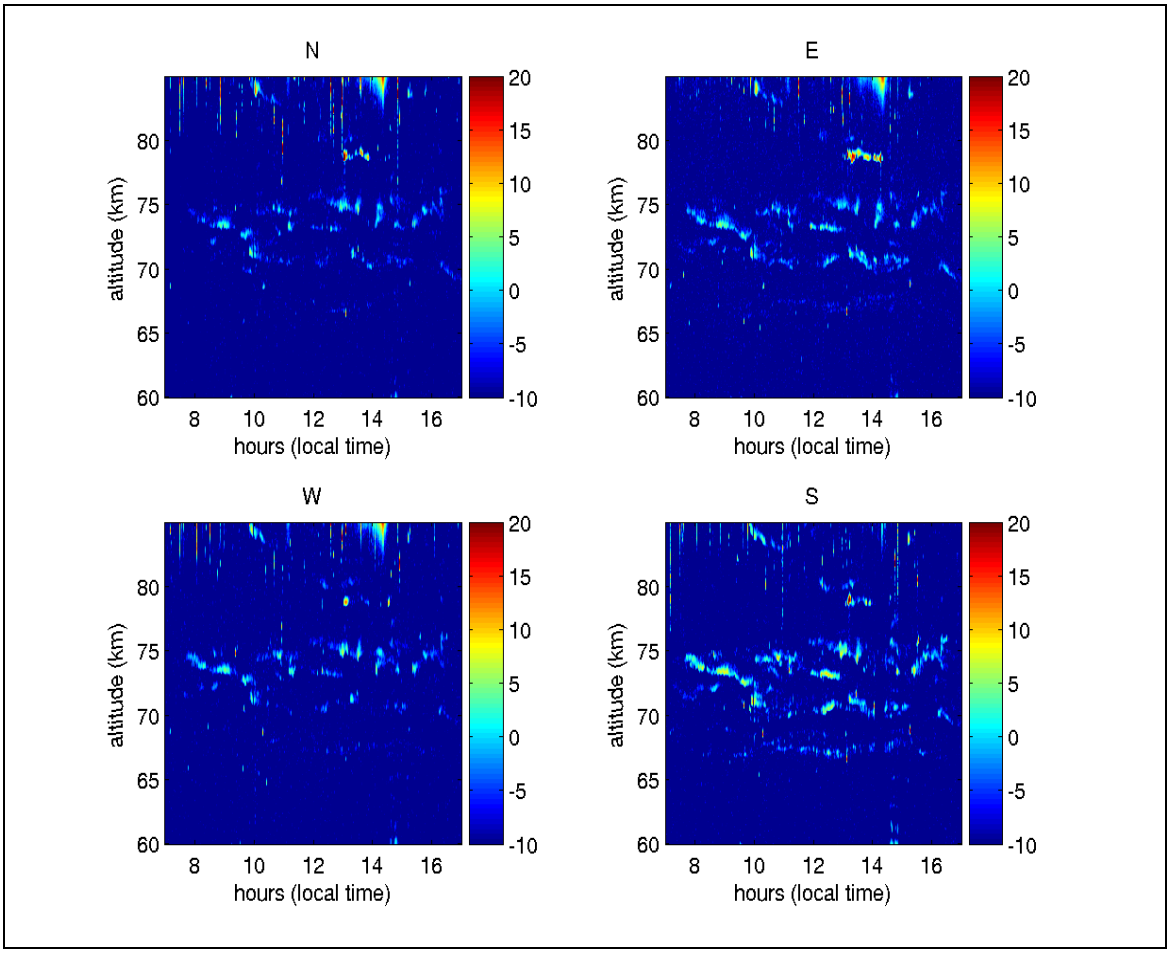

Figure A.4 SNR maps from 5/29/03 for the north, east, west and south beam

APPENDIX B

WIND FIELD AND WIND SHEAR IMAGES

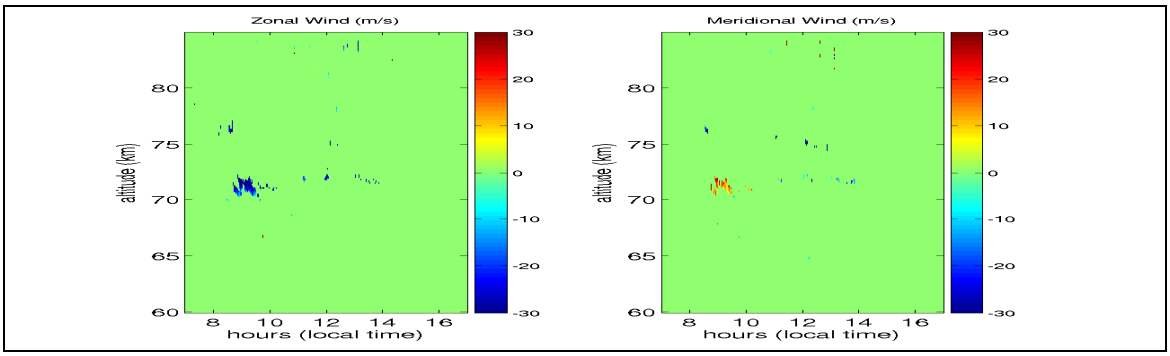

Figure B.1 Wind maps for 7/18/02

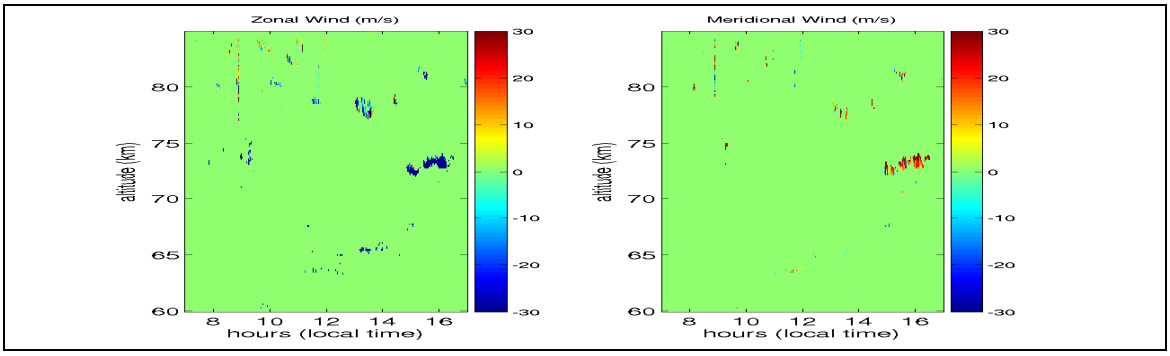

Figure B.2 Wind maps for 7/19/02

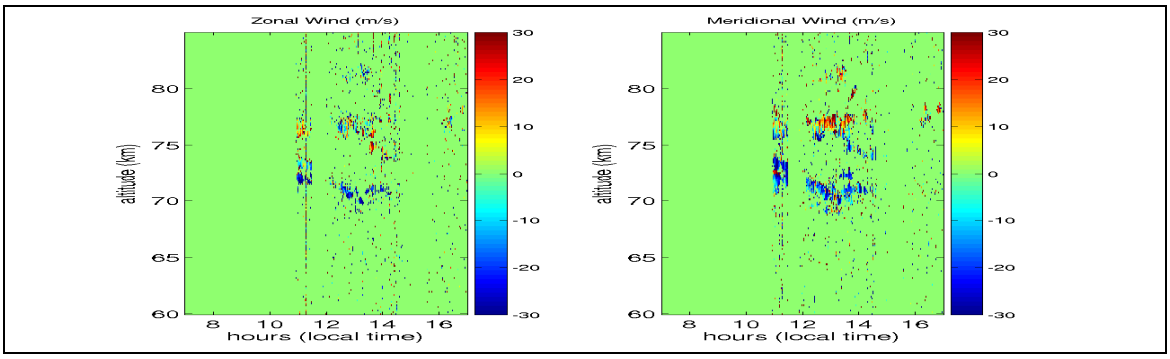

Figure B.3 Wind maps for 5/22/03

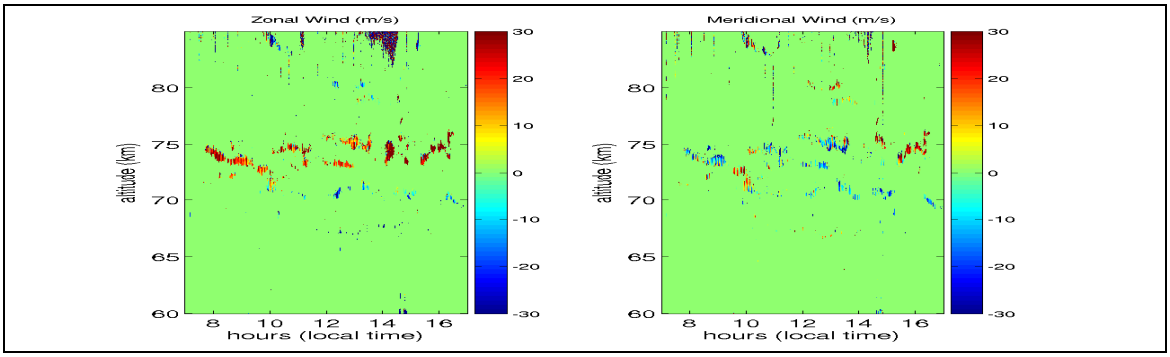

Figure B.4 Wind maps for 5/29/03

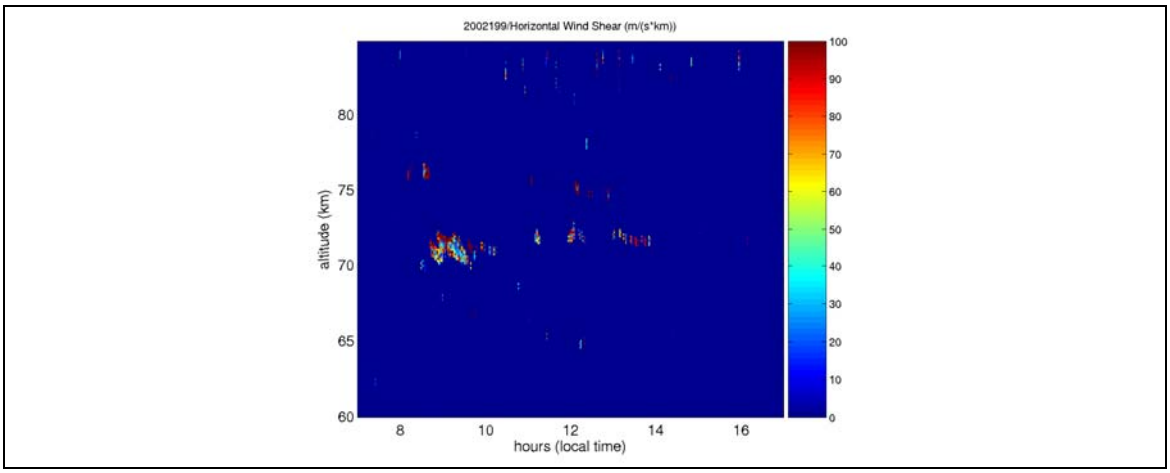

Figure B.5 wind shear map for 7/18/02

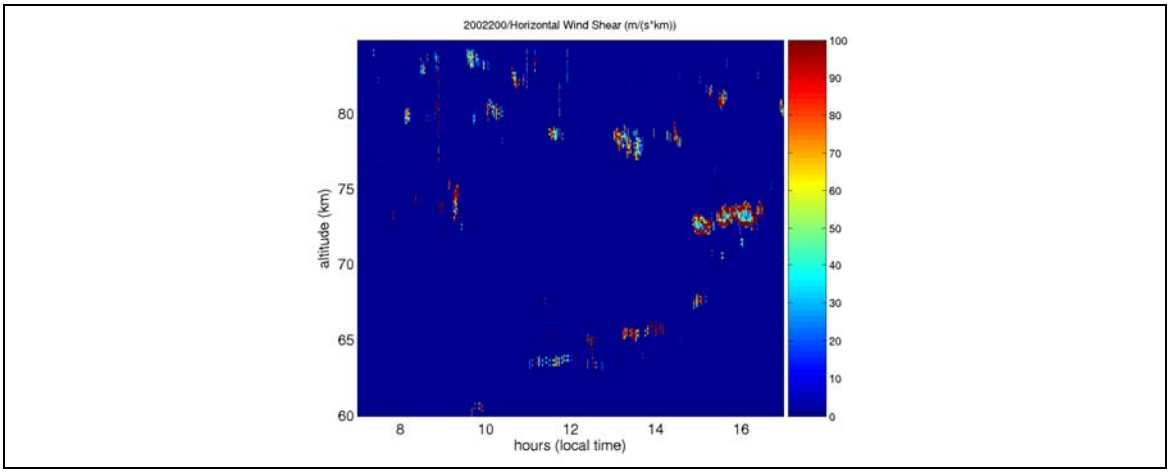

Figure B.6 wind shear map for 7/19/02

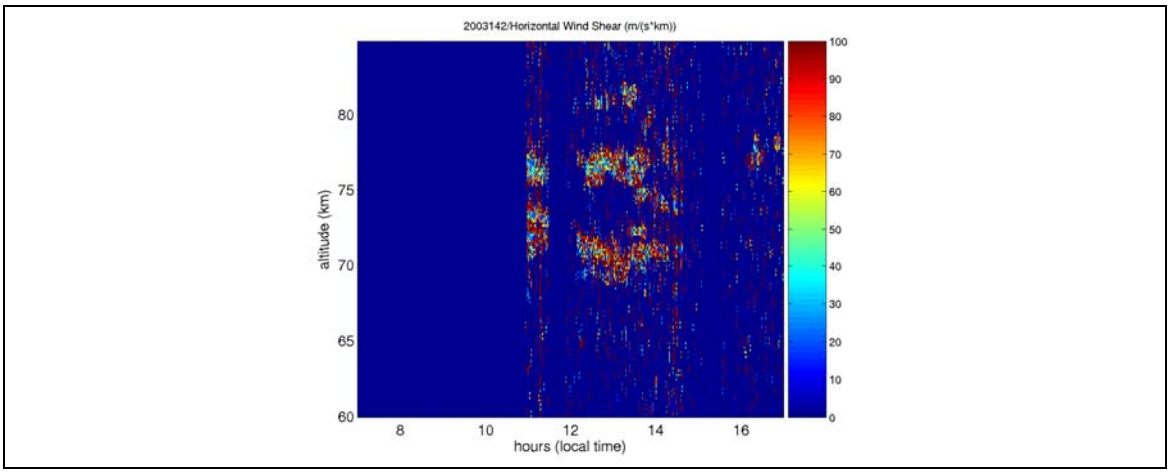

Figure B.7 wind shear map for 5/22/03

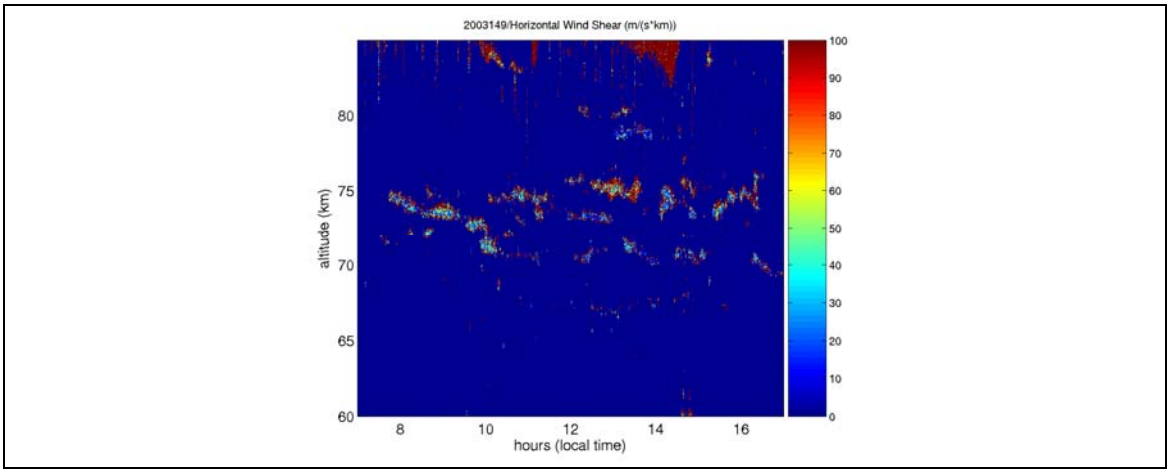

Figure B.8 wind shear map for 5/29/03

APPENDIX C SPECTRAL WIDTHS

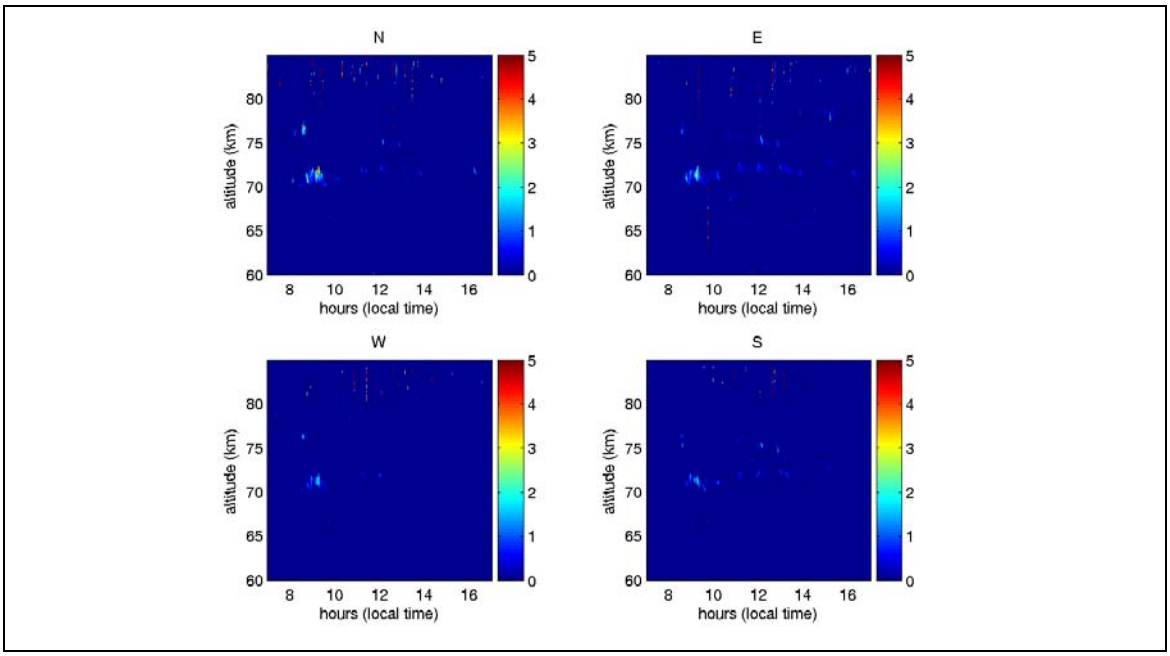

Figure C.1 σ_{turb}^2 maps for 7/18/02

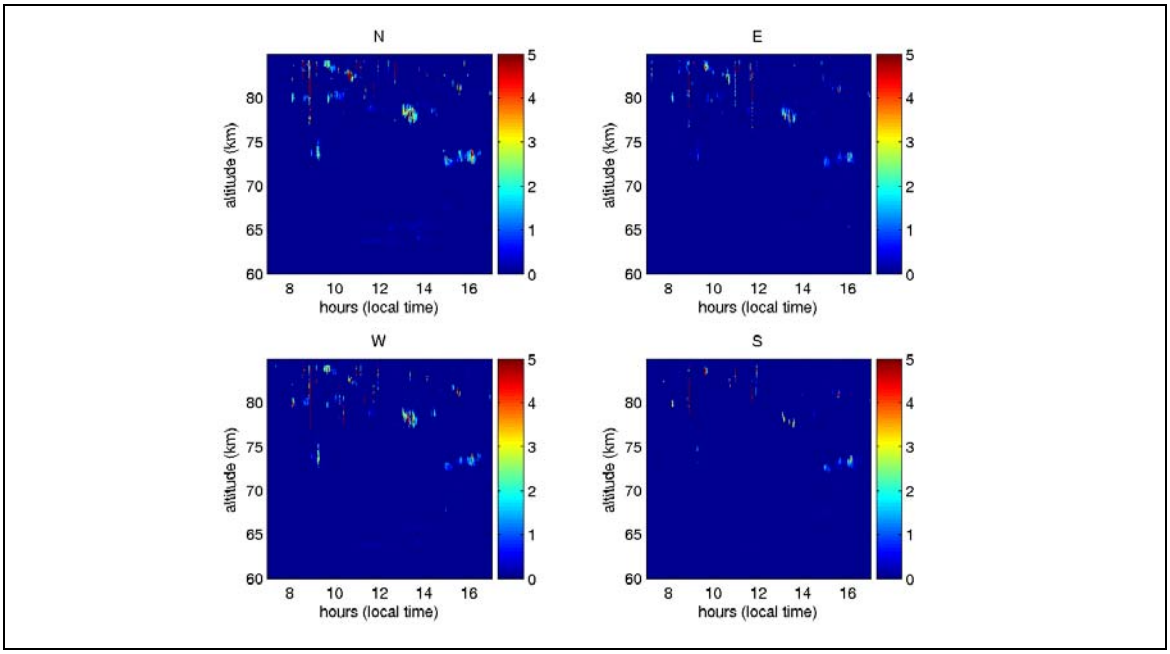

Figure C.2 σ_{turb}^2 maps for 7/19/02

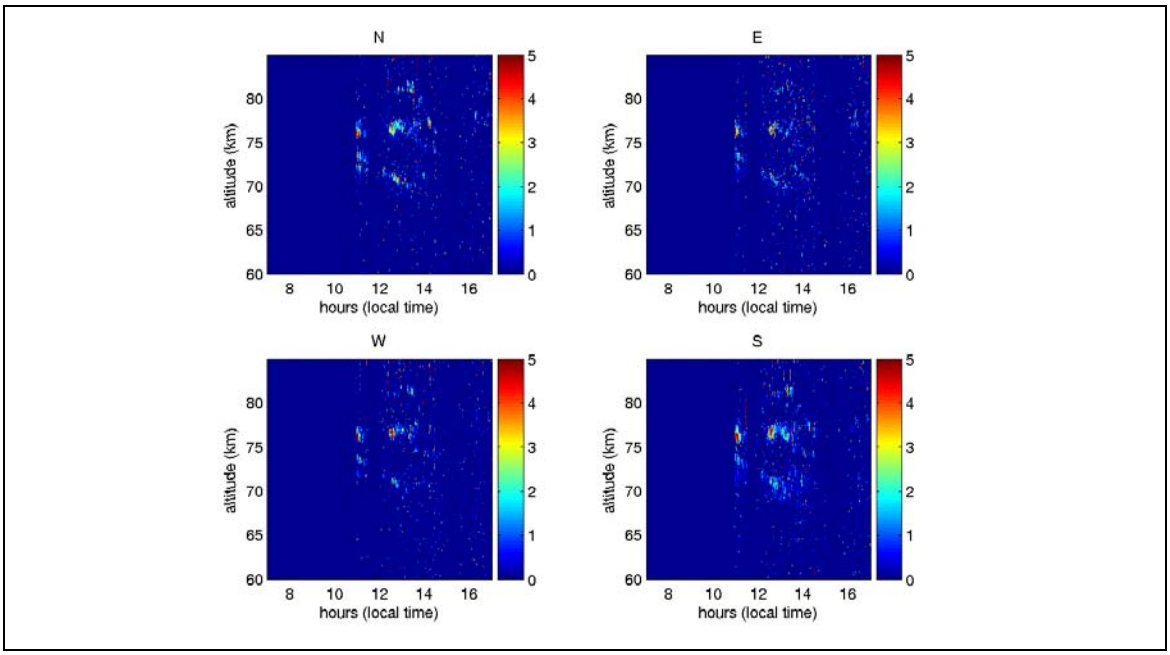

Figure C.3 σ_{turb}^2 maps for 5/22/03

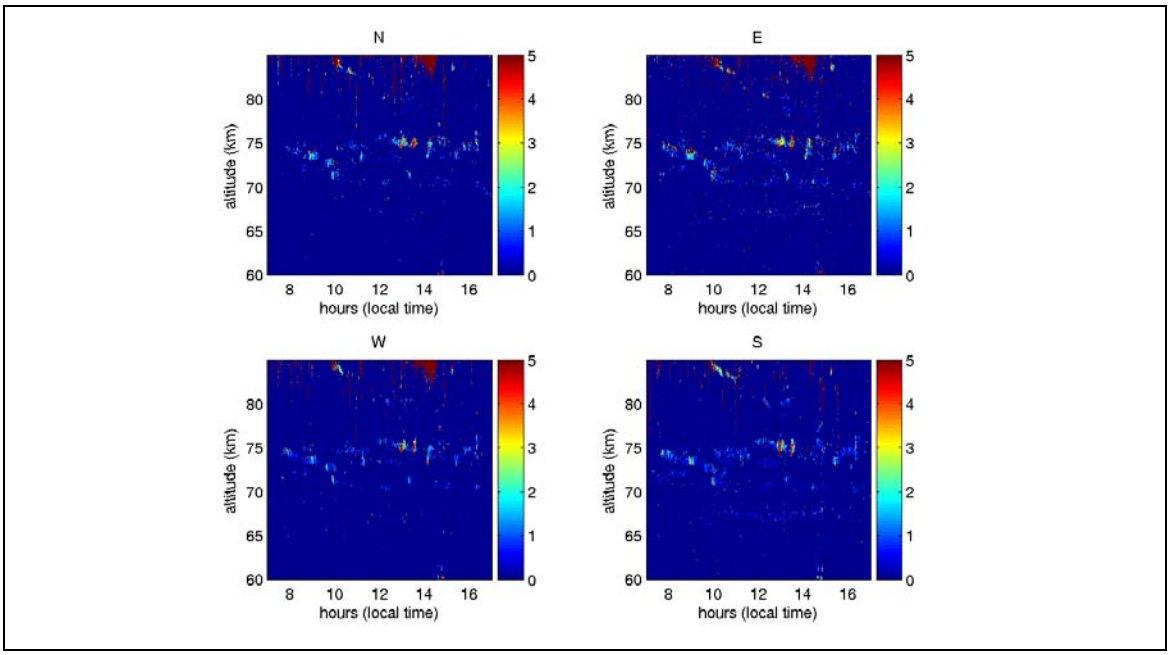

Figure C.4 σ_{turb}^2 maps for 5/29/03

APPENDIX D

ENERGY DISSIPATION RATE IMAGES

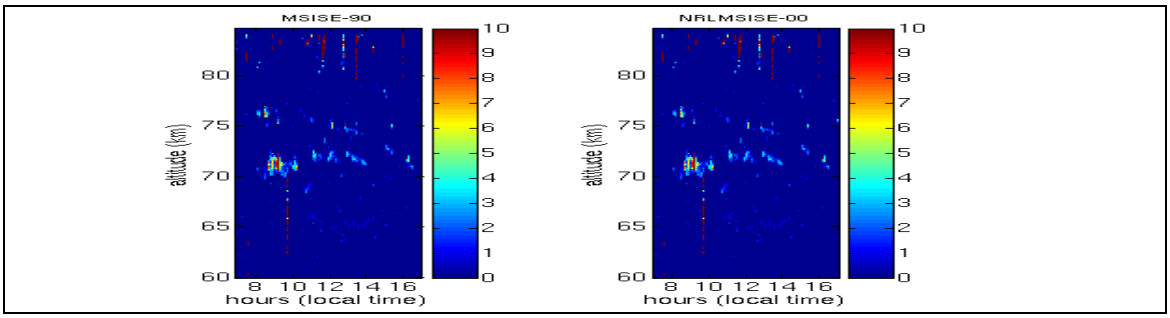

(a) ε (mW/kg) map for 7/18/02 (MSIS)

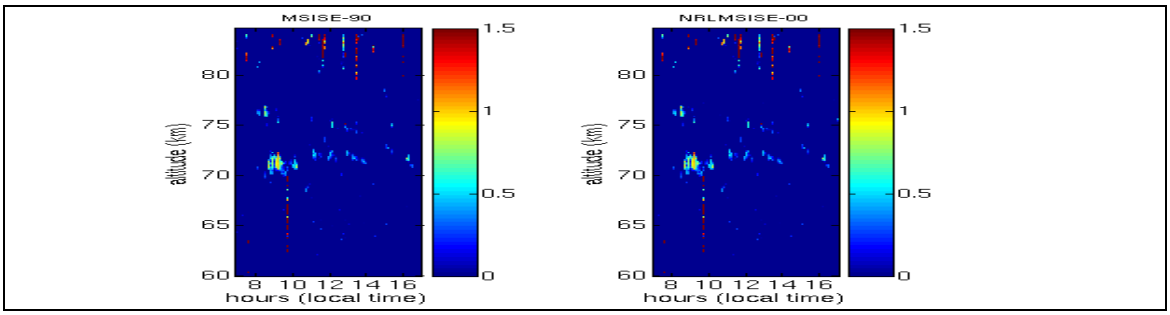

(b) Log K (m^2/s) map for 7/18/02 (MSIS)

Figure D.1 Turbulent parameter maps for 7/18/02 (MSIS)

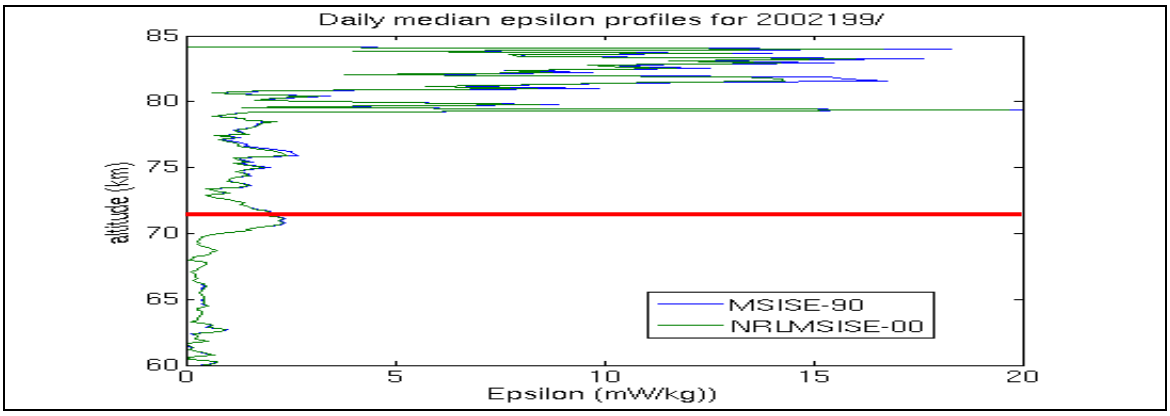

(a) ε (mW/kg) daily medians for 7/18/02 (MSIS)

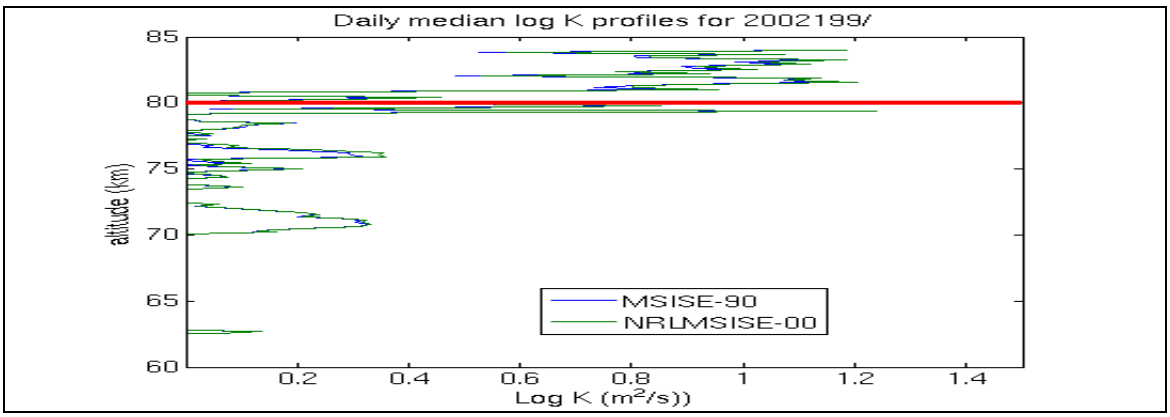

(b) Log K (m^2/s) daily medians for 7/18/02 (MSIS)

Figure D.2 Turbulent parameter daily medians for 7/18/02 (MSIS)

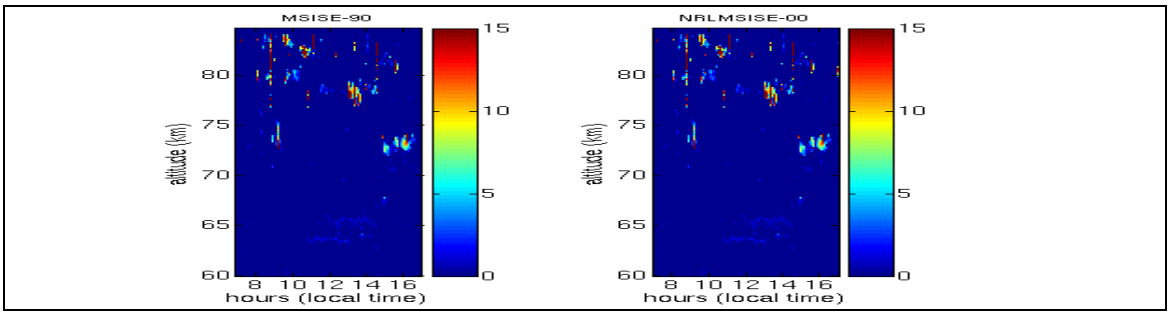

(a) ε (mW/kg) map for 7/19/02 (MSIS)

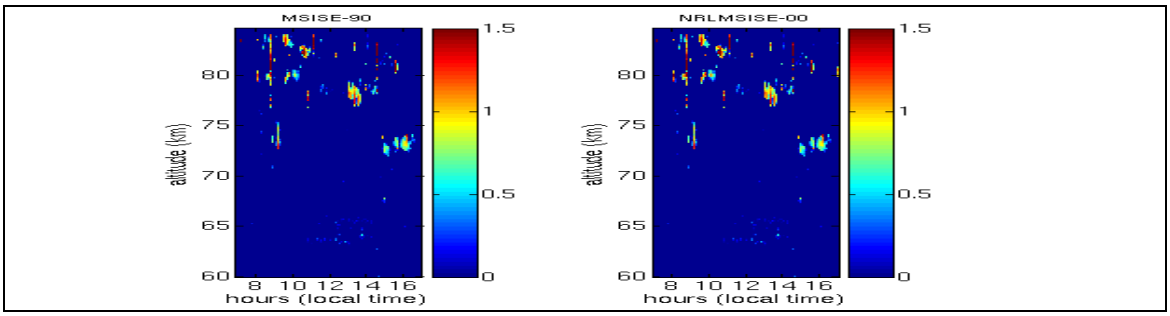

(b) Log K (m^2/s) map for 7/19/02 (MSIS)

Figure D.3 Turbulent parameter maps for 7/19/02 (MSIS)

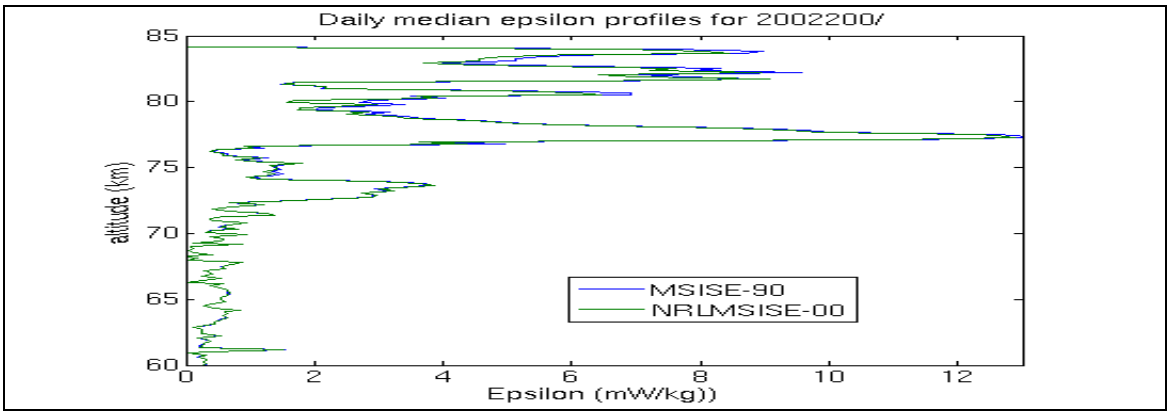

(a) ε (mW/kg) daily medians for 7/19/02 (MSIS)

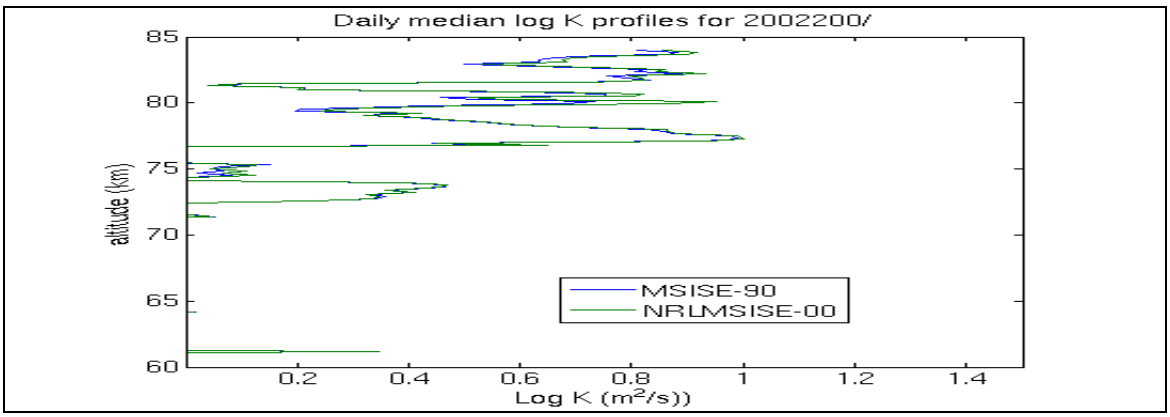

(b) Log K (m^2/s) daily medians for 7/19/02 (MSIS)

Figure D.4 Turbulent parameter daily medians for 7/19/02 (MSIS)

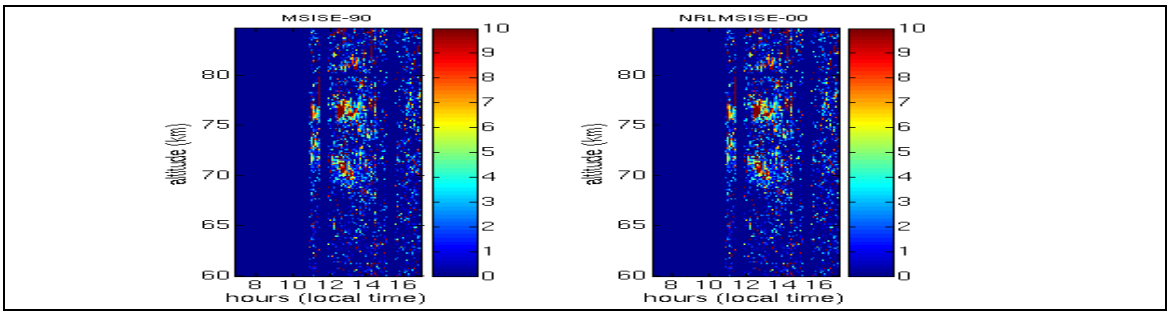

(a) ε (mW/kg) map for 5/22/03 (MSIS)

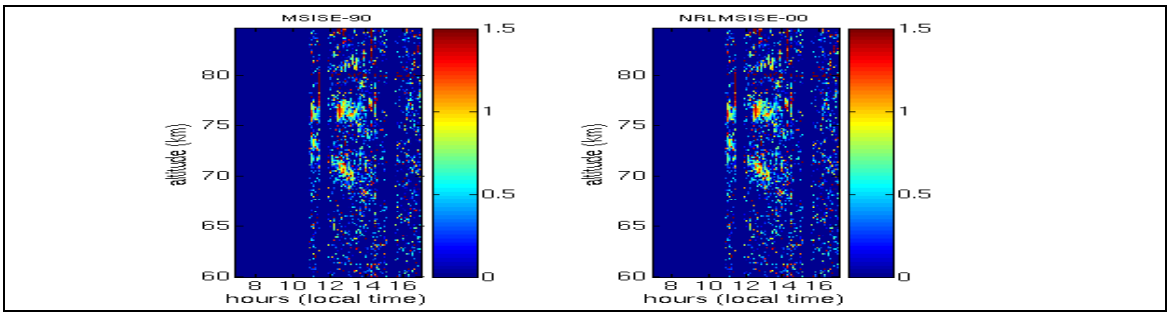

(b) Log K (m^2/s) map for 5/22/03 (MSIS)

Figure D.5 Turbulent parameter maps for 5/22/03 (MSIS)

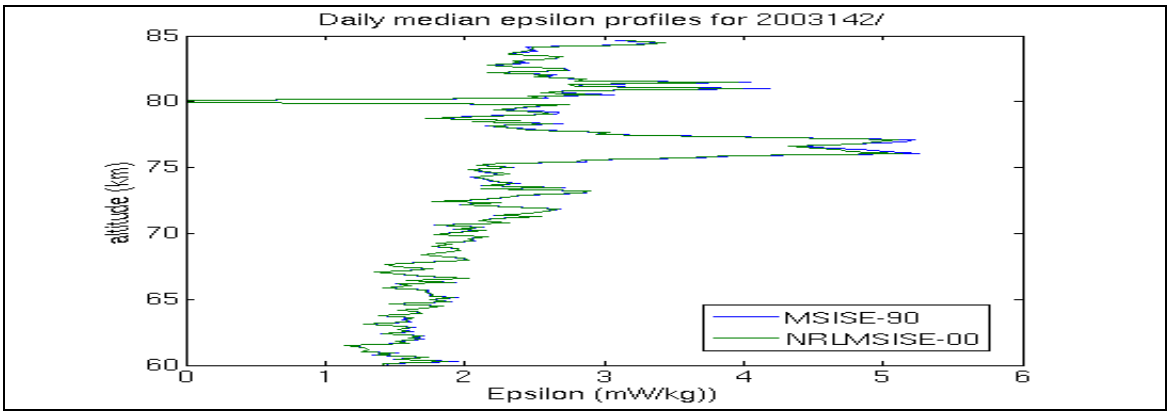

(a) ε (mW/kg) daily medians for 5/22/03 (MSIS)

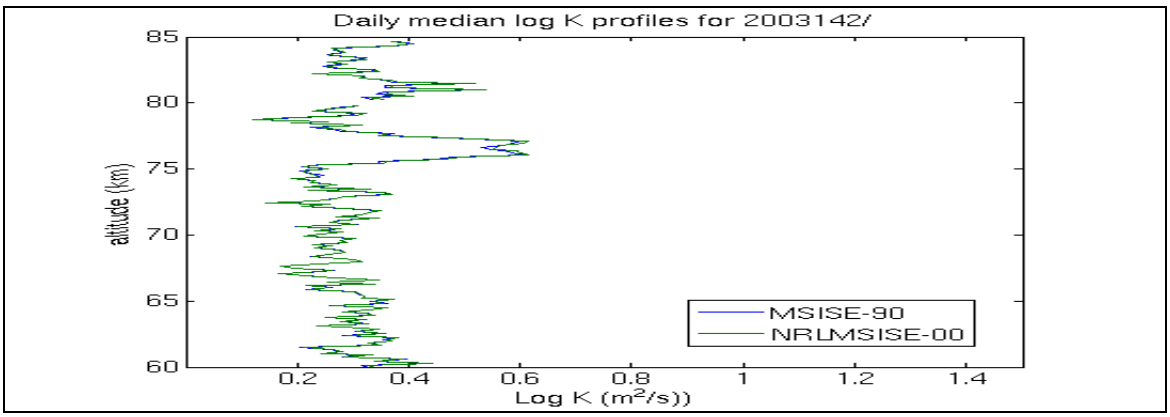

(b) Log K (m^2/s) daily medians for 5/22/03 (MSIS)

Figure D.6 Turbulent parameter daily medians for 5/22/03 (MSIS)

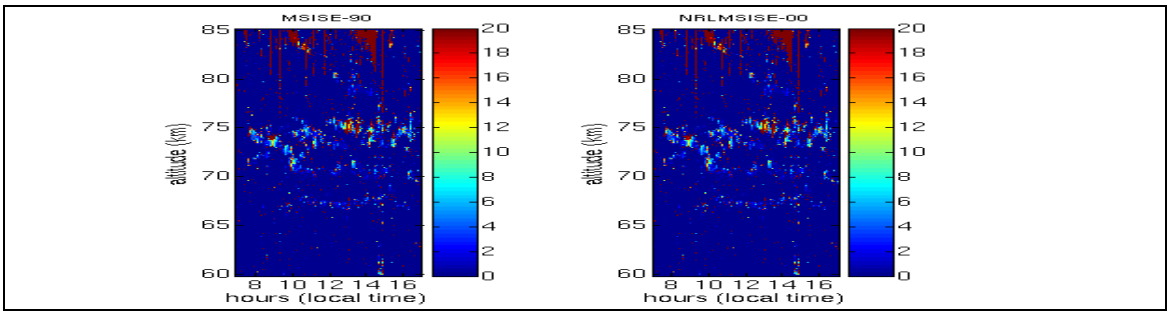

(a) ε (mW/kg) map for 5/29/03 (MSIS)

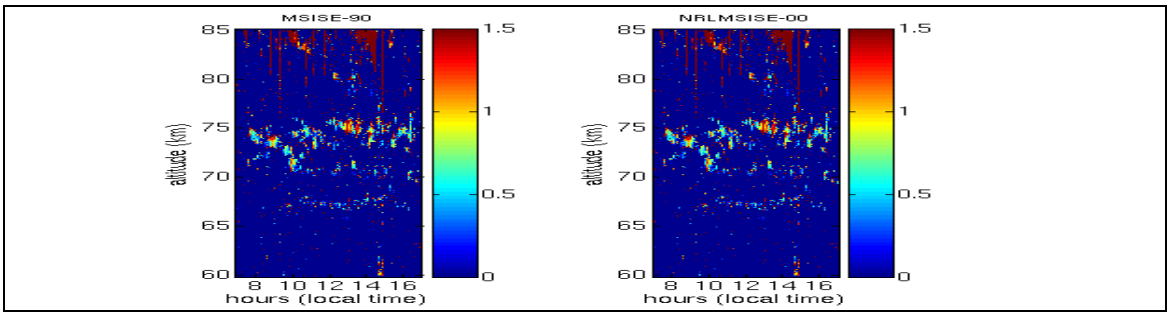

(b) Log K (m^2/s) map for 5/29/03 (MSIS)

Figure D.7 Turbulent parameter maps for 5/29/03 (MSIS)

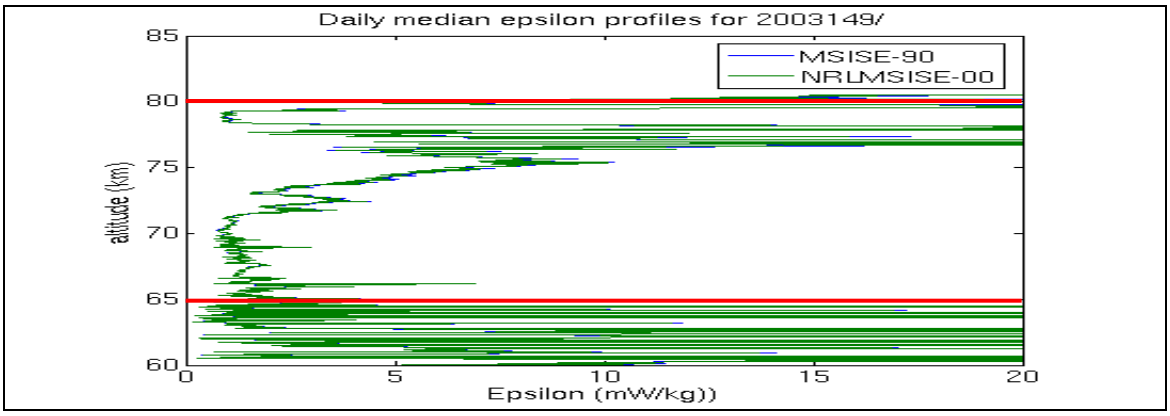

(a) ε (mW/kg) daily medians for 5/29/03 (MSIS)

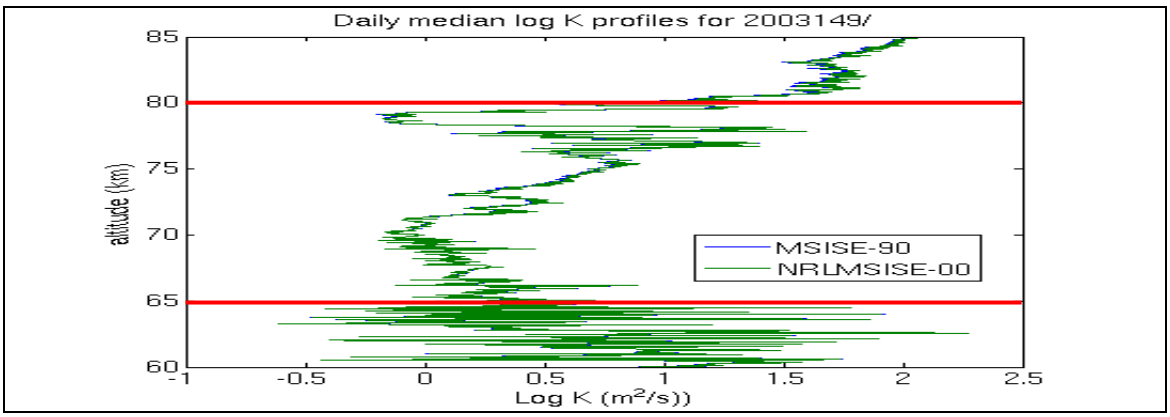

(b) Log K (m^2/s) daily medians for 5/29/03 (MSIS)

Figure D.8 Turbulent parameter daily medians for 5/29/03 (MSIS)

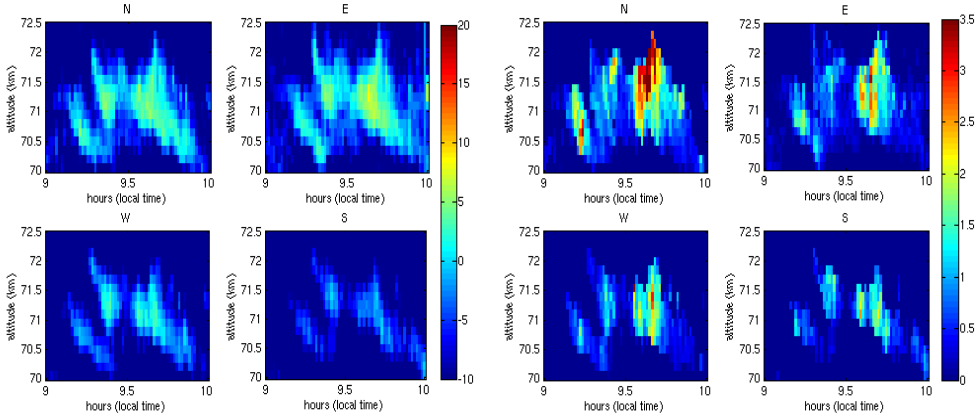

(a) SNR (b) σ_{turb}^2

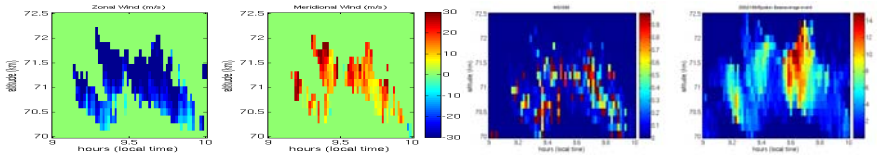

(c) Wind (d) Ri (e) ε

Figure D.9 7/18/02, 9-10 LT, 70-72.5 km

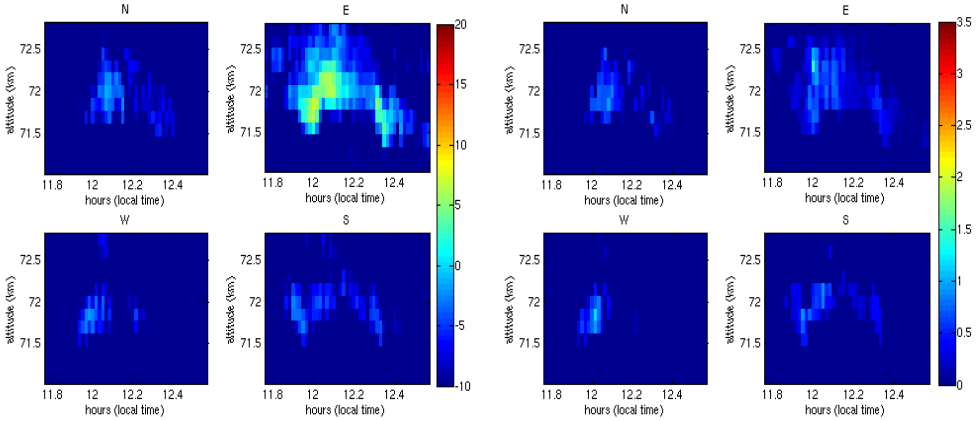

(a) SNR (b) σ_{turb}^2

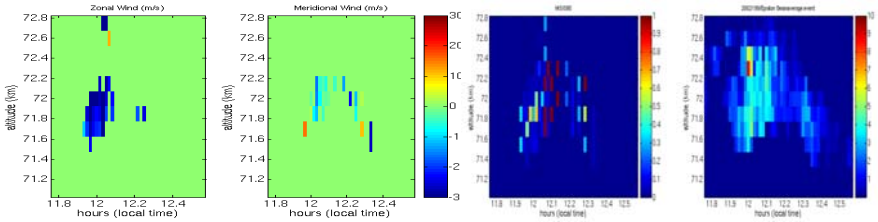

(c) Wind (d) Ri (e) ε

Figure D.10 7/18/02, 11:45-12:34 LT, 71-72.8 km

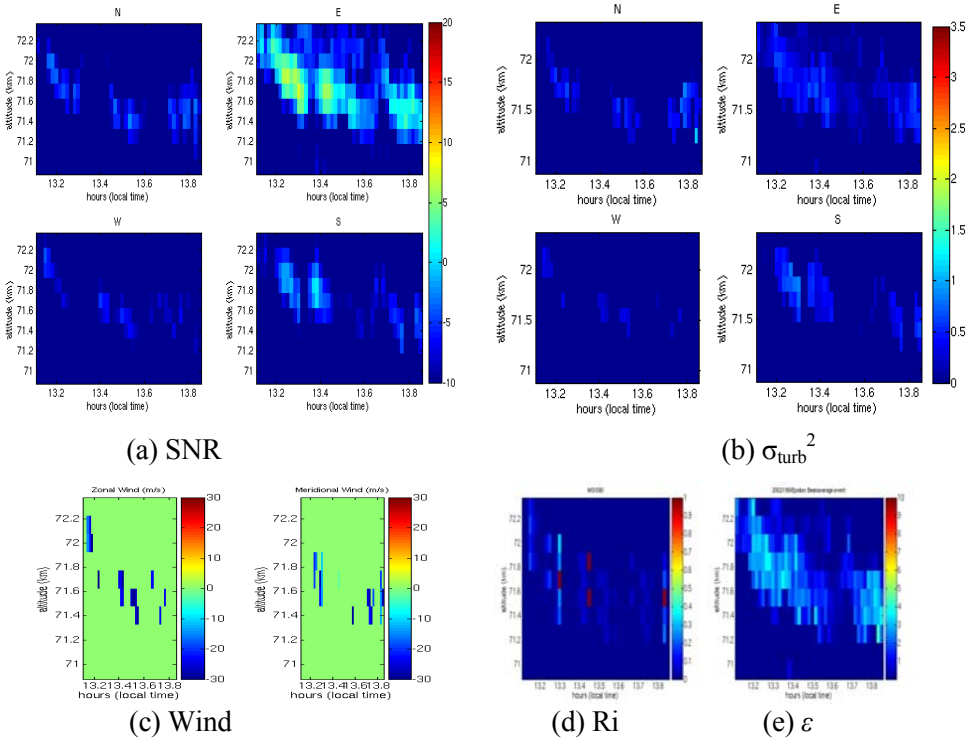

Figure D.11 7/18/02, 13:07-13:50 LT, 70.8-72.4 km

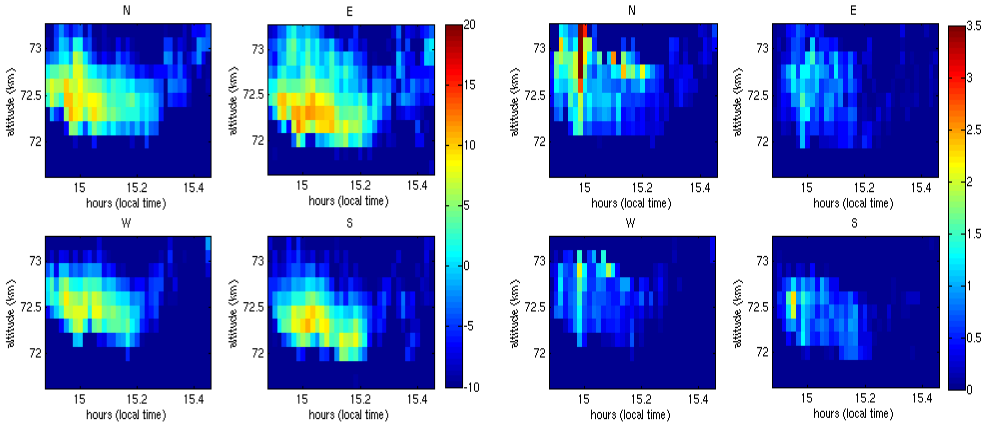

(a) SNR (b) σ_{turb}^2

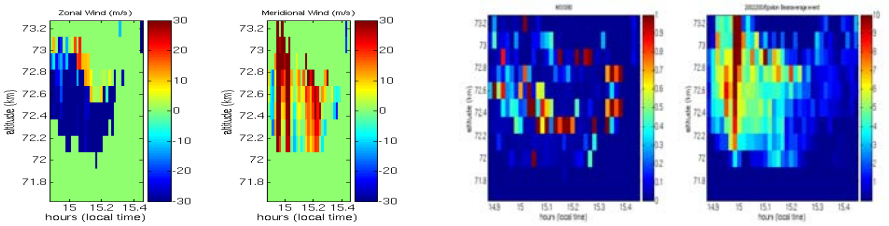

(c) Wind (d) Ri (e) ε

Figure D.12 7/19/02, 14:53-15:27 LT, 71.6-73.3 km

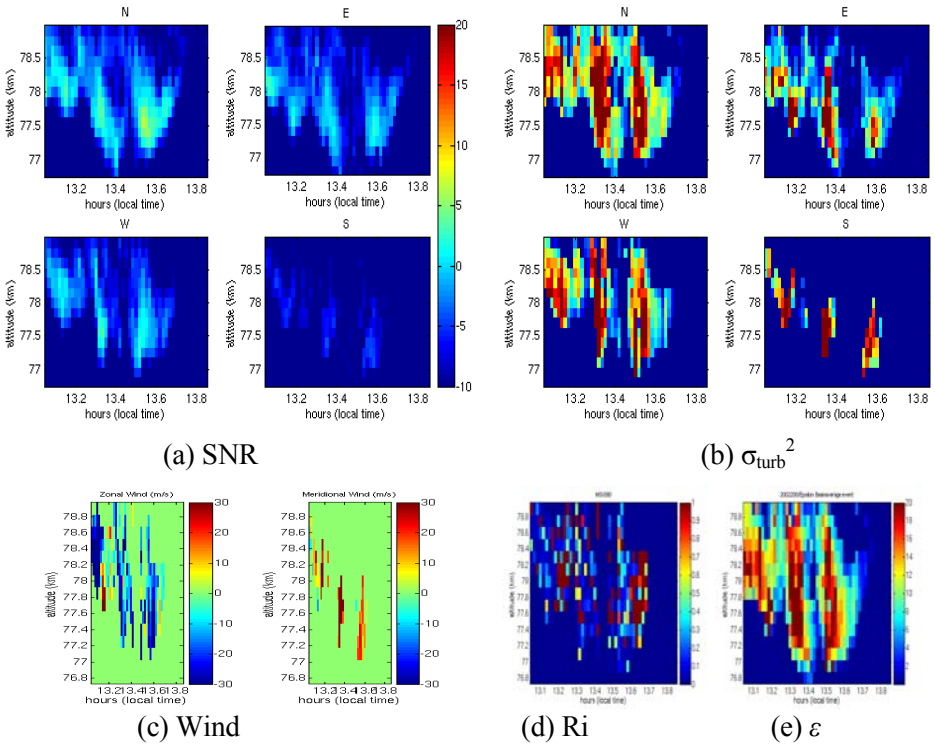

Figure D.13 7/19/02, 13:02-13:50 LT, 76.83- 78.91 km

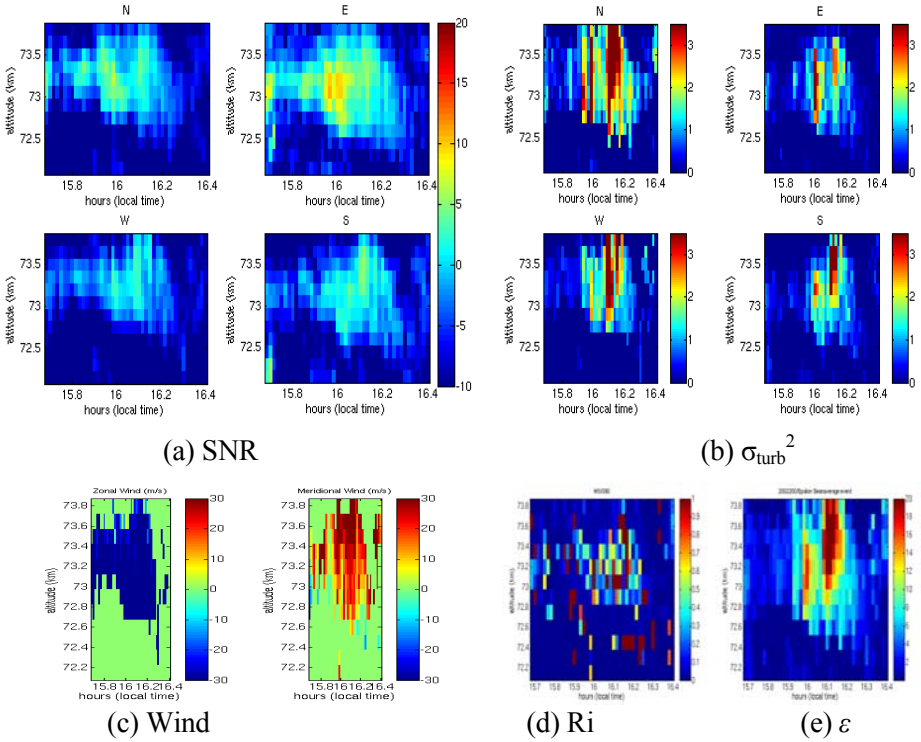

Figure D.14 7/19/02, 15:41-16:25 LT, 72.11-73.81 km

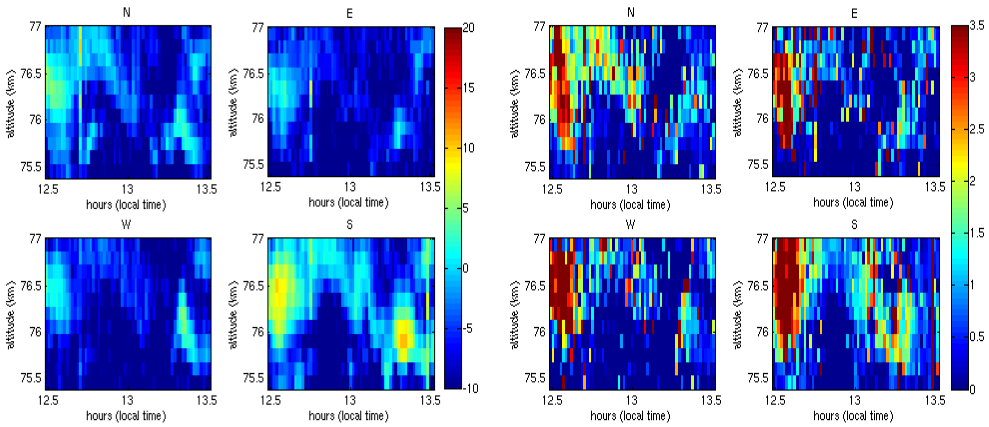

(a) SNR (b) σ_{turb}^2

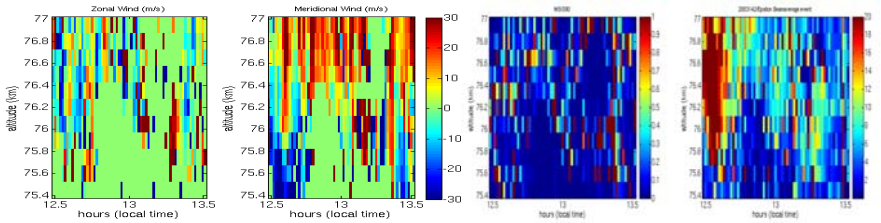

(c) Wind (d) Ri (e) ε

Figure D.15 5/22/03, 12:29-13:31 LT, 75.51-77.02 km

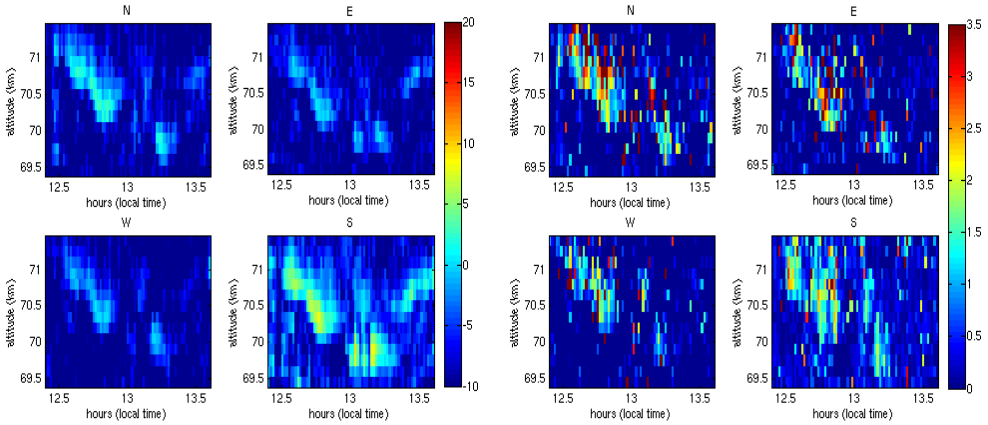

(a) SNR (b) σ_{turb}^2

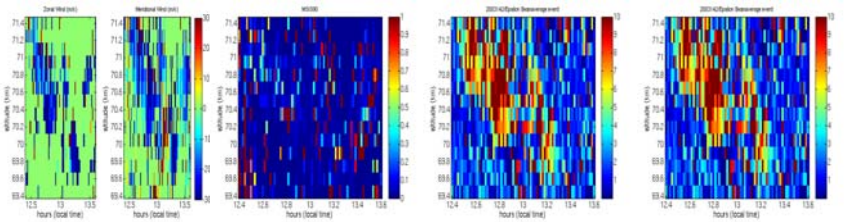

(c) Wind (d) Ri (e) ε

Figure D.16 5/22/03, 12:24-13:36 LT, 69.47-71.36 km

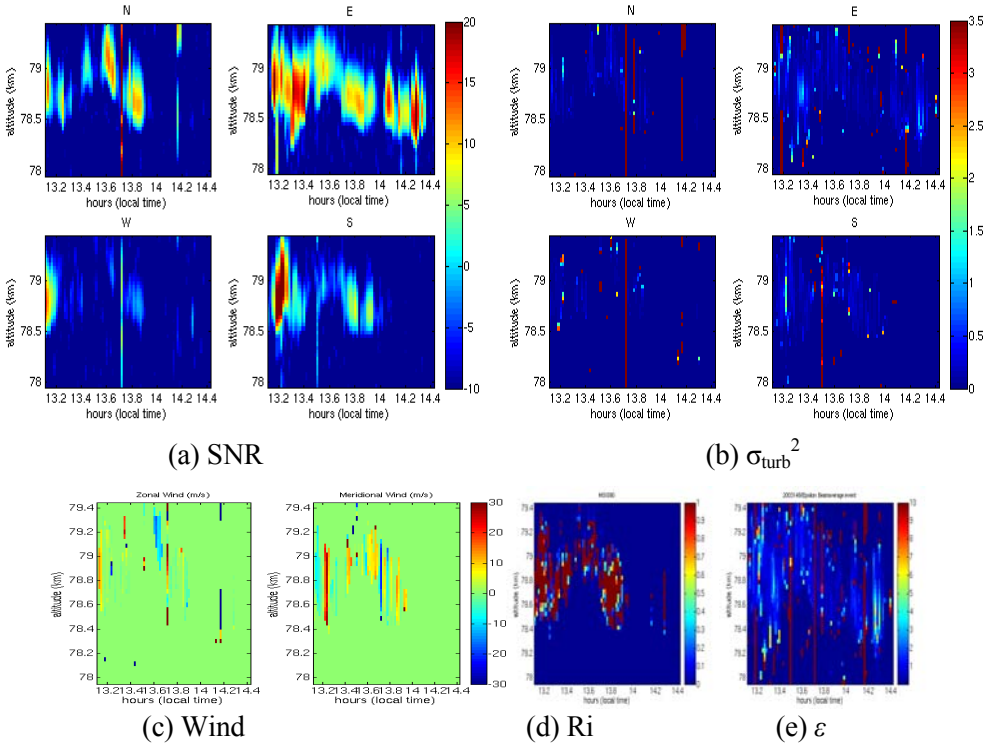

Figure D.17 5/29/03, 13:07-14:25 LT, 77.95-79.43 km

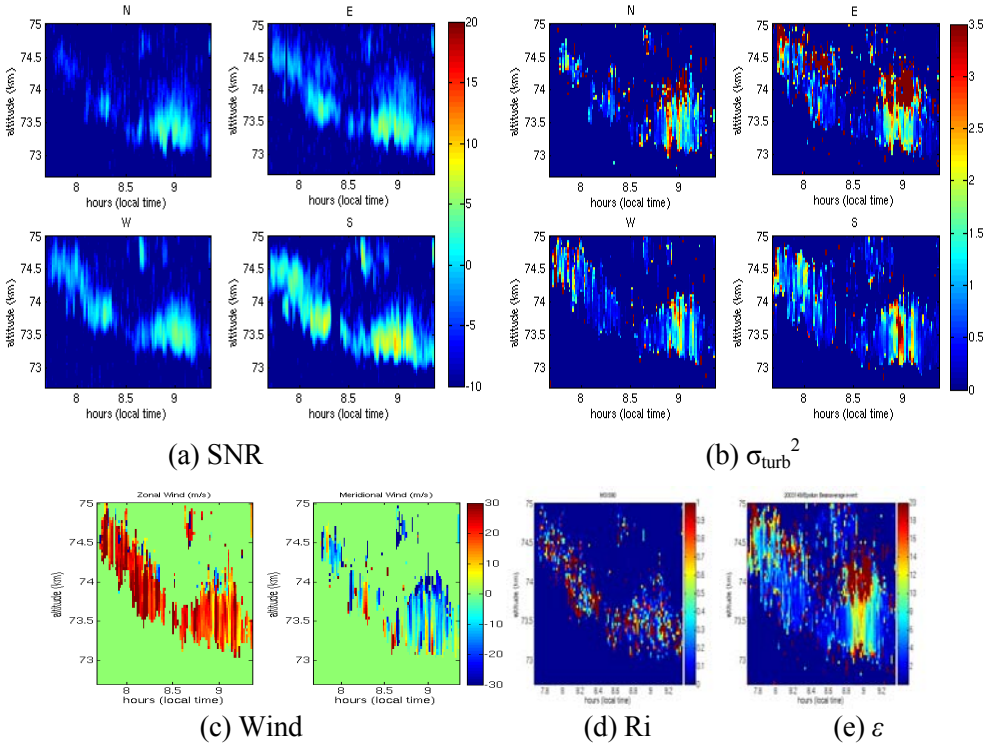

Figure D.18 5/29/03, 7:41-9:21 LT, 72.72-75 km

REFERENCES

Batchelor, G. K., The theory of homogeneous turbulence, Cambridge University Press, New York, 1953.

Bowles, K. L. Observation of vertical-incidence scatter from the ionosphere at 41Mc/sec, Phys. Rev. Lett., 1, 454-455, 1958.

Flock, W. L. and B. B. Balsley, VHF radar returns from the D region of the equatorial ionosphere, J. Geophys. Res., 72, 5537-5541, 1967.

Fritts, D. C., L. Yuan, M. H. Hitchman, L. Coy, E. Kudeki, R. F. Woodman, Dynamics of the equatorial mesosphere observed using the Jicamarca MST radar during June and August 1987, J. Atmos. Sci., 49, 2353-2371, 1992.

Fritts, D. C., J. F. Garten, D. M. Riggin, R. A. Goldberg, G. A. Lehmacher, F. J. Schmidlin, S. Mccarthy, E. Kudeki, C. D. Fawcett, M. H. Hitchman, R. S. Lieberman, I. M. Raid, R. A. Vincent, Equatorial dynamics observed by rocket, radar and satellite during CADRE/MARLTED campaign 2: Mean and wave structure, coherence, and variability, J. Geophys. Res., 102, 26,191-26,216, 1997.

Fukao, S., M. D. Yamanaka, Naoki Ao, W. K. Hocking, T. Sato, M. Yamamoto, T. Nakamura, T. Tsuda, and S. Kato, Seasonal variability of vertical eddy diffusivity in the middle atmosphere 1. Three-year observations by the middle and upper atmosphere radar, J. Geophys. Res., 99, 18973-18987, 1994.

Garcia, R. R., S. Solomon, The effect of breaking gravity waves on the dynamics and chemical composition of the mesosphere and lower thermosphere, J. Geophys. Res., 20, 3850-3868, 1985.

Hedin, A.E., MSIS-86 Thermospheric Model, J. Geophys. Res., 92, 4649, 1987.

Hedin, A. E., Extension of the MSIS thermosphere model into the middle and lower atmosphere, J. Geophys. Res., 96, 1159-1172, 1991.

Hocking, W. K., On the extraction of atmospheric turbulence parameters from radar backscatter Doppler spectra-1. Theory, J. Atmos. Terr. Phys., 45, 89, 1983.

Hocking, W. K., Measurements of turbulent energy dissipation rate in the middle atmosphere by radar technique: A review, Radio Sci., 20, 1403, 1985.

Hocking, W. K., Observations and measurements of turbulence in the middle atmosphere with a VHF radar, J. Atmos. Terr. Phys., 48, 655, 1986.

Hocking, W. K., Recent advances in radar instruments and techniques for studies of the mesosphere, stratosphere and troposphere, Radio Sci., 32, 2241, 1997.

Kudeki, E., Radar interferometer observations of mesospheric echoing layers at Jicamarca, J. Geophys. Res., 93, 5413-5421, 1988.

Kudeki, E., S. Bhattacharyya, and R. F. Woodman, A new approach in incoherent scatter F region E×B drift measurements at Jicamarca, J. Geophys. Res., 104, 28,145-28,162, 1999.

Lehmacher, G. A., E. Kudeki, Variability of mesospheric echoes, Adv. Space Res. 32(5), 747-752, 2003.

Lübken, F. -J., V. Von Zahn, E. V. Thrane, T. A. Blix, G. A. Kokin, S. V. Pachomov, In-situ measurements of turbulence energy dissipation rates and eddy diffusion coefficients during MAP/WINE, J. Atmos. Terr. Phys., 49, 763, 1987.

Lübken, F. -J., G. A. Lehmacher, T. Blix, U. -P. Hoppe, E. Thrane, First in-situ observations of neutral and plasma density fluctuations within a PMSE layer, Geophys. Res. Lett., 20, 2311-2314, 1993 (a).

Lübken, F. -J., Experimental results on the role of turbulence for the heat budget of the upper atmosphere, Habilitation thesis, Bonn University, 1993 (b).

Lübken, F. -J., Seasonal variation of turbulent energy dissipation rates at high latitudes as determined by in situ measurements of neutral density fluctuations, J. Geophys. Res., 102, 13,441-13,456, 1997.

Picone, J. M., A.E. Hedin, D.P. Drob, and A.C. Aikin, NRLMSISE-00 Empirical Model of the Atmosphere: Statistical Comparisons and Scientific Issues, J. Geophys. Res., 107, A12, 1468, doi:10.1029/2002JA009430, 2002.

Rastogi, P. K. and R. F. Woodman, Mesospheric studies using the Jicamarca Incoherent-scatter radar, J. Atmos. Terr. Phys., 36, 1217-1231, 1974.

Rao, D. N., M. V. Ratnam, T. N. Rao, S. V. B. Rao, Seasonal variation of vertical eddy diffusivity in the troposphere, lower stratosphere and mesosphere over a tropical station, Ann. Geophysicae, 19,975-19,984, 2001.

Remsberg, E.; Lingenfelser, G.; Harvey, V. L.; Grose, W.; Russell, J., III; Mlynczak, M.; Gordley, L.; Marshall, B. T., On the verification of the quality of SABER temperature, geopotential height, and wind fields by comparison with Met Office assimilated analyses, J. Geophys. Res., 108, D20, 4628, doi: 10.1029/2003JD003720, 2003.

Riggin, D. M., E. Kudeki, Z. Feng, M. Sarango, R. S. Lieberman, Jicamarca radar observations of the diurnal and semidiurnal tide in the troposphere and lower stratosphere, J. Geophys. Res., 107, D8, 4062, 10.1029/2001JD001216, 2002.

Röttger, J. The MST radar technique, Handbook for Middle Atmosphere Program, 13, 187-232, 1984.

Royrvik, O., VHR radar signals scattered from the equatorial mesosphere, Radio Sci., 18, 1325-1335, 1983.

Royrvik, O. and L. G. Smith, Comparison of mesospheric VHF radar echoes and rocket probe electron concentration measurements, J. Geophys. Res., 89, A10, 9014-9022, 1984.

Russell III, J. M., M. G. Mlynczak, L. L. Gordley, An overview of the SABER experiment for the TIMED mission, SPIE, 2266, 407-415, 1994.

Sato, T. and R. F. Woodman, Fine altitude resolution observations of stratospheric turbulent layers by the Arecibo 430-M. Hz radar, J. Atmos. Sci., 39, 2546, 1982.

Sheth, R., E. Kudeki, G. Lehmacher, M. Sarango, R. Woodman, L. Guo, P. Reyes, A high-resolution study of mesospheric density structures with he Jicamarca MST radar, Ann. Geophysicae, submitted, 2005.

Stitt, G. R., E. Kudeki, Interferometric cross-spectral studies of mesospheric scattering layers, Radio Sci., 26, 783-799, 1991.

Tatarski, V. I., Wave propagation in a turbulent medium, McGraw-Hill, New York, 1961.

Van Zandt, T. E., J. L. Green, K. S. Gage, W. L. Clark, Vertical profiles of refractivity turbulence structure constant: Comparison of observations by the Sunset radar with a new theoretical model, Radio Sci., 13, 819-829, 1978.

Weinstock, J., Energy dissipation rates of turbulence in the stable free atmosphere, J. Atmos. Sci., 38, 4, 880, 1981.

Woodman, R. F., A. Guillen, Radar observation of winds and turbulence in the stratosphere and mesosphere, J. Atmos. Sci., 31, 493, 1974.

Woods, J. D., On Richardson's number as a criterion for laminar-turbulent-laminar trasition in the ocean and atmosphere, Radio Sci., 14, 1289-1298, 1969.